

INFORMATION TO USERS

This was produced from a copy of a document sent to us for microfilming. While the most advanced technological means to photograph and reproduce this document have been used, the quality is heavily dependent upon the quality of the material submitted.

The following explanation of techniques is provided to help you understand markings or notations which may appear on this reproduction.

1. The sign or "target" for pages apparently lacking from the document photographed is "Missing Page(s)". If it was possible to obtain the missing page(s) or section, they are spliced into the film along with adjacent pages. This may have necessitated cutting through an image and duplicating adjacent pages to assure you of complete continuity.
2. When an image on the film is obliterated with a round black mark it is an indication that the film inspector noticed either blurred copy because of movement during exposure, or duplicate copy. Unless we meant to delete copyrighted materials that should not have been filmed, you will find a good image of the page in the adjacent frame. If copyrighted materials were deleted you will find a target note listing the pages in the adjacent frame.
3. When a map, drawing or chart, etc., is part of the material being photographed the photographer has followed a definite method in "sectioning" the material. It is customary to begin filming at the upper left hand corner of a large sheet and to continue from left to right in equal sections with small overlaps. If necessary, sectioning is continued again—beginning below the first row and continuing on until complete.
4. For any illustrations that cannot be reproduced satisfactorily by xerography, photographic prints can be purchased at additional cost and tipped into your xerographic copy. Requests can be made to our Dissertations Customer Services Department.
5. Some pages in any document may have indistinct print. In all cases we have filmed the best available copy.

University
Microfilms
International

300 N. ZEEB RD., ANN ARBOR, MI 48106

8209128

Hendrickson, Joel Stephen

**PHI PRODUCTION AND THE OZI RULE IN POSITIVE PION(D)
INTERACTIONS AT 10 GEV/C**

Iowa State University

PH.D. 1981

**University
Microfilms
International**

300 N. Zeeb Road, Ann Arbor, MI 48106

PLEASE NOTE:

In all cases this material has been filmed in the best possible way from the available copy. Problems encountered with this document have been identified here with a check mark ✓.

1. Glossy photographs or pages _____
2. Colored illustrations, paper or print _____
3. Photographs with dark background _____
4. Illustrations are poor copy _____
5. Pages with black marks, not original copy _____
6. Print shows through as there is text on both sides of page _____
7. Indistinct, broken or small print on several pages ✓ _____
8. Print exceeds margin requirements _____
9. Tightly bound copy with print lost in spine _____
10. Computer printout pages with indistinct print _____
11. Page(s) _____ lacking when material received, and not available from school or author.
12. Page(s) _____ seem to be missing in numbering only as text follows.
13. Two pages numbered _____. Text follows.
14. Curling and wrinkled pages _____
15. Other _____

**University
Microfilms
International**

π^0 production and the OZI rule in π^+d interactions at 10 GeV/c

by

Joel Stephen Hendrickson

A Dissertation Submitted to the
Graduate Faculty in Partial Fulfillment of the
Requirements for the Degree of
DOCTOR OF PHILOSOPHY

Department: Physics
Major: High Energy Physics

Approved:

Signature was redacted for privacy.

In Charge of Major Work

Signature was redacted for privacy.

For the Major Department

Signature was redacted for privacy.

For the Graduate College

Iowa State University
Ames, Iowa

1981

TABLE OF CONTENTS

	Page
CHAPTER 1. INTRODUCTION	1
CHAPTER 2. THEORY	3
CHAPTER 3. EQUIPMENT	25
CHAPTER 4. TRIGGERING AND DATA ACQUISITION	46
CHAPTER 5. EVENT RECONSTRUCTION	55
CHAPTER 6. DATA ANALYSIS AND MONTE CARLO	69
CHAPTER 7. RESULTS	79
APPENDIX	111
BIBLIOGRAPHY	132

CHAPTER 1. INTRODUCTION

The recent discovery of numerous heavy particles with abnormally small hadronic decay widths has naturally motivated a search for a mechanism that suppresses these hadronic decay modes. The Okubo-Zweig-Iizuka (OZI) rule (1-4) predicts the suppression of these decay modes and is currently the accepted explanation. However, the OZI rule was originally only an ansatz and as yet its dynamical origin is not fully understood. If the OZI rule were exact, the suppression would be complete; however, the fact that these decay modes are observed indicates that the OZI rule is violated. The dynamical mechanism for the suppression cannot be understood until the degree of violation has been measured and it is to this end that the present experiment has measured the cross sections for the reactions $\pi^+ n \rightarrow \phi p$ and $\pi^+ p \rightarrow \phi \Delta^{++}$ both of which are forbidden by the OZI rule. A history of the OZI rule and a discussion of the status of current theoretical models of the dynamical origin of the OZI rule are presented in Chapter 2.

The experiment was conducted at the Stanford Linear Accelerator Center (SLAC) Large Aperture Solenoid Spectrometer (LASS) facility and involved approximately five million primary physics triggers. A description of the apparatus is presented in Chapter 3. The experiment was designed to study reactions with final states involving kaons; thus, the trigger selected events with at least one fast forward particle with a mass greater than the pion mass. The trigger logic and data acquisition

system are discussed in Chapter 4. Chapter 5 presents the method used for reconstructing the events and Chapter 6 describes the data analysis and the Monte Carlo. The results of the cross section measurements for the reactions $\pi^+ n \rightarrow \phi p$ and $\pi^+ p \rightarrow \phi \Delta^{++}$ are presented in Chapter 7 and the degree of violation of the OZI rule which these measurements represents is interpreted in terms of the various theoretical models presented in Chapter 2. Also, included in this chapter are the results of a search for the reaction $\pi^+ n \rightarrow K^+ \phi \Lambda^0$ which provides a unique study of the OZI rule since it contains both an OZI allowed diagram and an OZI forbidden diagram. The ϕ , Δ^{++} and Λ^0 are not detected directly but rather inferred from their detected decay products; $\phi \rightarrow K^+ K^-$, $\Delta^{++} \rightarrow p \pi^+$, $\Lambda \rightarrow p \pi^-$. Finally, the results of a search for the phi-prime meson, the first excited state of the $s\bar{s}$ system, are presented.

CHAPTER 2. THEORY

At the present time, there is no theoretical consensus of the OZI rule. There are a number of models proposing a dynamical origin of the OZI rule; however, the predictions from most of these models are not sufficient to distinguish among them. The models may be grouped into two categories - those based on QCD and those based on unitarity and duality. A brief statement of several of the more popular of these models is presented in this section. First, however, a short history of the OZI rule is given in order to define the OZI rule.

History

The wide popularity of the SU(3) model (5) of Gell-Mann is partially due to the success of the mass formulae. For instance, the formula

$$\frac{1}{2} [m(N) + m(\Xi)] = \frac{1}{4} [3m(\Lambda) + m(\Sigma)]$$

for the $J^P = \frac{1}{2}^+$ baryon octet agrees well with experiment. However, the corresponding formula for the vector meson octet

$$m^2(\omega_8) = \frac{1}{3} [4m^2(K^*) - m^2(\rho)]$$

(where ω_8 is the eighth component of the octet) doesn't fare so well. Putting in the experimental masses (6) for the K^* and the ρ , this equation predicts the mass of the $I = Y = 0$ member of the octet (ω_8) to be $m(\omega_8) = 928$ MeV. However, neither of the two particles having the quantum numbers necessary for that state are of the correct mass -

namely, the ϕ which has a mass of $m(\phi) = 1020$ MeV and the ω which has a mass of $m(\omega) = 783$ MeV.

In 1962, Sakurai (7) suggested that the physical ω and ϕ be linear combinations of the eighth component of the octet (ω_8) and the SU(3) singlet state (ω_1).

$$\omega = \omega_8 \sin\theta + \omega_1 \cos\theta$$

$$\phi = \omega_8 \cos\theta - \omega_1 \sin\theta$$

Using the experimental ω and ϕ masses, the mixing angle (6) is determined to be $\theta = 40^\circ \pm 1^\circ$. A number of predictions from this model agree well with experiment so some confidence was placed in the model. However, it also produced the following problem. The ratio of coupling constants in $\phi \rightarrow \rho\pi$ and $\omega \rightarrow \rho\pi$ can be estimated from experimental data to be (8) $(g_{\phi\rho\pi}/g_{\omega\rho\pi})^2 \approx 0.007$. Sakurai's mixing model, however, requires the ratio of coupling constants to be given by

$$\frac{g_{\phi\rho\pi}}{g_{\omega\rho\pi}} = \frac{g_8 \cos\theta - g_1 \sin\theta}{g_8 \sin\theta + g_1 \cos\theta} .$$

In order to get the small value observed experimentally for this ratio, there has to be a large cancellation in the numerator. This suggests that the singlet and octet should not be treated independently as in the SU(3) scheme. So it might be better to place all of the vector mesons on an equal footing and group them into a nonet rather than an octet and a singlet (8). In fact, in SU(6) the vector mesons naturally fall into a nonet. The nonet can be represented by the nontraceless tensor (1)

$$G_{\nu}^{\mu} = \begin{pmatrix} \frac{1}{\sqrt{2}} (\omega + \rho) & \rho^{+} & K^{*+} \\ \rho^{-} & \frac{1}{\sqrt{2}} (\omega - \rho) & K^{*0} \\ K^{*-} & \bar{K}^{+0} & -\phi \end{pmatrix}$$

The nonet ansatz of Okubo, which was the original statement of the OZI rule, was to require that the $\text{Tr}(G)$ not appear in any physical calculation (1). Some justification for excluding the $\text{Tr}(G)$ can be seen by looking at the mass operator. The most general form of the mass operator up to first order in $\text{SU}(3)$ breaking is given by (8)

$$M^2 = \frac{1}{2} M_0^2 \text{Tr}(GG) + M_1 \text{Tr}(GG\lambda_8) + M_2 (\text{Tr}G)(\text{Tr}G) + M_3 (\text{Tr}G)\text{Tr}(G\lambda_8)$$

$$\text{Tr}(G) = \sqrt{2} \omega - \phi = \sqrt{3} \omega_1$$

The nonet ansatz requires $M_2 = M_3 = 0$ since the $\text{Tr}(G)$ can't appear in the calculation by assumption. The effect of including the $\text{Tr}(G)$ would be to give the singlet a different mass than the octet but since the singlet and octet are to be viewed on an equal footing, those terms must be excluded. It should be pointed out that the tensor G has been written with the mixing angle $\theta = \tan^{-1} \frac{1}{\sqrt{2}} \approx 35^\circ$ such that (1)

$$\omega = \frac{1}{\sqrt{2}} (G_1^1 + G_2^2) \quad \text{and} \quad \phi = -G_3^3$$

since the diagonalization of M^2 requires

$$\omega_1 = \frac{1}{\sqrt{3}} (G_1^1 + G_2^2 + G_3^3) \quad \text{and} \quad \omega_8 = \frac{1}{\sqrt{6}} (G_1^1 + G_2^2 - 2G_3^3) \quad .$$

This is called ideal mixing. The following relations are derived from

the mass formula by imposing the nonet ansatz and assuming ideal mixing (1):

$$m^2(\omega) = m^2(\rho)$$

$$m^2(\phi) - m^2(K^*) = m^2(K^*) - m^2(\omega) \quad .$$

These mass formula agree well with experiment.

Okubo also determined the matrix elements T for the decays $\phi \rightarrow \rho\pi$ and $\phi \rightarrow 3\pi$ to be (1) $T(\phi \rightarrow \rho\pi) = 0$ and $T(\phi \rightarrow 3\pi) = 0$ which are two of the more well-known predictions of the OZI rule. These predictions follow immediately from the nonet ansatz but its easier to see them from Zweig's reinterpretation of the ansatz in terms of the quark model.

In 1964, about a year after Okubo's original ansatz, Zweig (3) (and independently Iizuka et al. in 1966 (4)) showed that the tensor G_{ν}^{μ} could be written as $G_{\nu}^{\mu} = q_{\nu} \bar{q}_{\mu}$ where q represents a quark and \bar{q} an antiquark. The indices ν and μ represent the different quarks or antiquarks: $q_1 = u$, $q_2 = d$, $q_3 = s$, In the ideal mixing case then, the ω is made up of u and d quarks and contains no strange quarks. The ϕ consists only of strange quarks. Figure 2.1a shows the decay $\omega \rightarrow 3\pi$ in terms of quark lines. The matrix element for this diagram is part of the $SU(3)$ invariant form $\text{Tr}(GPPP)$ where P is a tensor representing the pseudoscalar octet (8). Compare this with the diagram for $\phi \rightarrow 3\pi$ (Fig. 2.1b). The matrix element is given by $(\text{Tr}(G))(\text{Tr}(PPP))$. Since the $\text{Tr}(G)$ appears, the decay $\phi \rightarrow 3\pi$ must be forbidden by the OZI rule. The $\phi \rightarrow 3\pi$ diagram, however, has disjointed quark lines. This is called a hairpin diagram and all hairpin diagrams are OZI forbidden.

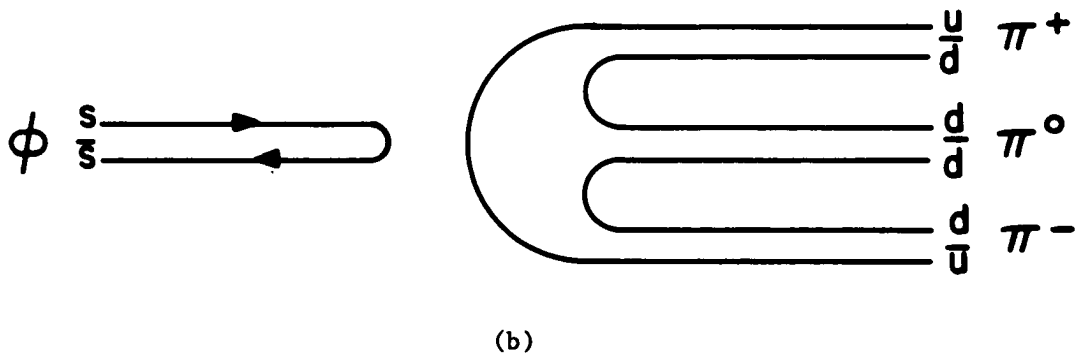
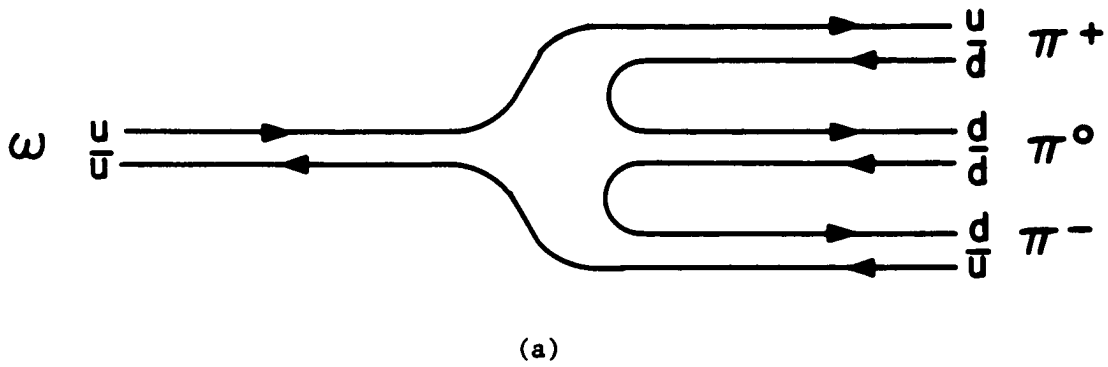


Figure 2.1. Quark line diagrams

(a) OZI allowed decay $\omega \rightarrow 3\pi$.

(b) OZI forbidden decay $\phi \rightarrow 3\pi$.

The predictions of the OZI rule are in general well-satisfied by experiment. Some of the experimental evidence is summarized in Reference 8.

QCD

The OZI rule predicts the suppression of cross sections that would otherwise appear much too small. This is ample motivation for trying to find its theoretical basis. However, recently, the OZI rule has become even more important. It has been invoked to explain the narrow width of several new particles such as the ψ ($\Gamma \approx 0.06$ MeV). The ψ is a bound state of $c\bar{c}$. With its mass of 3.1 GeV, it should have a lot of hadronic decay modes. Figure 2.2 depicts several classes of decays of the ψ that are forbidden by the OZI rule (9).

Without the OZI rule then, the ψ would have many more decay modes and consequently a much larger width. It is important to note that the OZI rule was not contrived as an explanation of the ψ 's narrow width but rather as an explanation of the ϕ 's production and decay properties. However, the rule works better for the ψ than for the ϕ as evidenced by the ψ 's slow decay rate. A possible explanation of this comes from Quantum Chromodynamics (QCD) (10-14). QCD is a color SU(3) gauge theory which tries to explain hadron dynamics. A basic tenet of QCD is the concept of asymptotic freedom which essentially says that the strong interactions get weaker as the energy goes up (or alternately as you examine interactions at closer distances). The strong interactions are mediated by the colored gluons just like the electromagnetic interactions are mediated by the photon. Asymptotic freedom then says that

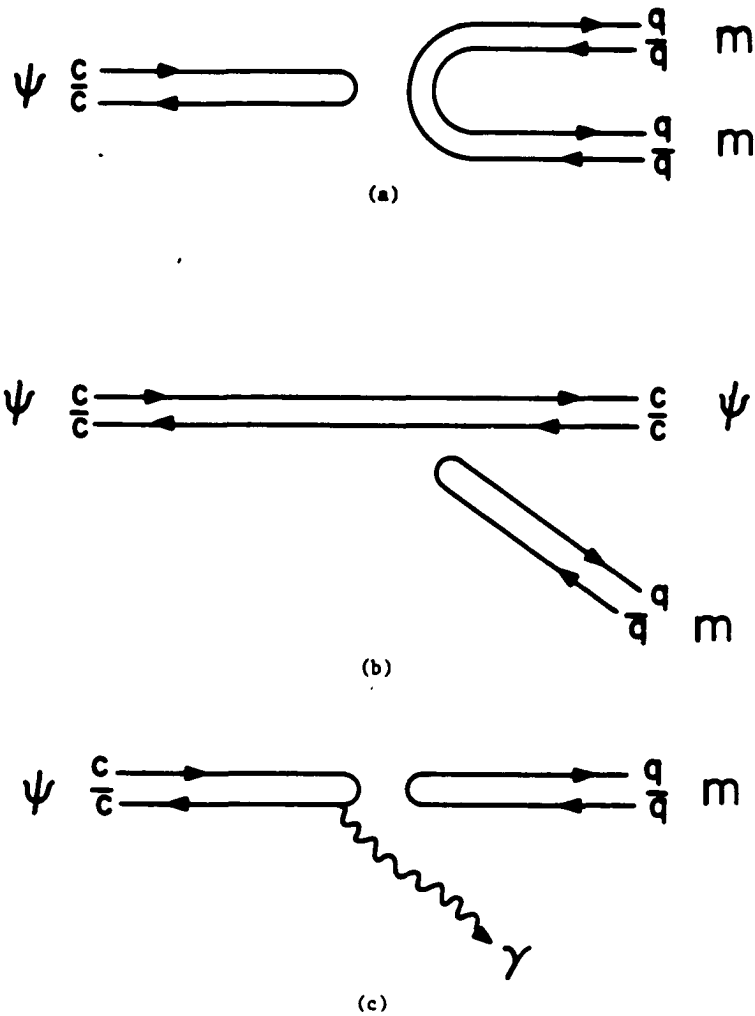


Figure 2.2. OZI forbidden classes of ψ decay. q represents an ordinary quark (u, d, s) and m an ordinary meson (i.e., does not contain charmed quarks)

- (a) $\psi \rightarrow mm$.
- (b) $\psi \rightarrow m\psi$.
- (c) $\psi \rightarrow \gamma m$.

the coupling constant between the gluons and the quarks decreases as the energy increases.

The smallness of the quark-gluon running coupling constant is to be regarded in this theory as the dynamical origin of the OZI rule. For example, consider the decay $\phi \rightarrow 3\pi$ as depicted in Fig. 2.3 according to the field theoretic point of view. The pions are produced from the annihilations of the $s\bar{s}$ quarks via three intermediate gluons. (One and two gluon exchange are forbidden for the decay of a vector particle by color conservation and C parity conservation, respectively.) The energy-momentum carried by the gluons is supposed to be large enough to make the quark-gluon coupling constant small. If that is the case, then the decay can be treated perturbatively with the result that this higher order diagram should be small. QCD's explanation then, of why the OZI rule works better for the ψ than for the ϕ , is simply that since the ψ is much more massive than the ϕ , its quark-gluon coupling constant is expected to be less than the ϕ 's and consequently the OZI rule will hold better for the ψ . QCD predicts $\Gamma_{\phi \rightarrow 3\pi} \approx 10\Gamma_{\psi \rightarrow \text{hadrons}}$ which agrees with experiment (15).

Dual Unitarity

Freund and Nambu (16) have criticized QCD stating that although it predicts overall rates, it is not easily adapted to investigating specific decays. As a result, they have developed a model that replaces the three gluons of the field theoretic models with a new SU(4) singlet vector meson, 0 . The model is developed from dual dynamics and identifies the 0 meson with the 1^- state on the Pomeron

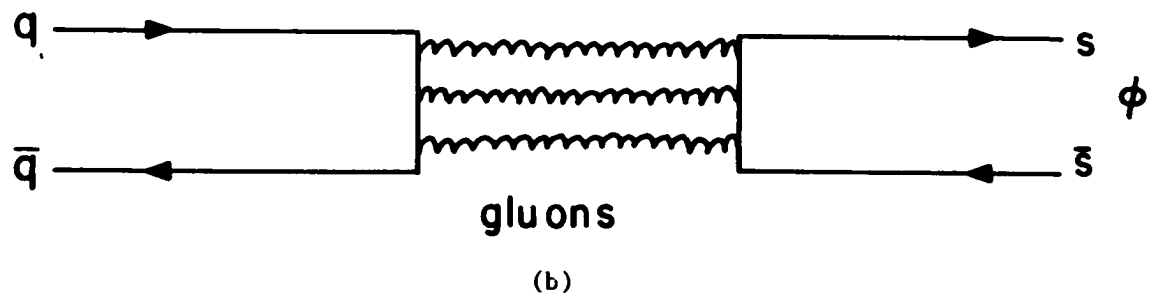
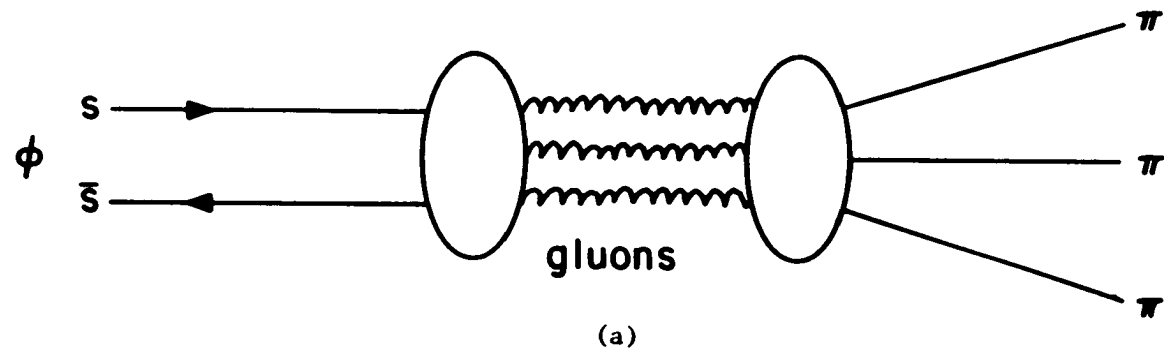


Figure 2.3. QCD gluon exchange

- (a) $\phi \rightarrow 3\pi$.
- (b) $q\bar{q} \rightarrow \phi$.

first daughter trajectory. In this model, the $\phi \rightarrow \rho\pi$ decay occurs as a result of the mixing of the 0 meson with the ψ , ϕ , and ω mesons as shown in the sequential pole diagram of Fig. 2.4.

Both the 0 meson model and the asymptotic freedom model (QCD) have been questioned by Arafune, Fukugita and Oyanagi (17). They begin with the generally accepted assumption that the violation of the OZI rule or the fact that it is not perfectly obeyed is a result of the deviation from ideal mixing. That is, the ϕ is not a pure $s\bar{s}$ state but rather a combination of $\phi_0 = s\bar{s}$ and $\omega_0 = (u\bar{u} + d\bar{d})\frac{1}{\sqrt{2}}$. In other words, the ϕ is produced by its nonstrange component via diagrams such as that in Fig. 2.5. The question then is, what is the mechanism responsible for the deviation from ideal mixing?

An examination of a number of different processes including the Gell-Mann-Okubo mass formula found them all mutually consistent with regard to both magnitude and sign of a mixing parameter $\epsilon = \tan\theta$ where θ is the deviation from ideal mixing defined by

$$\begin{aligned}\phi &= \phi_0 \cos\theta + \omega_0 \sin\theta \\ \omega &= -\phi_0 \sin\theta + \omega_0 \cos\theta \quad .\end{aligned}$$

The sign of ϵ is determined to be positive and the deviation from ideal mixing is only about 5.5° . The mixing of states is assumed to be a result of a unitarity correction. The unitarity correction can be described in the following manner. The decay $\phi \rightarrow \pi\rho$ is forbidden by the OZI rule (Fig. 2.6a). The decay $\phi \rightarrow K\bar{K}$ is allowed, however, as is the reaction $K\bar{K} \rightarrow \rho\pi$ (Fig. 2.6b). The reaction $\phi \rightarrow K^+K^- \rightarrow \pi^-\rho^+$ is then

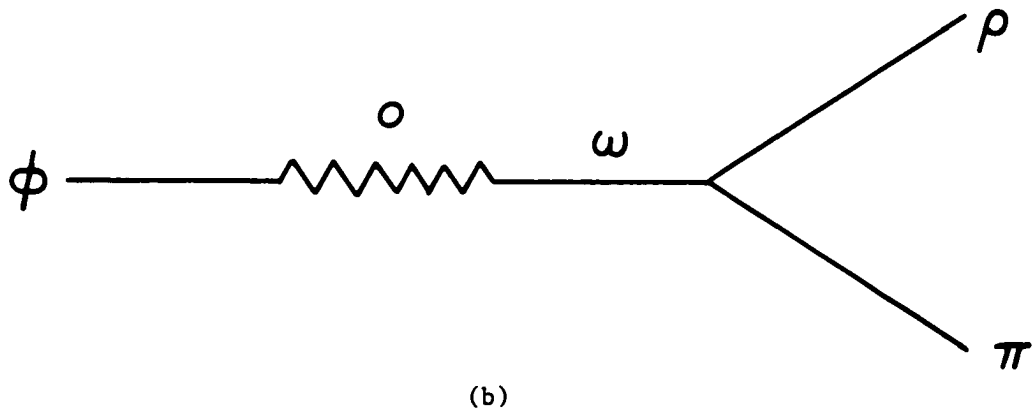
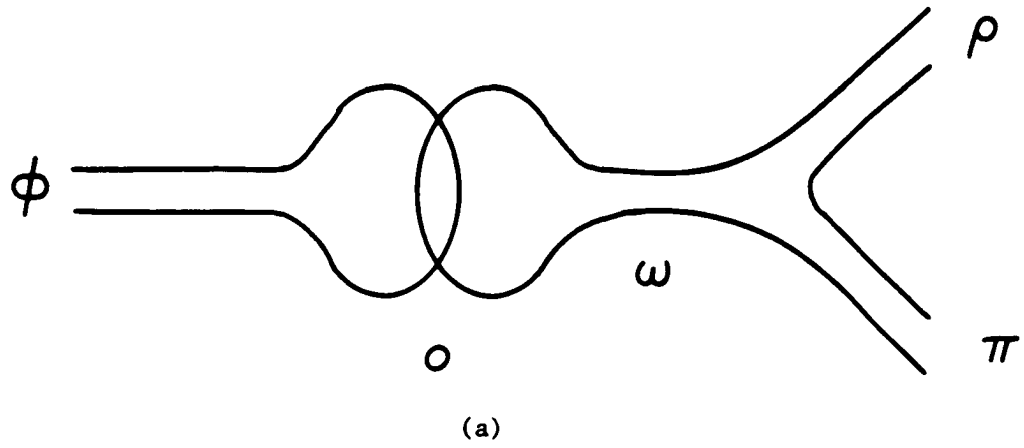


Figure 2.4. The decay $\phi \rightarrow \rho\pi$ in terms of the 0 meson model

(a) Nonplanar duality diagram.

(b) Sequential pole diagram.

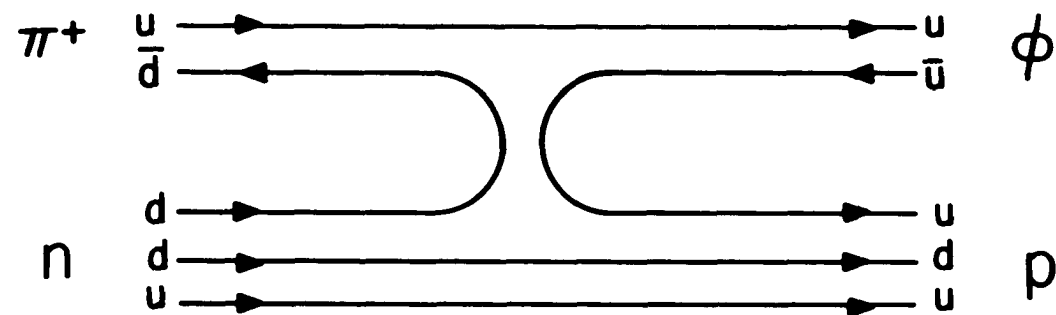


Figure 2.5. Nonstrange phi production in the reaction $\pi^+ n \rightarrow \phi p$

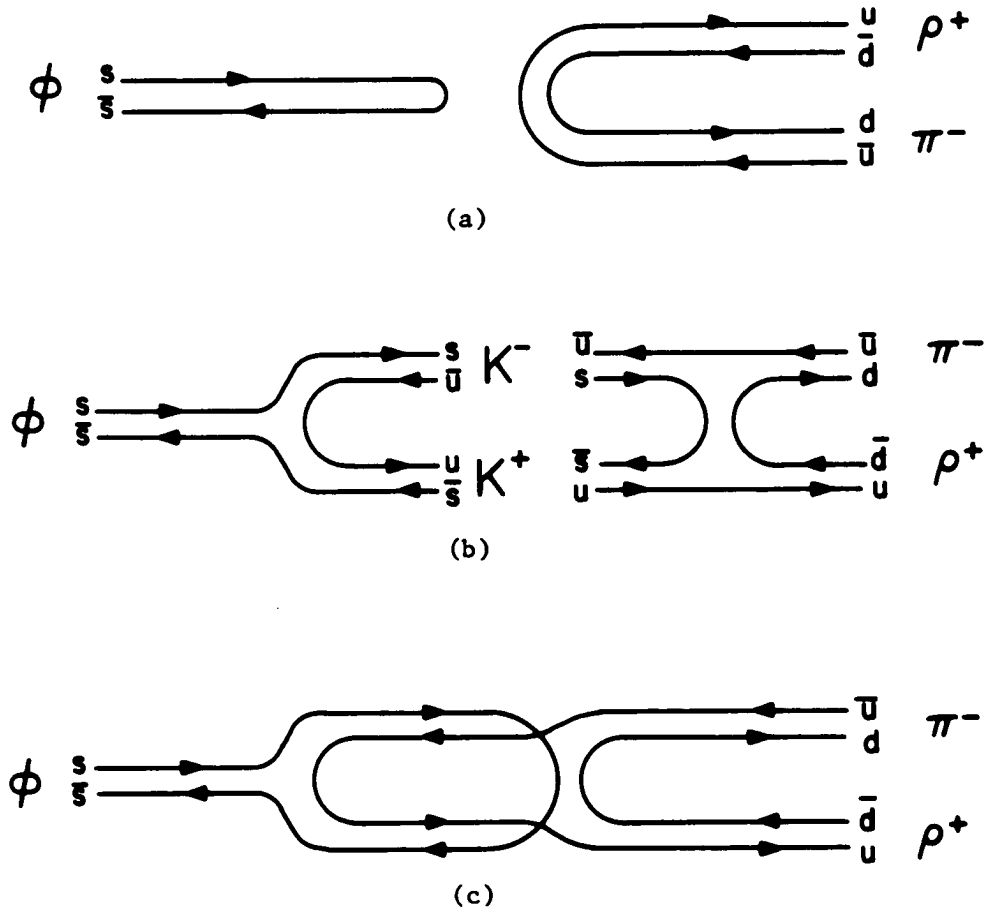


Figure 2.6. Higher order paradox

- (a) OZI forbidden decay $\phi \rightarrow \pi^- \rho^+$
 (b) OZI allowed processes $\phi \rightarrow K^- K^+$ and $K^- K^+ \rightarrow \pi^- \rho^+$
 (c) OZI forbidden higher order process $\phi \rightarrow K^- K^+ \rightarrow \pi^- \rho^+$.

expected to occur. The K's are peculiar in that they contain both a strange and a nonstrange quark and as such can provide a link between the completely strange ϕ system and the completely nonstrange $\pi\rho$ system.

Figure 2.6c is a diagram for the higher order process. Note that if the left side of the diagram is pulled away from the right side, the result is the disconnected hairpin diagram of the one step process of Fig. 2.6a. In fact, any hairpin diagram can be made into a connected diagram by just pushing the two sides together. In order to save the quark line interpretation of the OZI rule then, all diagrams with twisted lines must be forbidden (18). In other words, if a kaon was produced by a strange system then it can't decay into nonstrange particles. This means that there must be two distinct types of kaons - those produced from strange systems and those produced from nonstrange systems. The problem is, however, that the physical kaons have no such distinction. The conclusion is then, that in fact, these diagrams must occur (19). These diagrams are then demanded by the unitarity equation

$$\text{Im } T(i \rightarrow f) = \sum_n T^*(f \rightarrow n) T(i \rightarrow n) \delta(E - E_n)$$

and unitarity thus requires OZI violation. The small violation of the OZI rule then must be due to other intermediate states whose amplitudes just cancel the one in question. Thus, the unitarity correction is the inclusion of more intermediate states in the unitarity equation.

Arafune et al. express the mixing parameter ϵ in terms of a perturbation expansion of the transition amplitude (17) $T(\phi_0 \rightarrow \omega_0)$ of $\phi_0 \rightarrow \omega_0$,

$$\epsilon = \frac{T(\phi_0 \rightarrow \omega_0)}{m_\phi - m_\omega} = \sum_i \frac{\langle \phi_0 | H | i \rangle \langle i | H | \omega_0 \rangle}{m_\phi - m_i m_\phi - m_\omega}.$$

The intermediate states i are brought in as a result of the unitarity correction. The major contribution to ϵ comes from intermediate states such as $K\bar{K}$, $K\bar{K}^*$, $K^*\bar{K}^+$, etc. where m_i is generally greater than m_ϕ . Thus, the matrix element should be negative to give ϵ positive. Noting that SU(3) octet intermediate states produce a negative matrix element and SU(3) singlet states produce a positive matrix element, the conclusion is that the intermediate states must be dominated by SU(3) octet states. The 0 meson model, however, gives a negative sign for ϵ since the 0 meson is an SU(3) singlet. The QCD model, where transitions are mediated by three flavor SU(3) singlet gluons, also has a difficult time producing a positive sign for ϵ (although the possibility hasn't been ruled out because of a possible contribution from different intermediate states).

There are, however, several models which give the correct sign for the ω - ϕ mixing parameter. One of these is a model by Schmid, Webber, and Sorensen which links the OZI rule with exotic exchanges and unitarity (20). They have shown that the suppression of exotic exchanges is the result of the cancellation of amplitudes from particles of opposite charge conjugation. This same cancellation mechanism suppresses OZI violating transitions. In duality diagrams, this is equivalent to the suppression of twists in produced lines. The suppression of exotic exchanges requires the suppression of OZI violating transitions in order to satisfy unitarity. This is the dynamical

origin of the OZI rule in their model. The degree to which exotic exchanges occur gives a measure of the violation of the OZI rule. For instance, the following predictions are made (20):

$$\frac{g^2(\psi\rho\pi)}{g^2(\omega\rho\pi)} = 2 \times 10^{-3} \quad ; \quad \frac{g^2(\psi\rho\pi)}{g^2(\phi\rho\pi)} = \frac{1}{100} \quad ; \quad \frac{g^2(\psi\rho\pi)}{g^2(\omega\rho\pi)} = 2 \times 10^{-5}.$$

It has also been shown (21) that this cancellation mechanism is not valid for the central region and consequently suppression of OZI forbidden diagrams is weaker for central production than for peripheral production. This claim appears to be born out experimentally (22).

A second model which gives the correct sign for the ω - ϕ mixing parameter is the asymptotic planarity model of Chew and Rosenzweig (23). In this model, nonplanar components are associated with the breaking of ideal mixing. It is argued that with increasing t (where t is the 4-momentum transfer), these nonplanar diagrams become less and less important. This tendency toward planarity (or ideal mixing) with increasing t is called asymptotic planarity and is the S-matrix analog of the field theoretic asymptotic freedom. The precociousness of the asymptotic behavior, while unresolved in QCD, is naturally accounted for in this model.

Confounded Confusion

It is also possible that, while the nonstrange component of the ϕ as predicted by the deviation from ideal ω - ϕ mixing may account for a great deal of the ϕ production, it may not be the only mechanism for producing ϕ 's in OZI forbidden reactions. The now fashionable quark

fusion models (24-32) entertain just this idea. Proponents of quark fusion models begin by assuming Sakurai's mixing model predicts the nonstrange component of the ϕ and then include other mechanisms according to their predilections. One such mechanism is shown in Fig. 2.7. The target and projectile are assumed to be surrounded by seas of quark-antiquark pairs. An s and an \bar{s} quark are pulled from these seas and "fused" together to form the ϕ . The probability of producing the ϕ in this manner is given by (28)

$$\frac{2E}{\sqrt{s}} \frac{d\sigma}{dx} = \frac{8\pi^2}{M_\phi^2} \frac{g_s^2}{4\pi} S_s^{H_1(\xi_1)} S_s^{H_2(\xi_2)} \quad (2.1)$$

where $S_s(\xi)$ is the strange sea quark distribution function and ξ is the fractional momentum of the strange sea quark. x is the Feynman variable.

Fritzsch (30), however, argues that this mechanism is unimportant because there are likely to be very few strange quarks in the sea. He, therefore, describes two other epicycles as shown in Fig. 2.8. Both of these mechanisms produce an $s\bar{s}$ pair from the decay of a virtual gluon. In Fig. 2.8a, the virtual gluon is formed by the fusion of ordinary quarks and in Fig. 2.8b, it is formed by the fusion of two gluons. Obviously, QCD provides the framework for the various mechanisms considered in the quark fusion model. The relative importance of these various mechanisms has yet to be determined experimentally.

Another possibly important mechanism for ϕ production is the Drell-Yan process shown in Fig. 2.9. Here a quark and antiquark annihilate to form a ϕ (or other 1^- meson) via an intermediate photon.

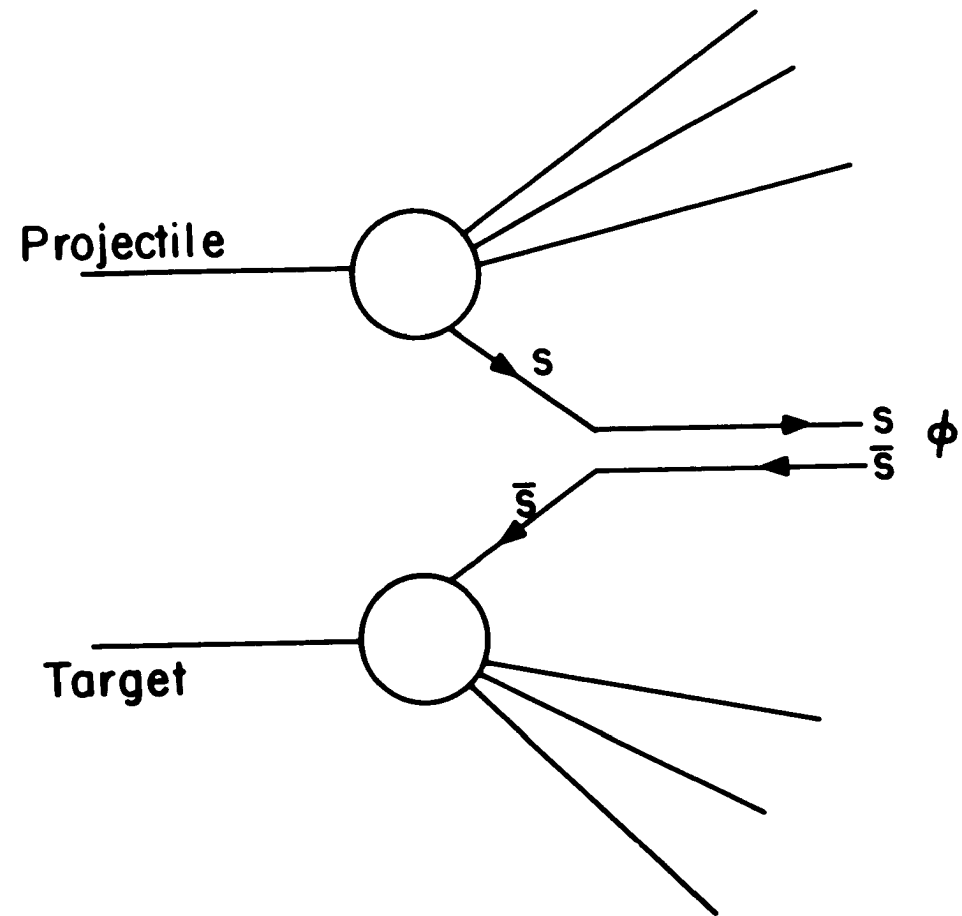


Figure 2.7. Quark fusion model. Fusion of strange sea quarks to form a ϕ

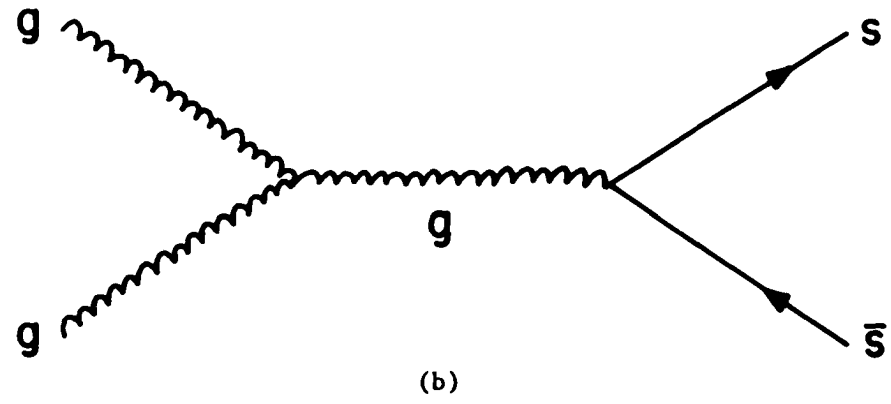
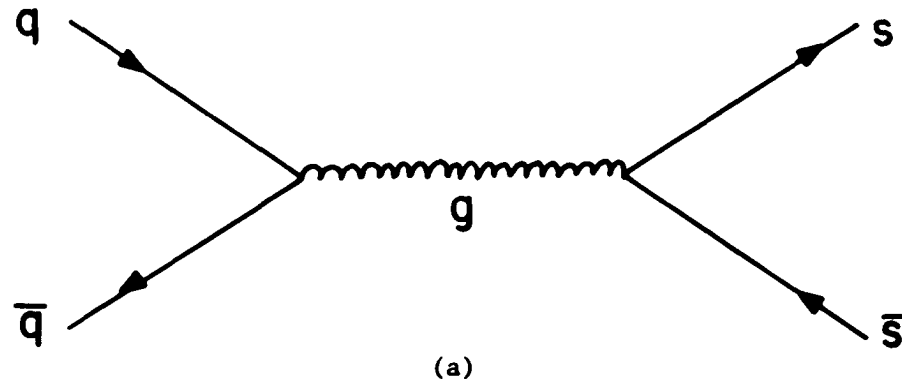


Figure 2.8. $s\bar{s}$ production by virtual gluons in the quark fusion model
 (a) Formation of virtual gluon by fusion of ordinary quarks and anti-quarks.
 (b) Formation of virtual gluon by gluon fusion.

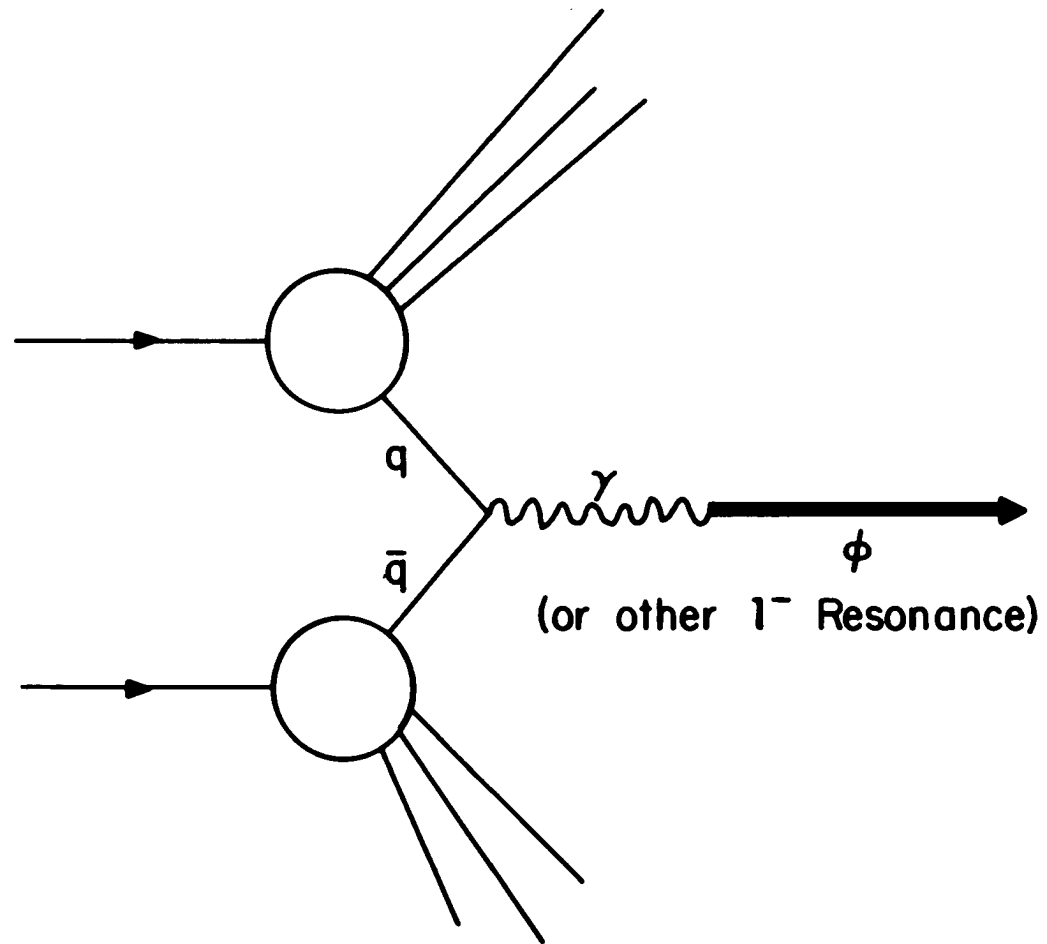


Figure 2.9. Drell-Yan model

Summary

The basic assumption is that the OZI rule would hold exactly if there were ideal mixing. However, empirically there is a deviation from ideal mixing and thus the OZI rule is violated. Several possible mechanisms for the deviation from ideal mixing have been presented. The QCD model attributes the small deviation from ideal ω - ϕ mixing to the smallness of the quark-gluon coupling constant. The 0 meson model mixes the 0 meson with the ω , ϕ , and ψ . Omega-phi mixing in the model of Schmid, Weber, and Sorenson is the result of cancellations among various intermediate states in the unitary sum. The asymptotic planarity model of Chew and Rosenzweig mixes Regge trajectories.

The models divide into two categories, QCD and dual unitarity, based on the framework in which they are developed. Indeed, they do provide a dynamical basis for the OZI rule; in fact several, and it is now necessary to test the predictions of the various models. The models are not mutually exclusive and in fact exhibit many striking similarities; it is therefore quite plausible that they might be fundamentally related.

An additional complication to understanding the OZI rule arises from the possible contribution to phi production in OZI forbidden reactions from other mechanisms for which the OZI rule is not valid (i.e., Figs. 2.7, 2.8 and 2.9). The relative strengths of these mechanisms are only poorly known; for instance, contributions due to the diagrams of Figs. 2.7 and 2.8 are given by expressions such as Eq. (2.1) which requires the knowledge of the quark and gluon

distribution functions which are very poorly known for sea quarks and gluons. It seems likely that with the current imprecision in the parameters of the quark fusion model, it will be capable of "explaining", once given, any new data on the OZI rule in a manner reminiscent of the Ptolemaic system.

The present experiment has measured the cross sections for the OZI forbidden reactions $\pi^+ n \rightarrow \phi p$ and $\pi^+ p \rightarrow \phi \Delta^{++}$ and finds them consistent with being produced solely through the nonstrange component of the phi as predicted by the deviation from ideal mixing.

CHAPTER 3. EQUIPMENT

The experiment was conducted at the Large Aperture Solenoid Spectrometer (LASS) at the Stanford Linear Accelerator (SLAC). A general layout of the apparatus is shown in Fig. 3.1. The LASS facility was designed and built by Group B at SLAC, with contributions from Johns Hopkins University and Cal Tech. Since we were not involved in the construction of the apparatus, the description of the equipment shall be limited to that necessary for an understanding of this experiment. More detailed information may be found in References 33-42.

The strength of the detector was in its large geometrical acceptance (almost 4π) and its high momentum resolution over a large range of both transverse and longitudinal momenta. A solenoid spectrometer provided measurements of particle trajectories with large production angles and relatively low momentum. High momentum particles with small transverse momentum were measured in the downstream dipole spectrometer. Information found in the dipole spectrometer was linked to that in the solenoid spectrometer by a series of detectors located between the two spectrometers. This region was known as the "twixt" region. Particle identification was established by two Cherenkov counters and a time-of-flight counter. The coordinate system used in this experiment was defined as follows: the positive z-axis was taken along the direction of travel of the beam (left to right in Fig. 3.1); the positive y-axis was defined as the upward vertical to the earth's surface and the x-axis was defined such that the coordinate system was right handed. The following sections briefly describe the apparatus.

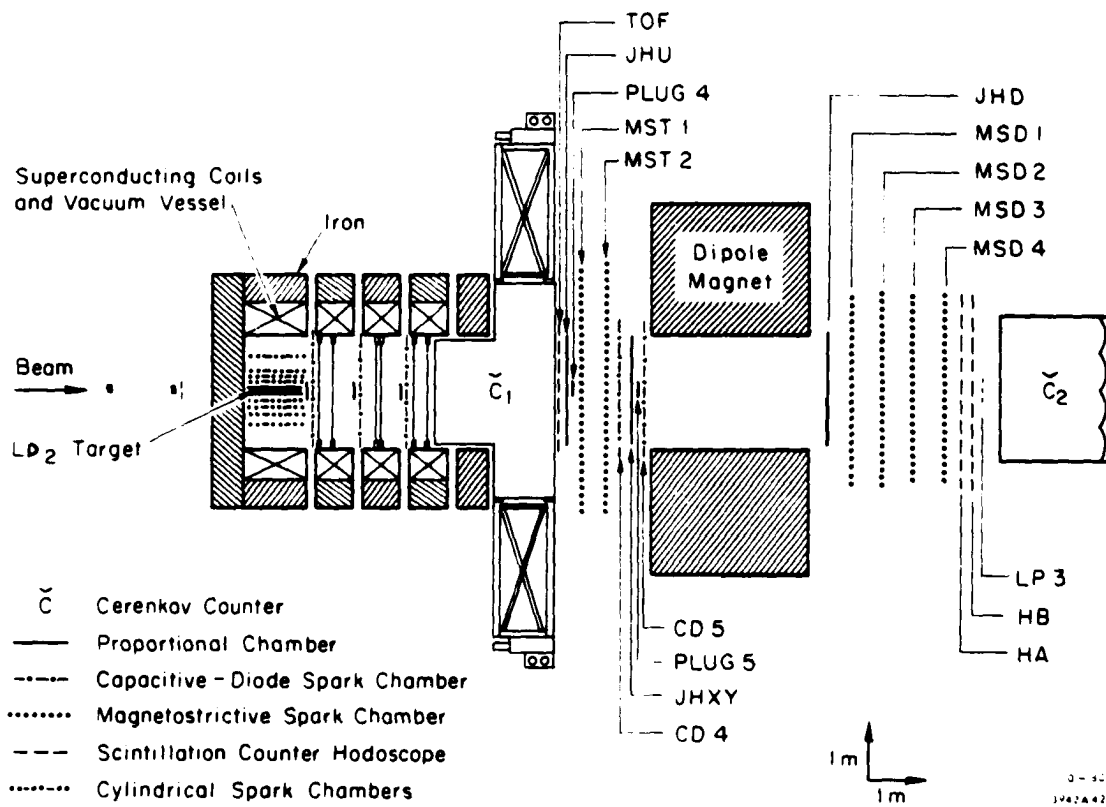


Figure 3.1. Overhead plan view of spectrometer

The Beam

The main accelerator produced a 180 Hertz 1.6 μ sec pulse of electrons. Beamline 20-21 delivered the beam particles to the LASS site as shown in Fig. 3.2. Before striking the .85 radiation length beryllium target, the electron shower was enhanced by a .22 radiation length copper radiator. Dipole magnet 20D1 was used to select a momentum of 10 GeV/c with $\Delta p/p \sim 2\%$ (fwhm). The final beam momentum was measured to within $\Delta p/p = 0.25\%$ by the P hodoscope located at a dispersed focus in beamline 21. Lead filters reduced the electron contamination ratio to $e^-/\pi \sim 10^{-6}$. Two RF separators were available for particle selection but were not used in this experiment because pions already made up 94% of the beam. Particle identification was provided by two Cherenkov counters, C_π which registered pions only, and C_K which detected both pions and kaons. Both counters were insensitive to protons. Thus, the logic for a pion beam was $C_\pi \cdot C_K$.

Beam track finding information was provided by the θ - ϕ hodoscope, the X-Y counter, and the beam proportional wire chambers (PWC). The beam proportional chambers were located in front of the deuterium target, the X-Y counter was located one meter upstream of the target, and the θ - ϕ scintillation counter hodoscope was positioned 40 feet upstream from the beam proportional chambers. It consisted of 24-1/2 inch wide strips of scintillator with half of the strips arranged horizontally and half arranged vertically. The X-Y counter was composed of four small scintillators arranged in a square. The X-Y counter was also used in

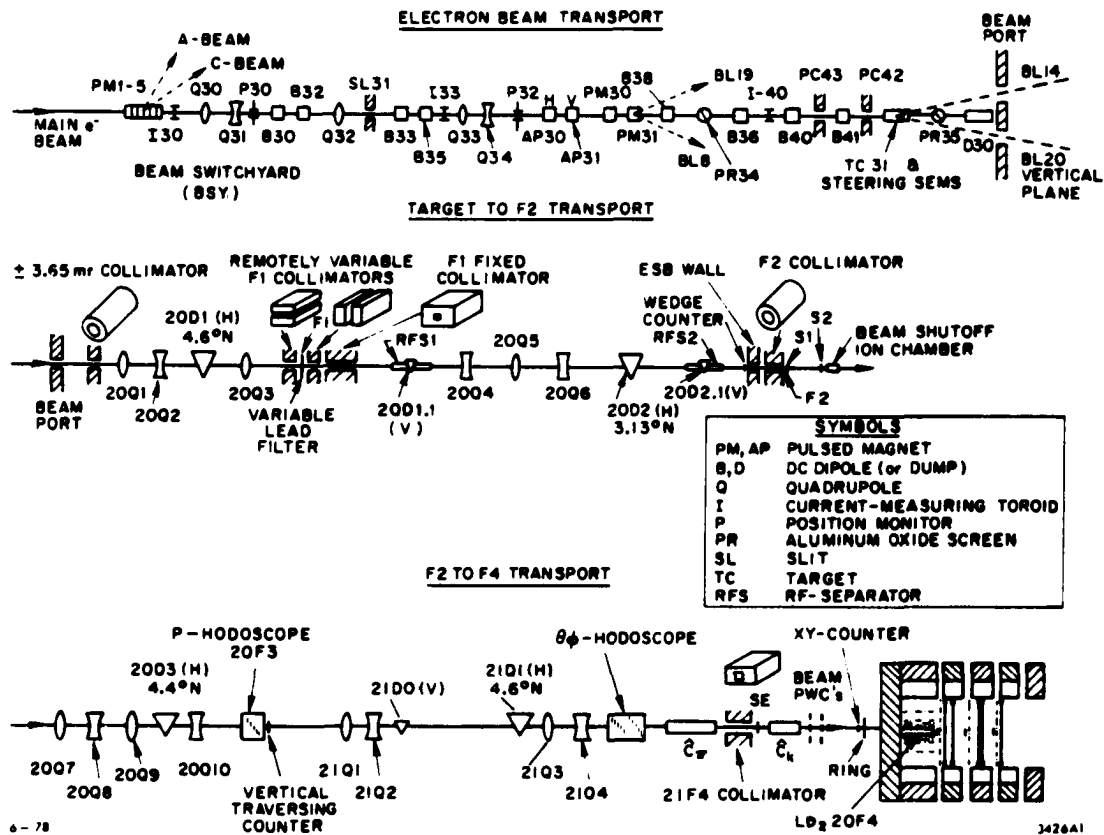


Figure 3.2. LASS beamline

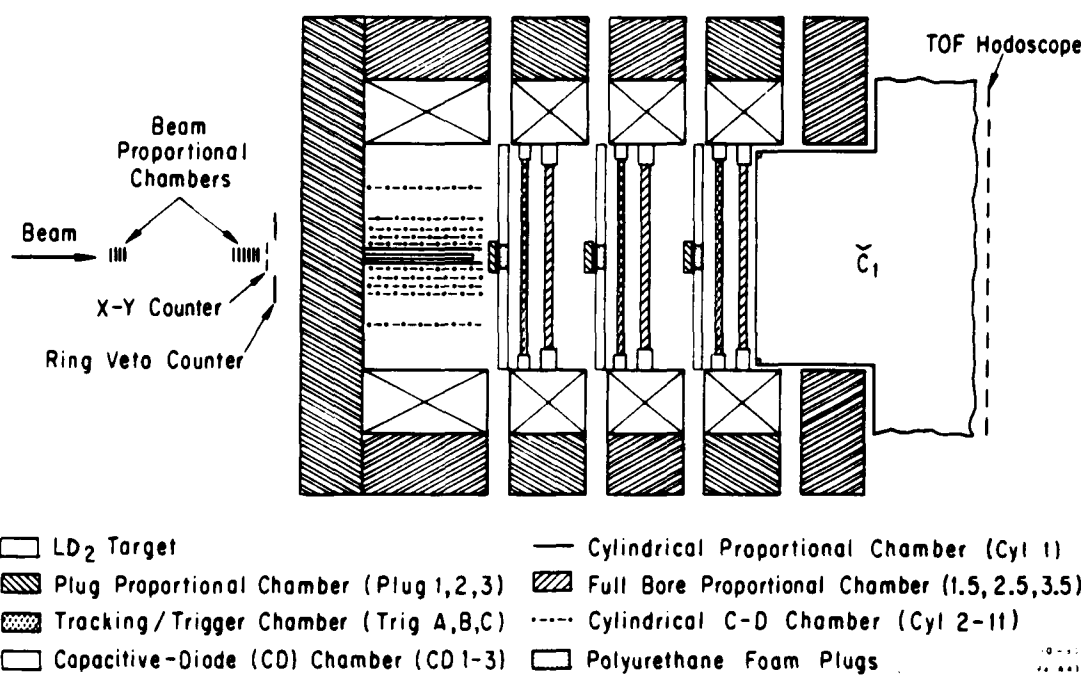


Figure 3.3. Detail of solenoid region

conjunction with the RING counter (a scintillation counter surrounding the X-Y counter) as part of the beam logic to reject beam halo particles and to make certain that the beam particle entered the target. The beam proportional chambers consisted of two groups of four planes separated by one meter and provided X,Y,E,P information (horizontal, vertical, and $\pm 45^\circ$). This arrangement located the beam particle to within 1.0 mm.

The Yardmux computer system, consisting of a Data General NOVA computer monitored all of the magnets in the beamline and controlled their currents to within 1% of their accepted value. The final settings for the beam system provided 2.5 pions per accelerator pulse.

Solenoid Spectrometer

The solenoid spectrometer consisted of the target, a superconducting solenoid magnet giving a field along the beam axis, a series of cylindrical detectors surrounding the target called the vertex detector, and a number of plane capacitive-diode (C-D) and proportional wire chambers located within the solenoid magnet.

Target

The liquid deuterium target was located at the upstream end of the solenoid magnet. The liquid deuterium was continuously circulated through a cell 36 inches long and $2 \frac{1}{16}$ inches in diameter. The temperature and vapor pressure of the deuterium were recorded at the beginning of each run and were used to compute the amount of deuterium in the target.

Solenoid magnet

The solenoid magnet was cooled to the superconducting state by liquid helium. It produced a uniform magnetic field along its axis of 22.4 kilogauss and required a current of 1600 amps. It consisted of four superconducting coils with six-inch gaps separating the coils to allow C-D and proportional wire chambers to be inserted into the solenoid. The coils were enclosed in an iron casing which provided a flux return. The length of the magnet was 465 cm and it had an inside diameter of 185 cm. Both ends of the magnet were capped with flux return mirrors and the nonuniformity of the field within the solenoid was only about 1%.

Vertex detector

The vertex detector consisted of six cylindrical chambers arranged around the target. This arrangement of detectors was particularly important for measuring interaction products produced at a large angle with respect to the beam. The wire spacing of all the detectors except the largest chamber was 2 mm. The largest chamber had a wire spacing of 4 mm. The chamber closest to the target was a proportional chamber and the other five chambers were C-D readout spark chambers. The PWC provided good spatial and time resolution and was incorporated into one of the triggers. Each of the five spark chambers had two gaps with three read-out planes providing a total of fifteen planes. The plane arrangement is shown in Fig. 3.4. The first gap of each chamber has two sets of wires crossed at small angle. The second gap resolved ambiguities resulting from multiple sparks. The result of this arrangement was that the ϕ -coordinate was measured well at the expense of z-coordinate precision.

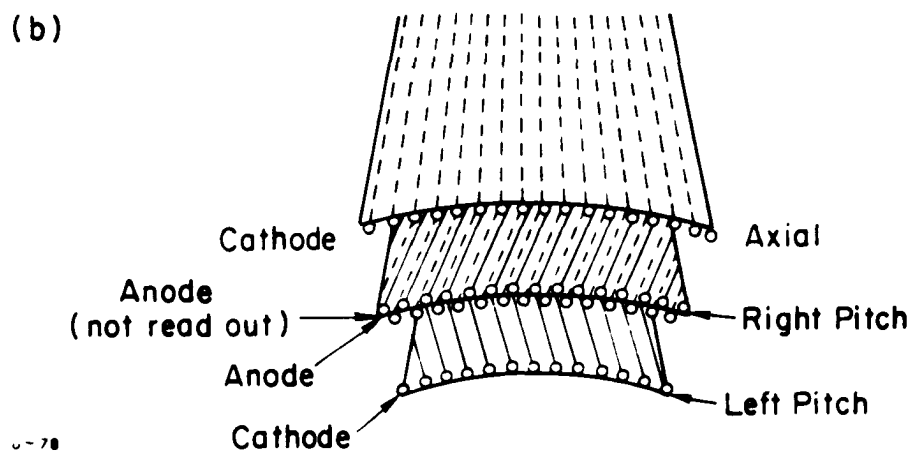
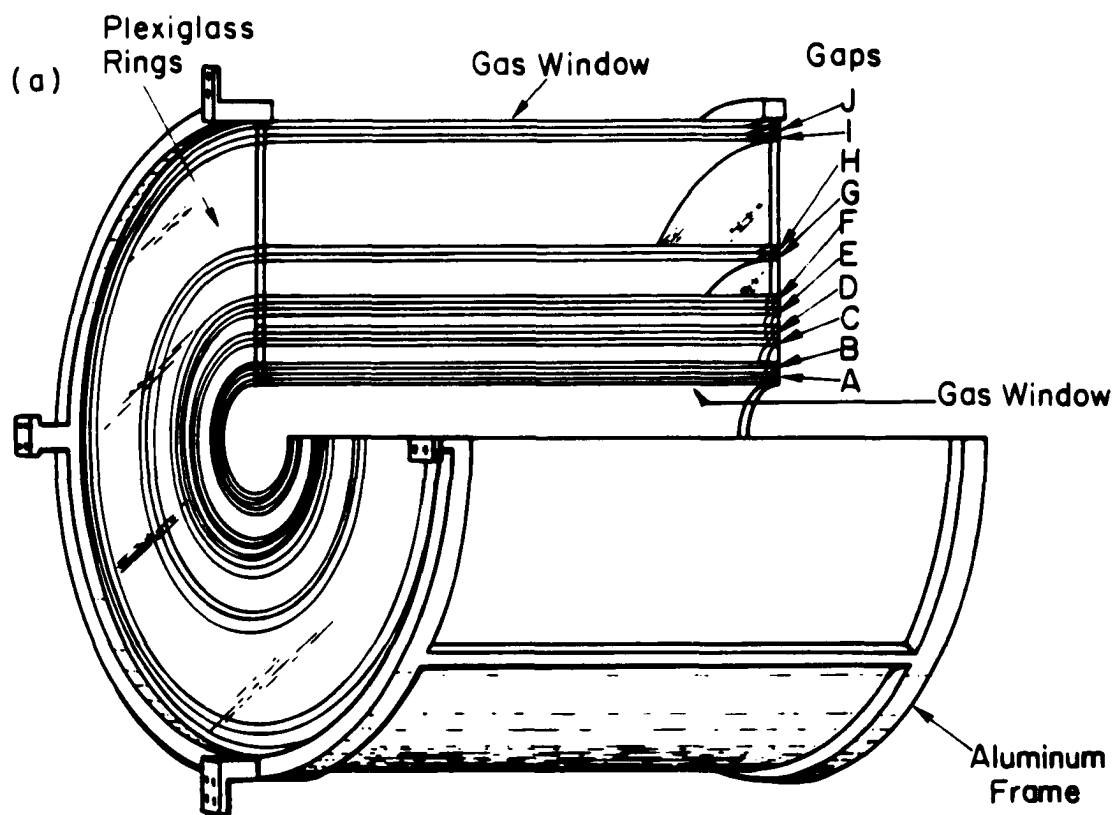


Figure 3.4. Vertex detector

(a) Overall view.

(b) Detail of plane orientation

Plane chambers

There were 12 plane chambers in the solenoid. Three of these were capacitive-diode spark chambers and the remainder were proportional wire chambers. The spark chambers functioned in conjunction with three proportional plug chambers. The spark chambers were desensitized in their central region because of their inability to handle the high flux of particles in that region. A plug chamber whose sensitive area covered this hole, was positioned next to each C-D chamber. Thus, the plug chamber with its fast time response and good multispark efficiency measured the small angle particles and the C-D chamber with a wire spacing of 28 wires per inch provided good spatial resolution for larger angle tracks. The C-D chambers had two gaps and X,Y,E,P readout (horizontal, vertical, $\pm 30^\circ$ to vertical). The plug chambers had a wire spacing of 1.016 mm and three gaps with X, Y, and E readout (horizontal, vertical, 35° to vertical).

There were also three full bore proportional chambers that provided in-time information. Each chamber had three gaps and measured X, Y, and E coordinates (E: 45° to vertical). Finally, there were three proportional wire trigger chambers. Each had one wire plane and an etched cathode foil which provided radial and aximuthal information. The ϕ resolution was 2.81° except for the inner portion of TA where it was 5.62° .

Twixt Region

The twixt region is that region between the solenoid magnet and the dipole magnet. Detectors in this region performed three major functions. First, a Cherenkov counter and a Time-of-Flight counter provided particle

identification. Second, both the Cherenkov counter and the TOF counter were in-time elements and thus could be used in the trigger logic. Third, a series of four spark chambers, two proportional plug chambers and a large PWC provided the track information necessary to link tracks found downstream of the dipole to tracks found in the solenoid. There was also a proportional hodoscope in this region; however, a wire had burned out and, although it remained in place, it was inoperative during the experiment.

Plane chambers

Two of the spark chambers were C-D readout and two were magnetostrictive readout. The two C-D spark chambers and the two plug chambers were identical to those in the solenoid region and previously described in that section.

The magnetostrictive spark chambers each had two gaps and four planes giving X, Y, E, and P information. They were desensitized in the center to allow the beam to pass through. The magnetostrictive wands were fitted with biasing coils to counteract the fringe fields of the solenoid and dipole magnets.

The PWC (JHXY) consisted of a vertical plane of 4 mm spaced wires and a coarser series of 2.8 cm spaced horizontal cathode readout strips. It was used primarily to assist in track finding and to discriminate between in-time and out-of-time tracks.

C1 Cherenkov counter

The Cherenkov counter, C1, was located directly downstream of the solenoid and in fact was fitted with a snout that extended almost to PWC 3.5 inside the solenoid. The purpose of this extension was to improve the efficiency of C1 by increasing the amount of radiator. A diagram of the counter is shown in Figs. 3.5 and 3.6. C1 was a segmented Cherenkov counter with 38 separate cells. There were three radial rings each made up of 12 cells. The two remaining cells were located in the center along the beam axis. The light from each cell was reflected by aluminized mylar mirrors into extension tubes and finally focused by Fresnel lenses onto phototubes at the ends of the extension arms. The purpose of the extension arms was to move the phototubes out of the fringe field of the solenoid. In addition, the phototubes were encased in iron and mu metal for shielding and fitted with bucking coils to compensate for any remaining magnetic field. The insides of the cells and the extension tubes were coated with aluminized mylar to improve reflectivity. All of the cells were oriented such that they pointed back to the center of the target in order to maximize the probability of a fast particle travelling through only one cell. The counter was filled with Freon 12 at atmospheric pressure. This gave a pion threshold of 3.0 GeV/c and a kaon threshold of 10.6 GeV/c. Protons should not make light with only a 10 GeV/c beam.

Discriminated signals from every phototube were added together and the resulting signal became a very important part of the main physics

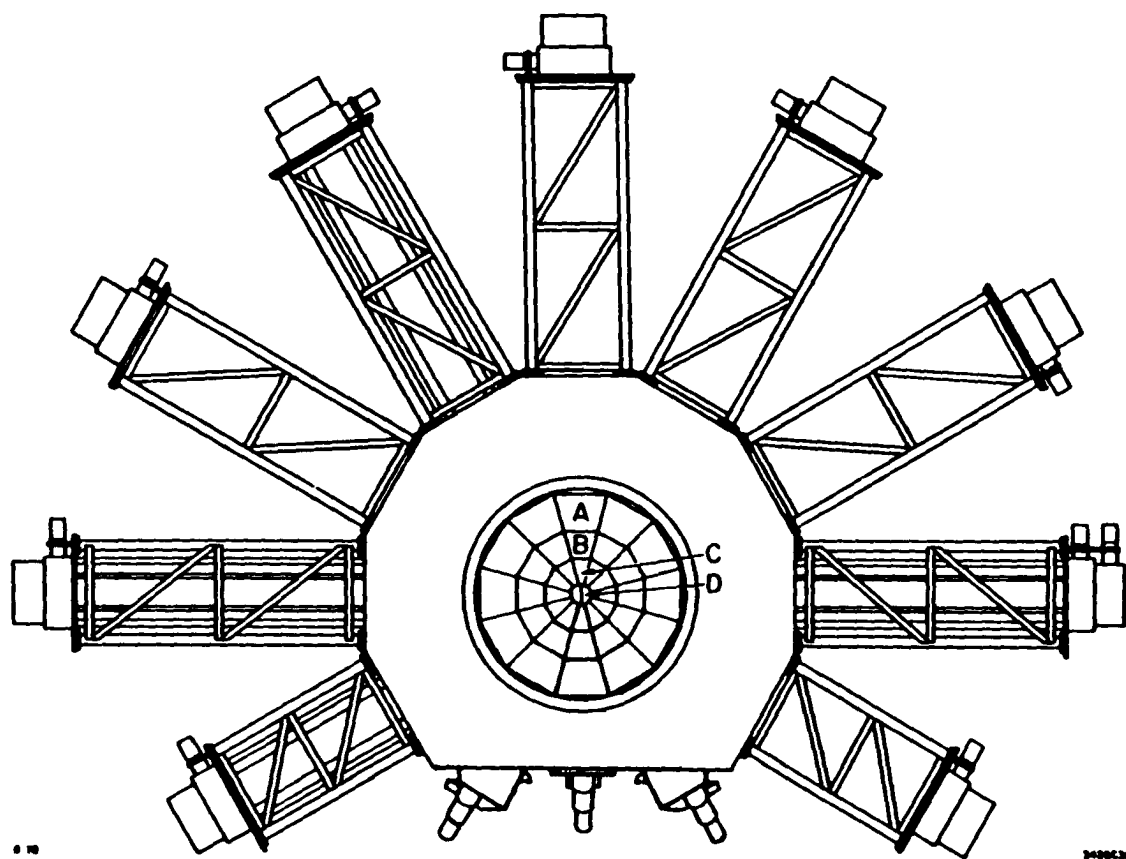


Figure 3.5. Cherenkov counter C1 (looking down beam)

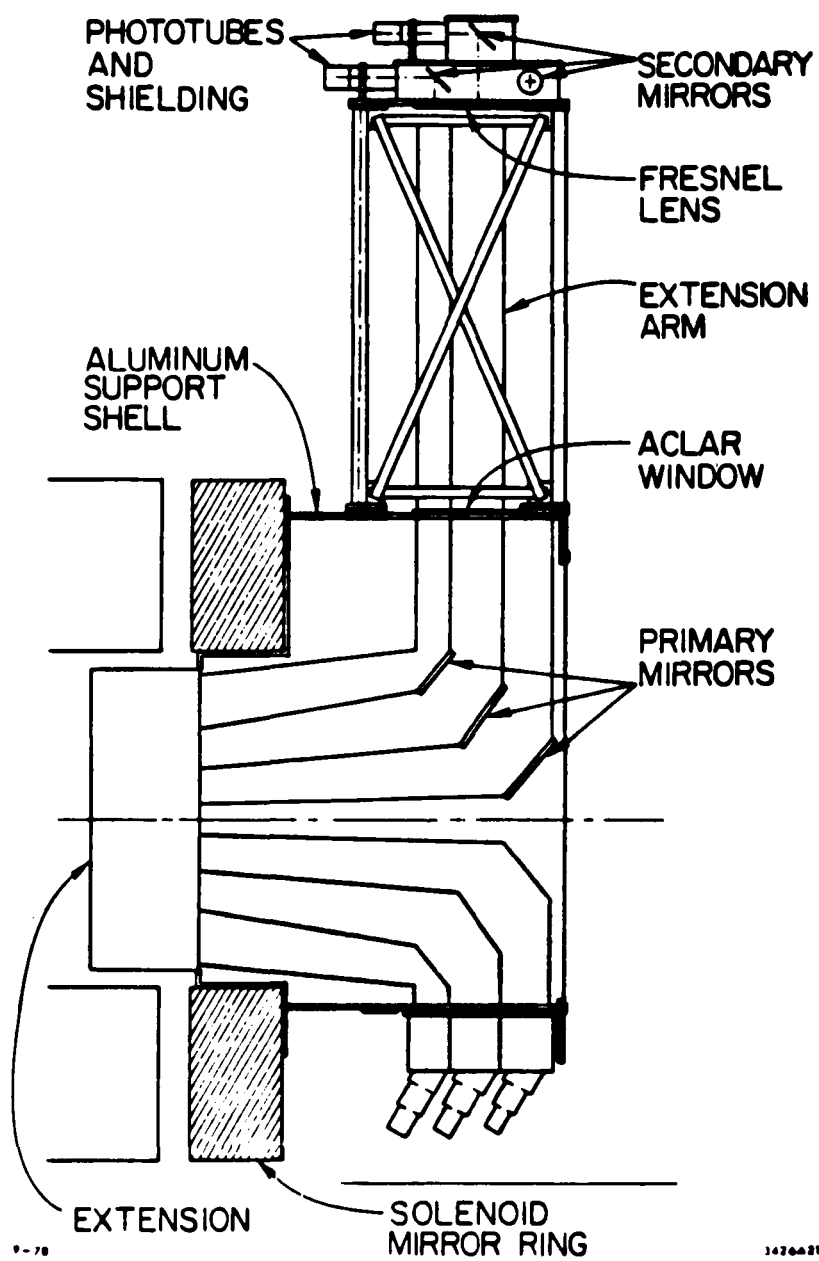


Figure 3.6. Side view of Cherenkov counter C1

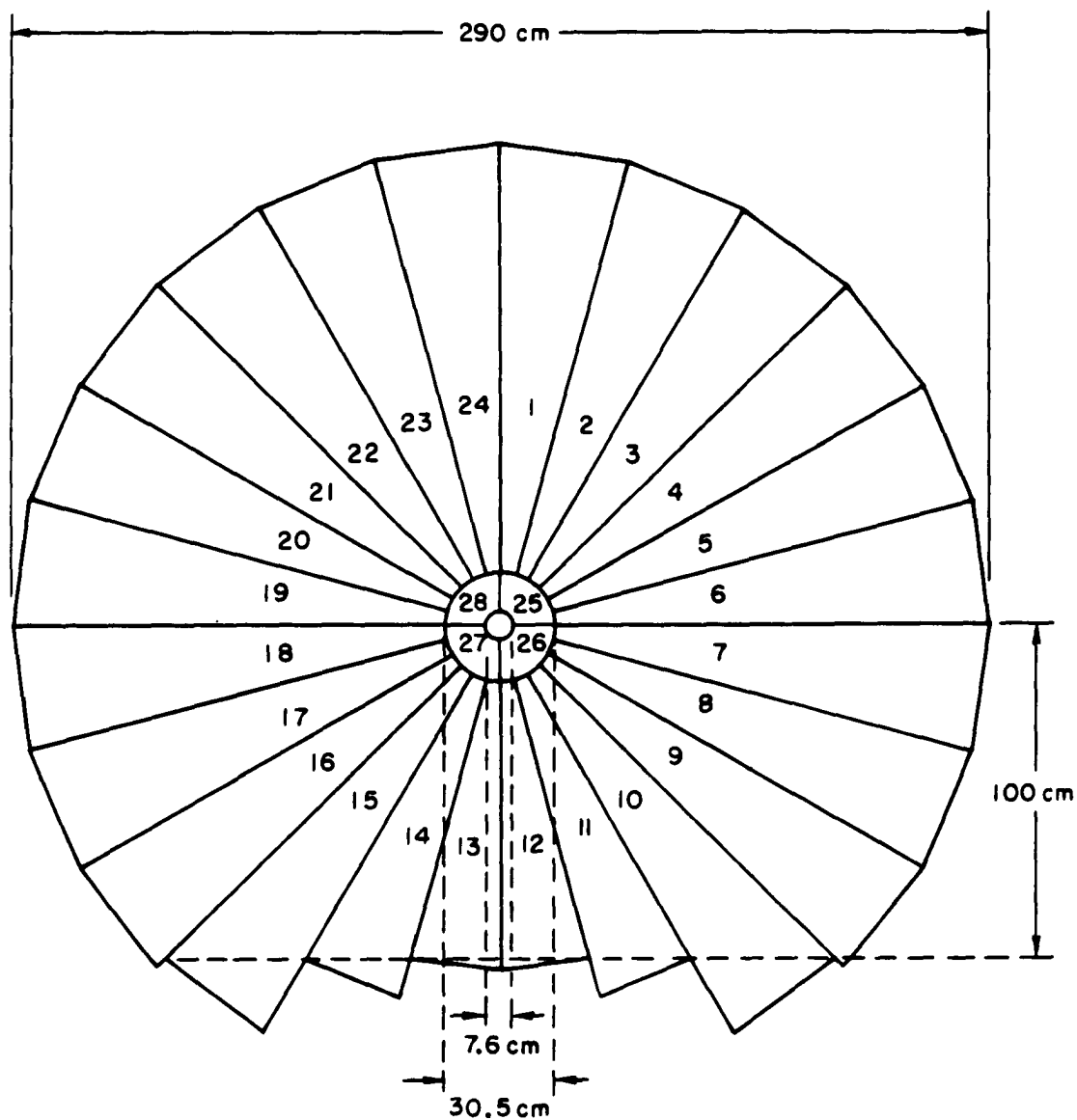
trigger. The ability of C1 to distinguish pions from kaons was a vital part of the experiment. Therefore, a series of low energy runs were made to study the efficiency of C1. Data were collected at 2.5, 3.5, 4.5, 5.5, and 10 GeV/c with both positive and negative pion beams. The results of a subsequent study of this data are contained in the Appendix.

Time-of-Flight counter

The TOF counter consisted of 24 scintillation elements arranged azimuthally as shown in Fig. 3.7. It was located directly downstream from C1 and was designed such that the outer edges of two adjacent scintillation paddles just matched the azimuthal boundaries of each cell in C1. Inside the 24 TOF counters were four more scintillation counters called quad counters. The quad counters were not connected to TDC's because most particles striking them were travelling too fast for the resolution of the electronics and thus could not provide a useful mass measurement. However, discriminated signals from all 28 counters were logically OR'd and then used as a part of several of the triggers.

Dipole Spectrometer

The function of the dipole spectrometer was to make an accurate momentum measurement of relatively high momenta particles which had been only poorly measured in the solenoid. The dipole spectrometer consisted of a 16 kilogauss dipole magnet, a proportional wire hodoscope, four magnetostrictive spark chambers, two scintillation hodoscopes, and a threshold Cherenkov counter.



The dipole magnet had a 1 meter gap and a field region of 2.4 meters in the beam direction and 2 meters wide. The field integral was 39 kg-m. The proportional hodoscope consisted of a single plane of vertical wires and provided in-time information for downstream track finding.

The four magnetostrictive spark chambers were all identical, each providing X, Y, E, and P coordinates (E, P: $\pm 30^\circ$ to vertical) and having a wire spacing of 28 wires/inch.

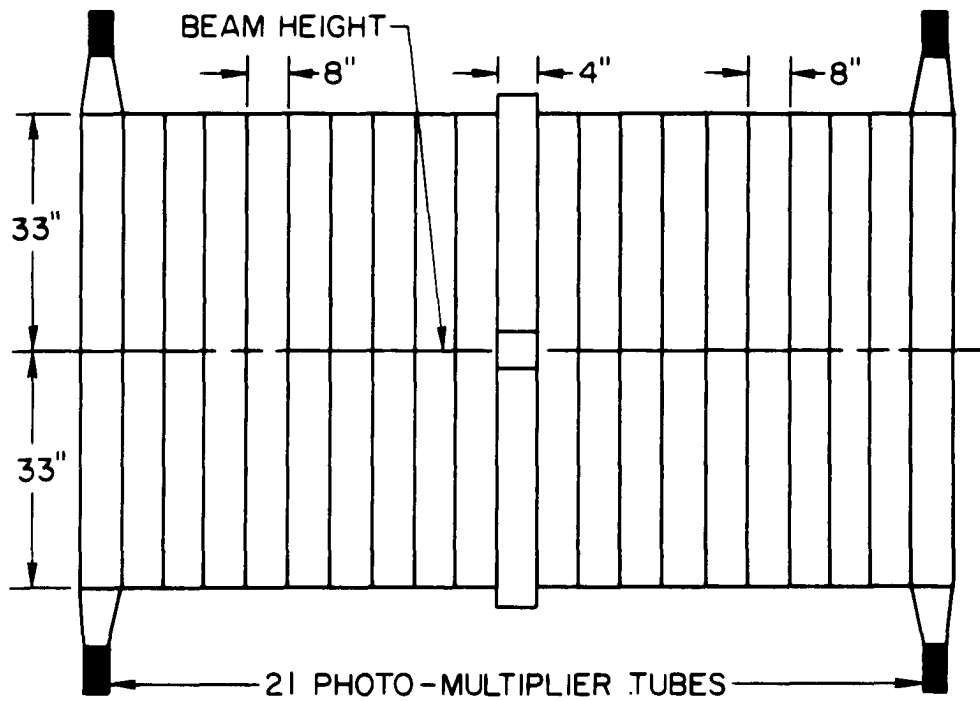
The scintillation hodoscopes consisted of individual counters placed next to one another in the form of a picket fence. Each counter had two such picket fences, one above the beamline and one below the beamline. These counters also had in-time information and were used in several of the triggers to ensure that at least one particle had made it through the dipole.

The Cherenkov counter, C2, consisted of eight mirrors, each reflecting light to a separate phototube. The phototubes were fitted with bucking coils and shielded from the fringe fields of the dipole and solenoid magnets. The counter was filled with Freon-12 at one atmosphere pressure. This produced a pion threshold of 3.0 GeV/c and a kaon threshold of 10.6 GeV/c and a proton threshold of 20.2 GeV/c. The results of a study made of the efficiency of C2 are contained in the Appendix.

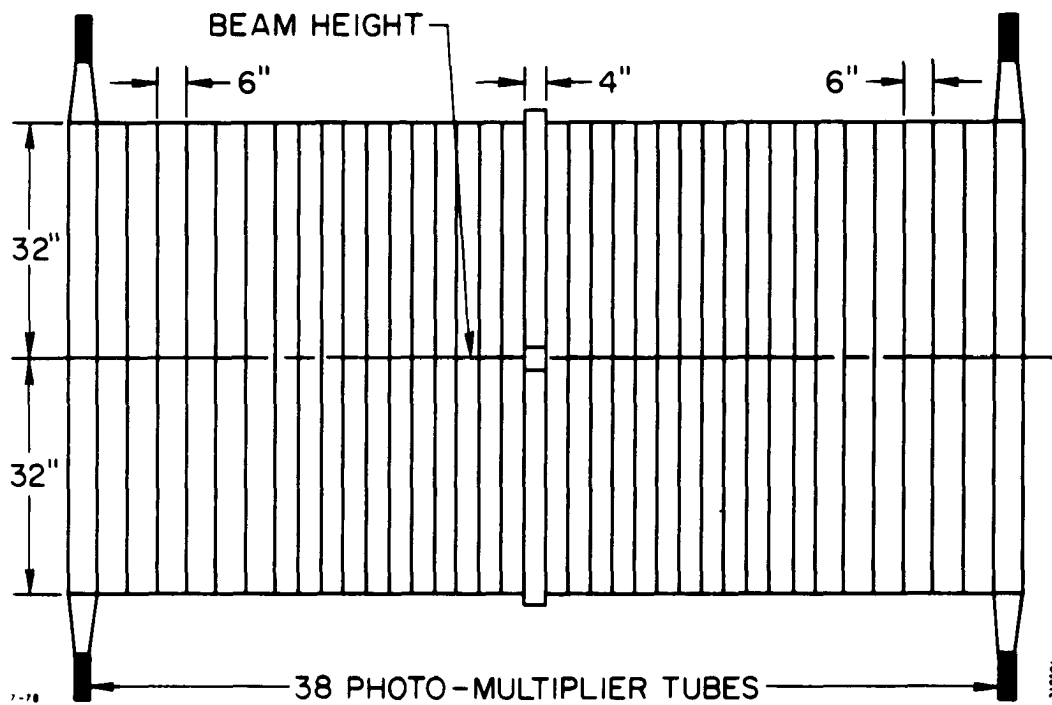
Figure 3.8. Scintillation hodoscopes

(a) HA.

(b) HB.



(a)



(b)

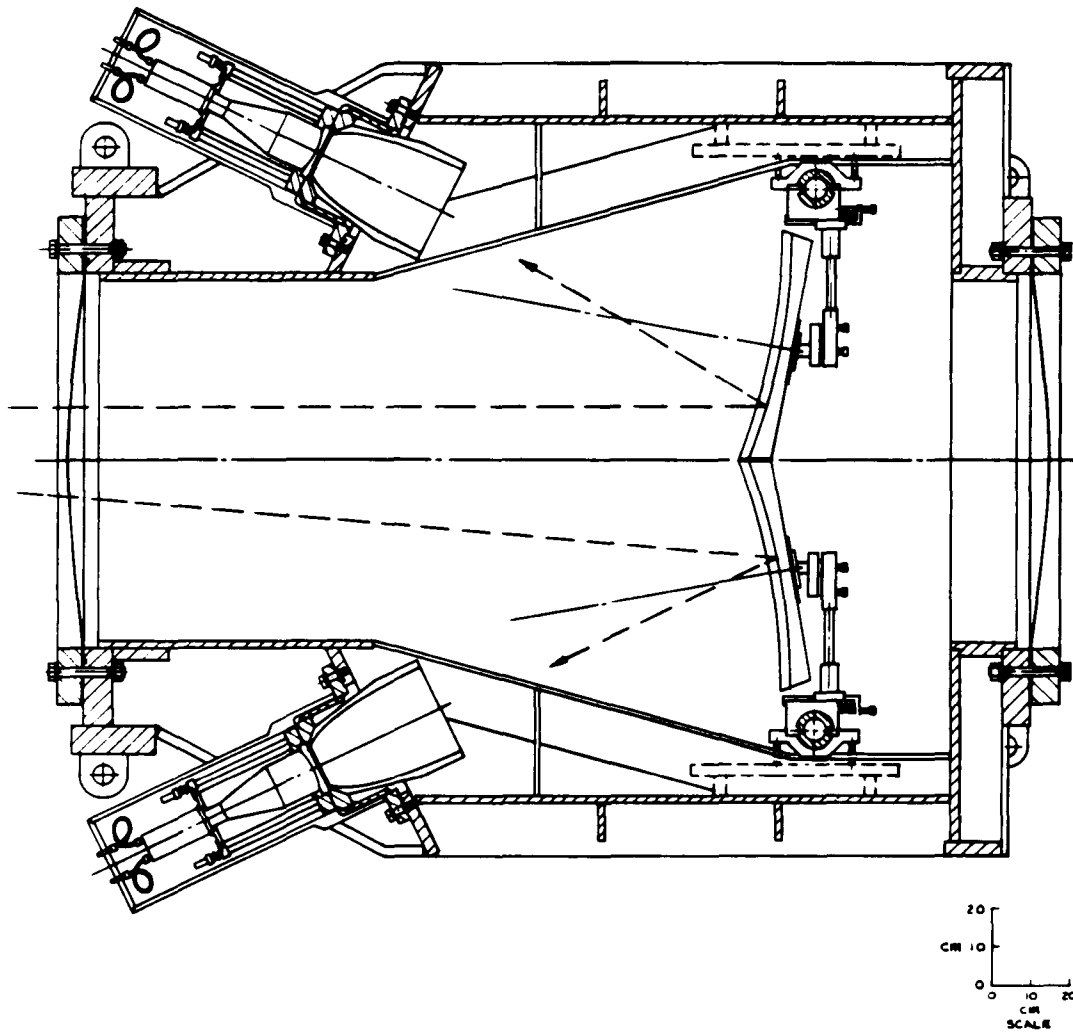


Figure 3.9. Side view of Cherenkov counter C2

Data Readout

C-D spark chambers (cylindrical and planar)

Capacitive-diode discriminators were attached to each wire. The output of each discriminator was stored in a shift register and the contents of the shift register were later strobed into the data acquisition system.

Proportional wire chambers

Each wire was connected to an amplifier-discriminator circuit. The discriminator output was strobed at a rate of 49 MHz and stored in a 32 bit Random Access Memory (RAM). The contents of the RAM were then fed into the data acquisition system. The purpose of recording a 32 bit time profile of each wire was to allow the timing to be done in the software rather than in the hardware.

Magnetostrictive chambers

The arrival times of signals generated by both fiducials and spark wires were measured, digitized and sent on to the data acquisition system.

Cherenkov counters C1 and C2

The dynode signal from each phototube in C1 was amplified and fed into an Analog-to-Digital Converter (ADC). The anode signal, after being discriminated, was stored in an event gated latch called a "buffer strobe module." Buffer strobe and ADC signals were also read out from C2.

Scintillation counters (beam counters, TOF, HA, HB, LP3)

All the scintillation counters used conventional phototubes. Output signals from the phototubes were discriminated and then sent on to ADC and TDC modules which provided pulse height and timing information.

CHAPTER 4. TRIGGERING AND DATA ACQUISITION

The major physics interest of this experiment was the examination of several particle reactions which occur very rarely as compared to other reactions. Typically, this experiment looked for events with a fast forward particle heavier than a pion, associated with another lower momentum particle to the side. In order to avoid excessive amounts of data irrelevant to this experiment, it was necessary to select events which appeared to be of interest and send only these events to the data acquisition system. This was accomplished by the fast logic system. The fast logic system examined the outputs of various chambers in the system, performed logical functions on these outputs, and finally decided whether or not to trigger the system and record the data for that event. The following is a description of the fast logic system and the data collection system. For more information see References 37-42.

Beam Logic

The beam logic identified incoming beam particles. The timing for the beam logic was determined by a 10 cm square scintillation counter SE ("START EVENT"), which provided a very narrow output signal (~ 7 ns). Discriminated signals from each quadrant of the X-Y counter were logically OR'd to produce a logical $\Sigma XY \geq 1$ signal with a 32 ns duration. The BEAM PARTICLE signal was then determined by a coincidence between the SE signal and the $\Sigma XY \geq 1$ signal. Events with more than one beam particle appearing within the resolving time of the apparatus were

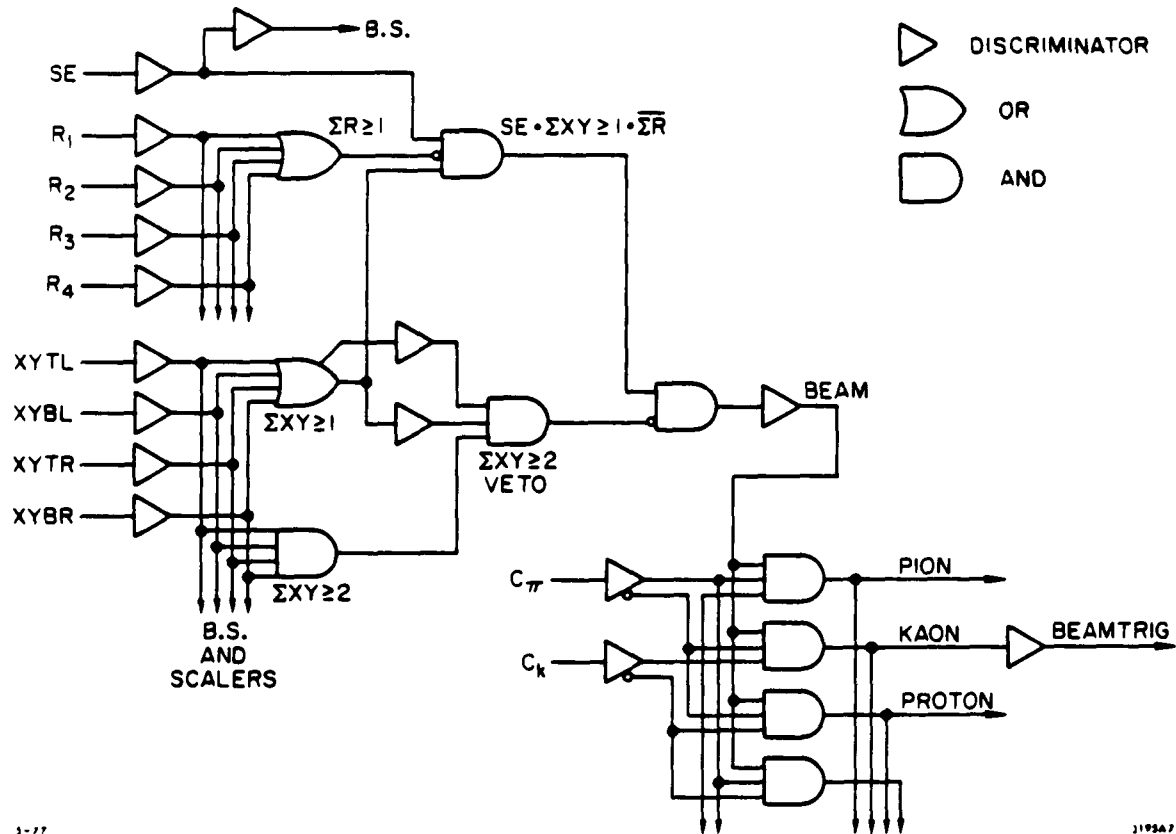


Figure 4.1. Beam logic

excluded by the AND of the BEAM PARTICLE signal with two veto signals $\overline{\Sigma XY \geq 2}$ and $\overline{\Sigma R \geq 1}$ where R represents the ring counter. It was necessary to include the veto signal from the ring counter in order to exclude particles in the beam halo which interact in the target walls. The definition for BEAM was then $SE \cdot \Sigma XY \geq 1 \cdot \overline{\Sigma XY \geq 2} \cdot \overline{\Sigma R \geq 1}$.

Information from the two beam Cherenkov counters was used to identify the beam particles. The logical signal for a pion beam particle was defined as $BT = BEAM \cdot CK \cdot C\pi$.

Trigger Logic

Output signals from various detectors in the spectrometer were converted to logical signals and combined with the beam logic to form the trigger logic. The purpose of the trigger logic was to select events of interest and then trigger the system to record the data for that event. The experimenters determined what state the various detectors should be in when an event of interest occurred and then logically combined the output to determine whether or not to fire the chambers. The use of Trigger-Rate-Equalizers (TRE's) allowed several different triggers to be established simultaneously. In this way, events of different characteristics could be recorded during a single run. The proportion of each type of trigger could also be selected. This experiment used five different trigger types.

The primary physics trigger (T0) was designed to select events rich in strange particles. The logic for the T0 trigger was as follows:

$$T0 = BT \cdot TOF \geq 2 \cdot (P1.5 > 1 + CYL > 1) \cdot HA \geq 1 \cdot HB \geq 1 \cdot JHD \geq 1 \cdot \overline{CL}.$$

Here P1.5 stands for the full bore proportional chamber 1.5 and CYL represents the cylindrical proportional chamber. The locations of the various elements are shown in Fig. 3.1. The $\text{TOF} \geq 2$ requirement vetoed elastic events. The requirement $(\text{P1.5} > 1 + \text{CYL} > 1)$ ensured that the reaction took place in the target. In order for a particle to pass through the dipole magnet, its momentum had to be above the pion threshold in Cherenkov counter C1. By requiring that there be no light in C1, the mass of this particle must be greater than the pion mass. This eliminated the large pion background and produced a sample of events enriched in kaons.

The T1 trigger was a general interaction trigger and was defined as

$$\text{T1} = \text{BT} \cdot \text{TOF} \geq 2 \cdot \overline{\text{LP3}} \quad .$$

The elastic trigger (T2) was defined as

$$\begin{aligned} \text{T2} &= \text{BT} \cdot \text{HA} \geq 1 \cdot \text{HB} \geq 1 \cdot \text{TOF} \geq 2 \cdot (\text{HA} \geq 2 + \text{HB} \geq 2) \\ &= \text{BT} \cdot \text{HA} = 1 \cdot \text{HB} = 1 \cdot \text{TOF} \leq 1 \quad . \end{aligned}$$

This trigger cut out events of low- t because particles traveling dead ahead passed through holes cut in HA, HB, and the TOF counters to allow the beam to pass through. The elastic events were used to study track finding and to check the calibration of the beam momentum. The T3 trigger was a beam trigger used to measure the phase space and determine alignment constants and was defined as $\text{T3} = \text{BT} \cdot \text{LP3}$. The final trigger (T4) was very similar to the T0 trigger and, in fact, most events satisfying the T0 trigger also satisfied the T4 trigger. However, the absence of the C1 veto logic in the T4 trigger allowed other interesting

final states (i.e., $k\pi$) to be studied. The T4 trigger was defined as

$$T4 = BT \cdot HA \geq 1 \cdot HB \geq 1 \cdot \overline{C2} \quad .$$

A typical run contained the following percentages of each type of trigger:

$$T0 = 44$$

$$T1 = 5$$

$$T2 = 7$$

$$T3 = 5$$

$$T4 = 60 \quad .$$

Gating Logic

The coincidence of a signal from the trigger logic and a signal from the gating logic caused the high voltage to be applied to the spark chambers, and the data to be readout and stored. The gating logic was necessary because of system dead time. There were three types of gates provided at the LASS spectrometer and various scalers operated from each of them. All three gates were started by a B2NU signal from the SLAC accelerator which preceded the arrival of the beam spill by exactly 2.5 μ sec. The gates were turned off at the end of the beam spill which lasted 1.6 μ sec. The gate logic is shown in Fig. 4.2.

The most important gate was the event gate. Besides the B2NU signal, the conditions necessary to start the event gate were as follows. First, the C.P.OK signal had to be turned on by the experimenters which indicated the beginning of a data taking run. Second, the 20 msec dead time of the spark chambers must have elapsed in order to clear the

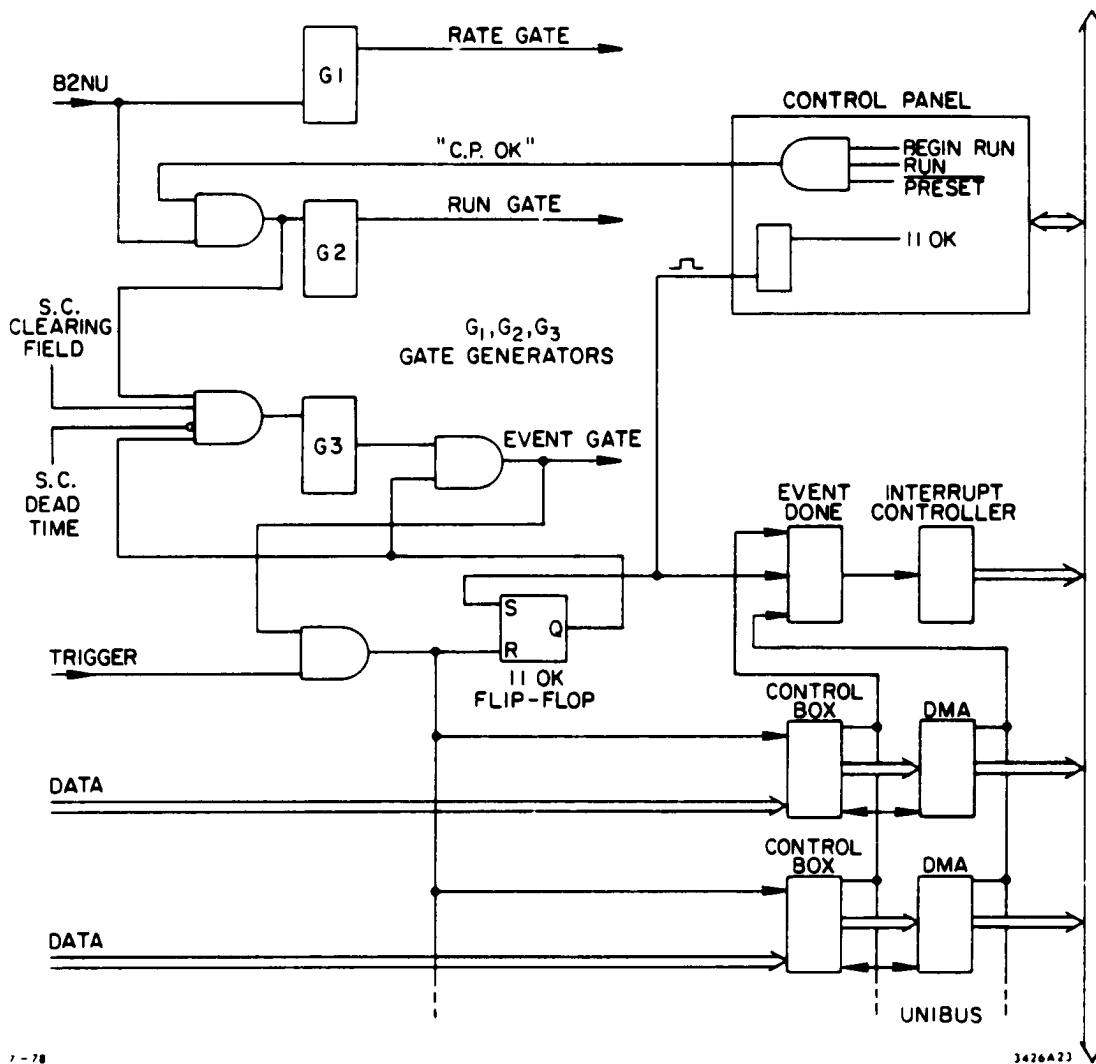


Figure 4.2. Gate logic

spark chambers of the ions from the previous event. Finally, the 11 OK flip-flop must be turned on by the PDP-11 which indicated its buffers were cleared and it was ready to accept data from a new event. The occurrence of a trigger signal in coincidence with the event gate caused the spark chambers to be fired and the data to be readout and stored. The presence of a trigger signal also immediately turned off the event gate so that the scalers operating from it would not count during the data collection and the subsequent dead time. Scalers associated with the event gate were used in the normalization for this experiment.

The other two types of gates were rate gates and run gates. The rate gate simply started with the B2NU signal and stopped at the end of the 1.6 μ sec beam spill. The run gate was similar to the rate gate except that it required a coincidence between the B2NU signal and the C.P.OK signal. Scalers associated with these gates were used in beam steering and centering. The run gated scalers allowed the observation of various quantities without actually recording the data. The run gated scalers in conjunction with the event gated scalers also provided a measurement of the overall dead time of the system.

Data Acquisition and Storage

The data were readout as described in the previous section. The data were then transferred via direct memory access (DMA) modules to a PDP-11 where it was organized and then sent to either the SLAC Triplex computer or an IBM 1800 where it was written onto magnetic tape. A diagram of the acquisition system is shown in Fig. 4.3.

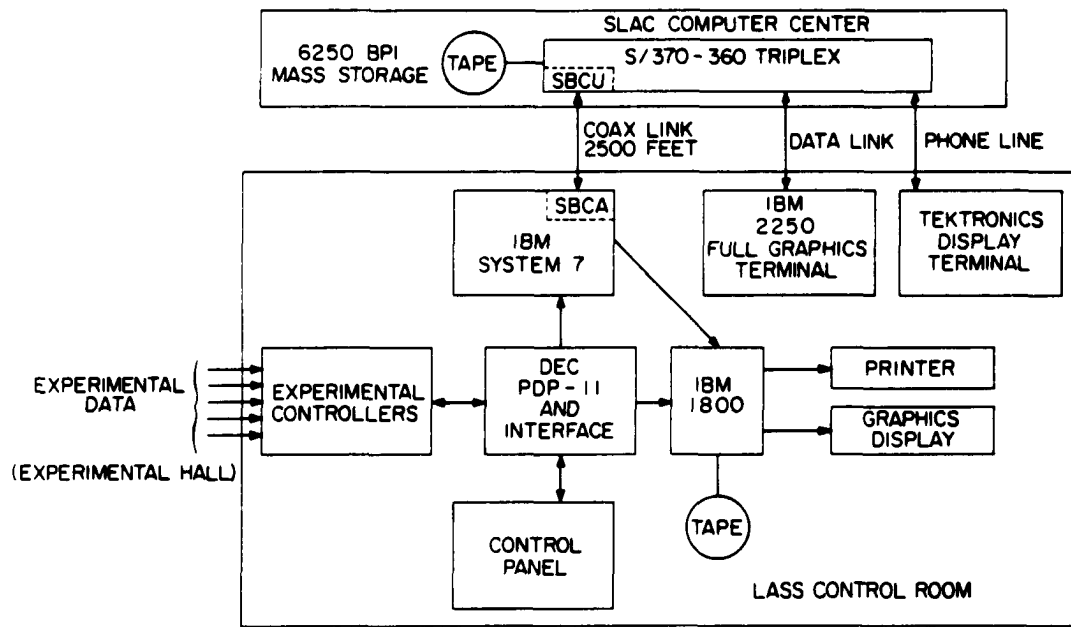


Figure 4.3. Data acquisition system

The Triplex computer was located in the SLAC Computation Center and consisted of 2 IBM model 370/168's and one IBM model 360/91. The Triplex was the primary system used and offered the experimenter a real-time network to monitor the on-going experiment. The real-time network contained an analysis task which was capable of analyzing a sample of events through the entire event reconstruction program. An IBM 2250 graphics terminal coupled to the sophisticated analysis task allowed the experimenter to closely monitor the operation of the spectrometer.

The 1800 was located in the LASS control room and acted as a backup when the Triplex emulated a good-woman silence. Only a very simple monitoring program was available when using the 1800.

CHAPTER 5. EVENT RECONSTRUCTION

A series of computer programs operated on the data to try to reconstruct the events. A typical event satisfying the $T\phi$ trigger is shown in Fig. 5.1. Wire numbers where sparks occurred in the various chambers were first converted to spatial coordinates by using chamber positions determined from the alignment procedure (described later in this chapter). The spark coordinates were then used to reconstruct tracks. Track reconstruction procedures differed for the beam region, the solenoid region, and the downstream region.

Since there was essentially no magnetic field in the beam region, tracks found in this region were parameterized by the five quantities x_0 , y_0 , z_0 , dx/dz , dy/dz which defined a straight line as given by

$$\begin{aligned} X &= X_0 + (Z - Z_0)dx/dz \\ Y &= Y_0 + (Z - Z_0)dy/dz \end{aligned} .$$

The coordinate system used here and in all reconstruction programs was the same as defined in Chapter 3. The origin was chosen to be on the solenoid axis just upstream from the target.

The magnetic field in the solenoid was very uniform and thus tracks in this region were fit to a helix as determined by

$$\begin{aligned} X &= X_0 + R \cos(\phi_0 + (Z - Z_0)d\phi/dZ) \\ Y &= Y_0 + R \sin(\phi_0 + (Z - Z_0)d\phi/dZ) \end{aligned} .$$

The fitting routines determined the parameters X_0 , Y_0 , ϕ_0 , R , and $d\phi/dZ$ for a particular Z_0 . The solenoid track finding algorithms were based

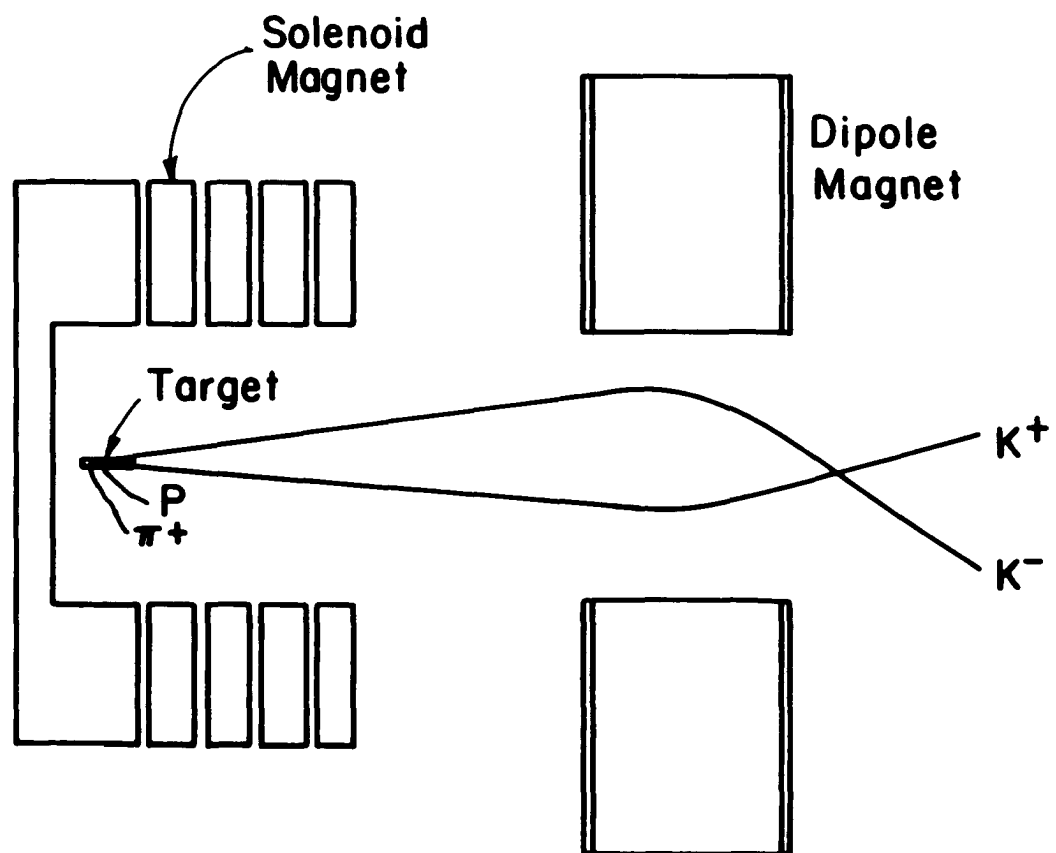


Figure 5.1. Typical event satisfying the T0 trigger

on the fact that a helix appears as a circle in the X-Y plane and also that $d\phi/dZ$ is a constant for a helix. Tracks found in the solenoid were extrapolated into the twixt region and Cherenkov (C1) and TOF information were assigned to each track. Spark coordinates downstream of the dipole were fit to straight lines. The downstream tracks were then extrapolated back through the dipole into the twixt region where another straight line fit to coordinates was attempted. If a twixt extension was found for the dipole track, then the track was extrapolated back into the solenoid and the iterative tube procedure was used to fit the track to a helix.

After reconstructing all of the tracks for a particular event, the track parameters were used to find both primary and secondary vertices. The tracks associated with a particular vertex were then refit to provide the best track parameters consistent with that vertex. Finally, a kinematic fit was attempted for each vertex. The following describes the above in somewhat more detail.

Solenoid Track Finding

A cluster was formed if a group of adjacent wires fired. The coordinate at the center of the cluster was then used in the track finding rather than the individual wire coordinates. Solenoid tracking was initiated by combining points from each plane of a chamber to form a match point. The proportional chambers had three planes - X, Y, and E. The X and Y planes were combined first and then corroboration was asked from the E-plane. Two plane match points were also accepted because of inefficiencies in the chambers. The C-D spark chambers had

four planes and, therefore, three or four plane match points were set up for them. Match points in the cylinders were set up between the left and right pitched wires. The cylinder match points thus provided ϕ and Z information at a particular radius.

Two procedures were used for combining these match points to form solenoid tracks. The two procedures differed only in which chambers initiated the track finding. In the end, information from all chambers was considered in both procedures. One algorithm started with the plane chambers. Match points from the plane chambers were used to define a helix. The helix was then projected onto the X-Y plane where it should appear as a circle and was tested for its circularity. $d\phi/dZ$ for the helix was also checked and should have been constant. If it passed these tests, corroborating points were looked for in the other chambers within a 5σ tube placed around the helix. A new helix was computed using all of the points found. A second iteration helix was then computed using points from a 3.5σ tube. Coordinates from chambers with too many missing points were then thrown out and a final fit to the helix was made using the remaining points. The track was finally accepted if its confidence level was greater than 1%.

The other algorithm for finding solenoid tracks started with the cylinder chambers. The bending angle between match points in three cylinder chambers was required to be smooth. If it passed this test, the same iterative procedure to find the track parameters was applied as had been used for the plane chamber algorithm.

Tracks found by both procedures were then extrapolated into the twixt region provided that their momentum was >750 MeV/c and that they didn't strike the solenoid wall. Time-of-flight and Cherenkov (C1) information were then assigned to each track.

Beam and Dipole Track Fitting

Beam and dipole track finding algorithms were similar in that they fit the coordinates to straight lines using an iterative tube procedure. Beam track candidates were formed by taking all combinations of one match point from each of the beam PWC's. Straight line parameters were then calculated from each combination of two match points and a tube of radius R was placed around the fit. Points within the tube were then included in a new least-squares fit and the resulting parameters compared with the old parameters. If the parameters disagreed, a new tube was placed around the line, bad points discarded, and a new fit made. This iterative process continued until either the parameters from one iteration to the next agreed or there were less than seven points left in which case that track candidate was discarded. In addition, the beam track candidate could share only a certain maximum number of points with any beam tracks already found. The track candidate was then extrapolated into the θ - ϕ hodoscope and the X-Y scintillation counter and at least one of these counters was required to fire. Finally, the track was saved if only one bin in the P-hodoscope was hit.

Dipole track finding started by finding coordinates from three planes of a given type that formed a straight line. These were called X, Y, E, and P views depending upon which type of coordinate plane was

being looked at. Tracks were then started by comparing intercepts from different views. If the intercepts agreed, a tube was fitted to the track and all points within the tube were used to compute the new track. The tube size was decreased, new points chosen and the track refit until two iterations agreed. The downstream track was then crossed through the dipole using a map of the dipole field. If the track did not strike the dipole, the twixt chambers were looked at for corroboration. Once an X-coordinate was found, the track was extrapolated into the twixt chambers establishing a trial road. A tube was set up around the trial road and corroborating sparks were looked for in the chambers. The tube diameter was decreased and the track was refit using the new set of points. The iterations stopped when two successive iterations agreed on the number of points in the tube. A maximum of five iterations were allowed. At this point, the chi-square was calculated and if less than a certain value, the track was considered good.

The dipole track and its twixt extension determined the momentum of the track. In order to determine the vertex position for the interaction, the track's coordinates at the target must be known. Therefore, the twixt extension of the dipole track was extrapolated into the solenoid region. The track was swum through the highly nonuniform fringe field of the solenoid by Runge-Kutta procedure using a field map of the fringe field. Once inside the solenoid, the field was very uniform and a least squares fit to a helix was made using the iterative tube procedure. The track coordinates were thus determined by the parameters to the fit helix.

Vertex Finding and Fitting

Once all of the tracks had been found, the next step was to determine the origin of the interaction. The vertex finding program, VRHUNT, was quite versatile in that it found primary vertices of varying topologies and also secondary vertices resulting from the decay of neutral particles (i.e., K^0 , Λ^0). It also rejected spurious tracks found by the track finding algorithms. The spark chambers used throughout the spectrometer had long memory times and thus contributed many out-of-time coordinates. In order to eliminate these out-of-time tracks, the track finding program required each track to have a certain minimum number of in-time coordinates. This greatly reduced the number of out-of-time tracks inputted to VRHUNT. However, the presence of the out-of-time sparks from the spark chambers together with the noise and background from all of the chambers produced tracks which were not associated with the primary interaction. Since these spurious tracks were not associated with the primary interaction, they generally pointed in some direction other than the point of interaction. Their distance of closest approach to the vertex was then very large. VRHUNT would throw these tracks away because it found the "best" vertex by eliminating the tracks that contributed the largest chi-square.

VRHUNT "finds" the vertex for a given set of tracks by minimizing the quantity

$$D^2 = \sum_{i,j} (x_v^j - x_i^j)$$

where (x_i^1, x_i^2, x_i^3) is the calculated point of closest approach for each

track i to the vertex (X_v^1, X_v^2, X_v^3) . These points of closest approach X_i^j are functions of X_v^1 and cannot be determined exactly because of the complex transcendental nature of the solution. They are calculated in the following iterative manner. As shown in Fig. 5.2a, the actual point of closest approach is a distance s_i from the point X_i^j and the line along the distance of closest approach is perpendicular to the tangent at the point of closest approach. The helix is then approximated by a straight line, Fig. 5.2b, and the normalcy condition requires

$$(X_i^j + s_i \epsilon_i^j - X_v^j) \cdot \epsilon_i^j = 0$$

which determines

$$s_i = \epsilon_i^j (X_v^j - X_i^j)$$

where ϵ_i^j are the direction cosines for the tangent at X_i^j . After each iteration, a new point of closest approach is calculated as follows

$$X_i^3(\text{New}) = X_i^3(\text{Old}) + \epsilon_i^3 s_i.$$

The new X_i^1 and X_i^2 are calculated on the helix at $Z = X_i^3(\text{New})$. The minimization conditions now take the form

$$\frac{\partial D^2}{\partial X_v^k} = \sum_{i,j} (X_i^j + s_i \epsilon_i^j - X_v^j) (\epsilon_i^j \epsilon_i^k - \delta^{jk}) = 0$$

which can be written in the form

$$A_{kj} X_v^j = a_k \quad (6.1)$$

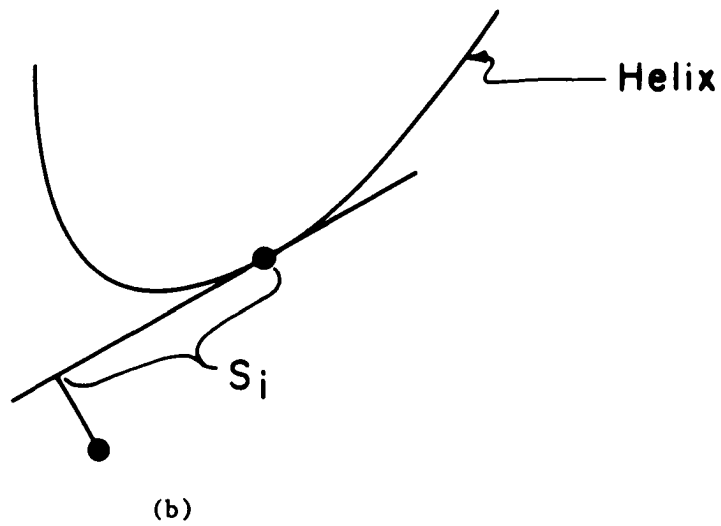
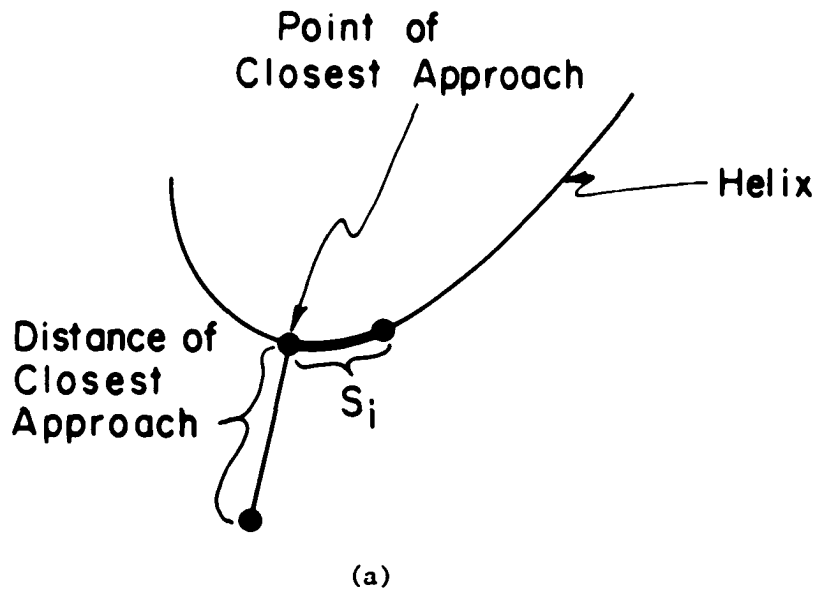


Figure 5.2. Determination of point of closest approach of helix to vertex

- (a) Actual point of closest approach on helix
- (b) Straight line approximation to helix

where

$$A_{kj} = \sum_i (\epsilon_i^j \epsilon_i^k - \delta^{jk})$$

and

$$a_k = \sum_{ij} [\epsilon_i^k (X_i^j \epsilon_i^j) - X_i^k] \quad .$$

The vertex X_v^j is found from Eq. (6.1) by the matrix inversion technique.

VRHUNT began by trying to make a primary vertex using all of the tracks. The fit was called excellent, good, or OK depending upon the value of the chi-square per degree of freedom. If the vertex was called excellent (very small chi-square/degree of freedom), this vertex was declared to be the correct vertex; the parameters for it were saved and the vertex finding stopped at this point. However, if the vertex was declared either good or OK, then the vertex finding continued in the following manner. First, a fit was attempted using a primary vertex consisting of N-2 tracks (N = total number of tracks found) and a secondary vertex (presumably from the decay of a neutral particle) consisting of the two tracks excluded from the primary vertex. The two tracks contributing the largest chi square to the original N-prong vertex were the first two tracks tried in the secondary vertex but in the end all combinations of pairs of tracks were examined as a possible secondary vertex. If no excellent vertex was found using all of the tracks, then one of the tracks was thrown out and a search was made for an N-1 prong primary vertex. Again, if no excellent vertex was found, an N-3 prong primary vertex plus a secondary vertex was tried. The

vertex hunting continued in this manner and allowed a maximum of three tracks to be excluded from a fit consisting of only a primary vertex and a maximum of two tracks to be thrown out from fits consisting of both a primary and a secondary vertex. In the end, the best fit to the primary only vertex was saved along with the three best fits to (primary + secondary) vertex.

In finding these vertices, VRHUNT used the track parameters calculated in the track finding programs. The purpose of VRHUNT was to determine which tracks should be included in the vertex. Once VRHUNT had established the topology of the vertex, it was then necessary to make a geometry fit to the vertex; in other words, to refit the tracks and vertex constraining the tracks to the vertex. This was accomplished by a program called MVFIT. The track coordinates and parameters along with the VRHUNT vertex parameters were input to MVFIT as the starting values for the constrained fit. The beam track parameters and error matrix were also used in the fit which was based on an iterative Lagrange multiplier technique. The fit also included corrections for energy loss in the target and for multiple scattering. Thus, the geometric fit gave the best values for the track parameters and it was these values that were used in all of the subsequent analysis.

Finally, the results of the geometry fit were used as starting values for a kinematically constrained fit. Although these fits were made, they were not used in the present analysis.

Alignment

An optical survey measuring the position of the various chambers in the spectrometer was conducted after the data for this experiment was taken. These measurements served as a first order approximation in aligning the system. The alignment constants were refined by using three sets of data taken during the experiment. Two of these sets of data were taken with no magnetic fields on. The third data set, from which the final alignment constants were determined, was a sample of TO triggered events from the actual production run which involved both solenoid and dipole magnetic fields on.

The alignment procedure for all three data samples was essentially the same and involved the calculation of residuals which were defined as:

$$\text{residual} = (\text{measured coordinate}) - (\text{expected coordinate from fit}).$$

Straight line least square fits, using the iterative tube procedure described earlier, were made to tracks in the first two data samples since there were no magnetic fields present. The first data sample came from the T3 trigger and was just straight-through beam tracks. Hundreds of events of this type were processed and the alignment error for each plane was then just the mean of the residual distribution for that plane. The offset constant for each plane was then corrected by this alignment error and the coordinates recalculated using the new offset constants. The entire alignment procedure was then repeated using the new coordinates and calculating new residuals until consistent alignment constants were obtained. All of the plane chambers in the spectrometer were aligned using this beam straight-through data sample except the

spark chambers in the twixt (MS1T, MS2T) and solenoid (CD1-CD4) regions. These spark chambers had their central areas desensitized to allow the beam to pass through undetected. The spark chambers in the dipole region (MSD1-MSD4) also had desensitized beam areas but with the dipole field off the beam passed through sensitive areas of these chambers.

The twixt and solenoid spark chambers were aligned using the second field off data sample which included large angle tracks. The alignment procedure was identical to that for the first data sample except that only those chambers already aligned by the beam straight-through process were included in the straight line fits. Residuals for the unaligned spark chambers were then calculated and the offset constants corrected.

Thus, the first two data samples aligned all of the chambers of the spectrometer except the cylinder chambers and the scintillation counters. These detectors were aligned using the final data sample which contained events satisfying the TO trigger. The cylinder chambers were aligned in a two step process. First, the cylinder chambers were aligned with respect to one another and then the entire cylinder package was aligned with respect to the rest of the spectrometer. The internal alignment of the cylinder package was accomplished using large angle tracks that passed primarily through the cylinder chambers. Since the solenoid magnetic field was on, these tracks were fit to helices. The residuals were then calculated and the offset constants corrected. Once the cylinders were aligned with respect to one another, another subsample of tracks was selected from the TO data in order to align the cylinder package with the rest of the world. This subsample contained

large angle tracks that passed through both the cylinder chambers and the plane chambers. Helical fits were made to the data using only the plane chambers. The resulting track was then extrapolated back through the cylinder chambers where the residuals were calculated. Finally, the cylinder parameters were changed allowing the cylinder package to rotate and tilt in order to minimize the residuals.

The scintillation counters were aligned by extrapolating tracks to the counter. A plot was then made of the X-Y position of those tracks producing light in the scintillation counter and the edges of the counters were easily identified and the relevant corrections made to the counter positions.

Finally, all the chambers in the spectrometer were realigned using this TO field on data. These final parameters differed only very slightly from the field off parameters.

CHAPTER 6. DATA ANALYSIS AND MONTE CARLO

The sequence of the analysis steps is shown in Fig. 6.1. There were three stages in the data analysis. First, the trackfinding was done by the LASS production job. Then the VRHUNT and MVFIT packages examined the tracks to find vertices. Finally, the DST maker produced Data Summary Tapes (DST's) of both the geometrically fit and the kinematically fit events. Various cuts were imposed on the data during the analysis procedure. The effect each cut had on the physics associated with the data must be understood, and to this end a Monte Carlo simulation of the data was produced. A brief outline of the Monte Carlo's operation will be given and the various cuts on the data will be interpreted in terms of the Monte Carlo.

LASS Production Job

This was the first stage in the data analysis. The 197 6250 BPI tapes (corresponding to ~ 11 million events) were processed in this stage. Only a portion of these events, however, were fully processed. There were a number of early selection criteria imposed on the data in order to select only those events of interest and thereby reduce the amount of computer time needed to analyze the data. These cuts and their effects on the data are summarized in Table 6.1.

Since the T0 trigger was the primary physics trigger, the first cut selected only those events satisfying the T0 trigger. Portions of the data from the other triggers were analyzed separately. This experiment

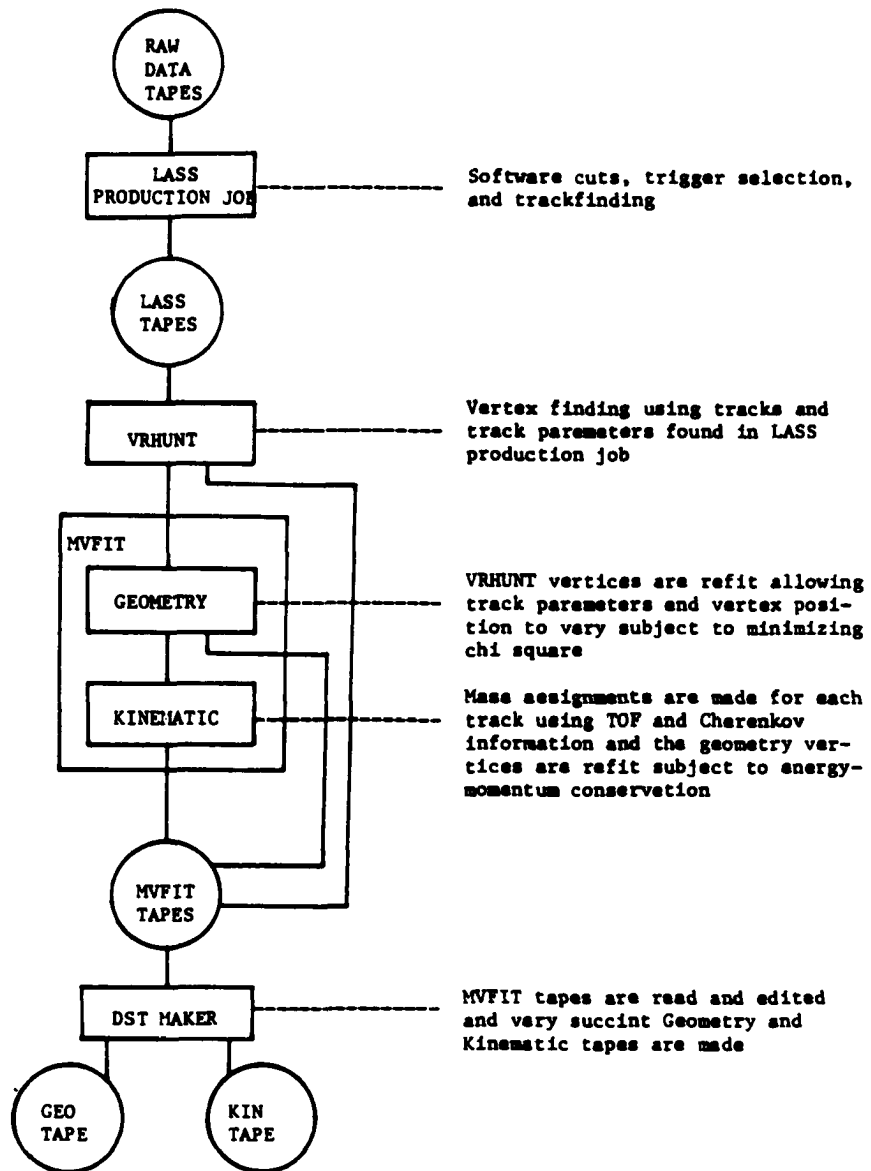


Figure 6.1. Data processing flow diagram

Table 6.1. Software T0 production cuts

Cuts imposed on data	Sequential percentage losses
T0 trigger	53%
Clean	7%
Dipole track	15%
Dipole track with twixt extension	28%
Dipole track with momentum > 3.0 GeV/c	36%
C2 (no light)	30%
Track through efficient part of C1 or through C2	15%

was only concerned with events of low multiplicity (≤ 6). The "clean" cut, which allowed a certain maximum number of hits in the solenoid chambers was employed to exterminate those events not mindful of the over population problem. It also eliminated those events having an intolerable amount of noise. The "clean" cut occurred early in the analysis (before most of the data was even unpacked) and therefore saved considerable time.

The second requirement was that the event have a downstream track that was continued into the twixt region. The T0 trigger was designed to select events with at least one downstream track; however, slow particles interacting with the dipole walls could produce interaction particles that would satisfy the trigger. The requirement that the dipole track have a twixt extension eliminated these events. The downstream track finding was done before the solenoid trackfinding. If a downstream track with a twixt extension was not found, then the time consuming solenoid trackfinding was eliminated. Also the downstream track finding was much faster than the solenoid track finding since there were fewer sparks in the downstream region and the track finding algorithms were much simpler.

The third requirement was that there be at least one downstream track with a momentum greater than 3.0 GeV/c. The Monte Carlo indicated that tracks originating in the target did not make it through the dipole if their momentum was less than 3.0 GeV/c. This cut then eliminated spurious triggers resulting from secondary interactions downstream of the target.

The fourth requirement was that there be no light in Cherenkov counter C2. The threshold was such that protons and kaons would not make light in it but any pion fast enough to make it through the dipole (momentum $> 3.0 \text{ GeV}/c$) should make light in it. Recall that the fast logic for the T0 trigger did not allow any light in Cherenkov counter C1. C2 was not made a part of the fast logic trigger so that it could provide a measure of the inefficiency of C1. It was found in a subsequent study (contained in the Appendix) that some regions of C1 were very inefficient, in particular the cells in the A ring and the two D cells. In order to minimize the reliance on these inefficient areas, a fifth cut was applied to the data. This cut required that at least one track either go through an efficient area of C1 (i.e., through a cell in either the B or the C ring) or go through C2.

If an event survived all of these cuts, the solenoid track finding was then invoked. After having found all of the tracks associated with the event, an output record was made. The output record was written onto magnetic tape and consisted of the track parameters along with all of the raw data for that event. These output tapes consisted of a reduced sample of events (only those events satisfying the cuts) and contained all of the information necessary to rerun the track finding programs if need be. The original 197 raw data tapes were now reduced to 33 LASS output tapes. These output tapes became the input tapes for the next stage in the data processing--the vertex finding.

Vertex Finding and Fitting

This stage of the analysis consisted of finding the vertex and refitting the event by employing the previously described analysis programs VRHUNT and MVFIT. VRHUNT used the track parameters and data as found on the LASS output tapes to determine the vertex for each event. If VRHUNT was successful in finding a vertex (65% of the events input to VRHUNT made fits) then MVFIT was used to refit the event constraining the tracks to emerge from the vertex. The track parameters as determined in the LASS production job and the vertex position determined in VRHUNT were used as starting values. If the geometry fit converged (83% of the VRHUNT events made Geometry fits) then a kinematically constrained fit was attempted.

The results from each stage of this process (VRHUNT, GEOMETRY, KINEMATIC) were written onto a common output tape (MVFIT TAPE). It was therefore easy to compare the results the different fitting routines produced for each event. The MVFIT tapes contained enough information so that any of the three routines VRHUNT, GEOMETRY, KINEMATIC could be rerun without having to redo the others. There were 18 MVFIT tapes which represented about 686,000 events. It would have been very cumbersome and time consuming to try to make plots and histograms of physics quantities from all 18 of these tapes. Therefore, it was necessary to edit the data which is what the third stage of the data processing did.

DST Maker

The DST maker simply read the 18 MVFIT tapes and then made an output tape for the geometrically fit events (GEOMETRY TAPE) and an output tape (KINEMATIC TAPE) for the kinematically fit events. These output tapes contained only enough information from each event to examine the physics quantities of interest (i.e., vertex position, particle identification, and momentum vectors for each track). The 18 MVFIT tapes were condensed in this manner into a single GEOMETRY tape and a single KINEMATIC tape. Finally, tapes containing subsamples of the events on these tapes were made; for instance, a tape containing only three prong geometrically fit events was made. It was these tapes containing only specific subsamples of the data that were used in the final physics analysis because they greatly reduced the CPU time needed to do the analysis by eliminating the time consuming reading and unpacking of events not pertinent to the physics topic being investigated. For instance, the tape used in the analysis of the reaction $\pi^+ n \rightarrow K^+ K^- p$ contained only three prong events which had two kaons each with a momentum greater than 3.5 GeV/c. A typical histogramming job using this tape took only about two minutes as opposed to about two hours if the full GEOMETRY tape was used.

Monte Carlo

The purpose of the Monte Carlo was to determine the spectrometer acceptance by simulating the spectrometer's geometrical acceptance, hardware and trigger inefficiencies, secondary absorption and decay, and the software event reconstruction programs. The spectrometer

acceptance was then used to calculate the cross sections for the various reactions studied. A brief description of the Monte Carlo follows. More information may be found in References 41-42.

Event generation

Event generation began by selecting a beam track from a special file containing a random sampling of reconstructed tracks from the LASS output tapes. The beam track was then extrapolated into the target and a z-vertex position chosen such that the vertex position distribution correctly described the target absorption. The final state particle momenta were then generated using the standard Monte Carlo generating routine SAGE. A multiperipheral production mechanism with an exponential t-distribution was assumed and corrections were made for the Fermi motion of the liquid deuterium target and for the energy losses in the target and the target walls.

Particle tracking in spectrometer

The event having thus been defined, it was then necessary to follow the tracks through the spectrometer. The particles were tracked through the uniform field of the solenoid by calculating helices for each particle using the particle's four momentum. They were swum through the fringe fields of the solenoid and dipole magnets by a Runge Kutta procedure using solenoid and dipole field maps and were fit to straight lines in the twist and downstream regions.

A particle was assumed to be totally absorbed if it struck any of the physical boundaries of the spectrometer (i.e., magnet walls, chamber

boundaries, etc.) and its tracking stopped at that point. The intersection of the track with the active area of a detector corresponded to a possible hit. Whether or not the detector theoretically fired was determined by generating a random number and using the experimental chamber efficiencies. If the detector fired, the coordinate was stored in a hit array for use in the event reconstruction routines.

Produced particle absorption in the target was accounted for by assigning a weight, determined by the absorption length in the target, to each event. Absorption throughout the rest of the active area of the spectrometer was accounted for as follows. The spectrometer was divided into four regions: 1) the cylinder chambers, 2) the solenoid plane chambers, 3) the C1 Cherenkov counter, and 4) the downstream (dipole) chambers. An absorption length was determined for each of these regions according to the amount of material in them. The absorption probability was then calculated from the absorption length and the length of the track in that region. The particle was then determined to either be absorbed or not be absorbed depending on the combination of a randomly generated number and the absorption probability. If the particle was determined to be absorbed, the tracking stopped at the point of absorption.

Particle decays were accounted for by calculating a decay length from the particle's lifetime in conjunction with a random number. If the particle travelled the decay length, then the tracking again stopped at that point. Multiple scattering throughout the spectrometer and

energy losses outside of the target were found to be negligible and therefore not included in the Monte Carlo.

Event reconstruction

The track finding in the Monte Carlo was designed to simulate that in the LASS production job. Match points were determined from the coordinate hit arrays and trial tracks established from these match points. Corroborating hits were looked for in the other detectors and before the trial track was accepted as an actual detected track it had to pass a number of criteria designed to determine if it would have been found in the LASS track finding programs. If a track was determined to be unreconstructable, the event was determined likewise. Finally, if the event was reconstructed, then the hit arrays were examined to determine if the trigger (T0) was satisfied.

Once an event was reconstructed and satisfied the trigger requirements, it was passed on to the same VRHUNT and MVFIT programs used in the "real" data analysis.

CHAPTER 7. RESULTS

This experiment was conducted to investigate the validity of the OZI rule. The cross sections have been measured for the reactions $\pi^+ n \rightarrow \phi p$ and $\pi^+ p \rightarrow \phi \Delta^{++}$ both of which are forbidden by the OZI rule. These results are compared with the predictions of some of the theoretical models described in Chapter 2. Also of primary interest in this experiment was the reaction $\pi^+ n \rightarrow K^+ \phi \Lambda$. This reaction has never been measured before and is particularly interesting because it contains both an OZI allowed diagram and OZI violating diagram. An upper limit for the cross section of this reaction has been determined. Finally, a search has been made for the phi prime meson in the $K_S^0 K^+ \pi^-$ and $K^+ K^- \pi^+ \pi^-$ decay modes and upper limits for these cross sections have been established. In order to calculate these various cross sections, it was necessary to know the normalization for the experiment. First, the method of determining the normalization will be described and then each of the reactions will be considered.

Normalization

The heading for this section will no doubt alarm and disgust any thinking person who is not familiar with the methods of particle physics. In order to dispel their fears, it should be explained that this "normalization" of the data is in no way similar to the "normalization" process practiced by such institutions as democracy, socialism, christianity, and death, whose common goal it is to make everyone equal, average, normal, middle class, mediocre, zero; in other words, the

sexless herd. The normalization that is done in particle physics is done for quite the opposite reason; it is done so that data from different reactions and different experiments may be compared and the differences understood - not equalized. (And lo, the data do show that not all cross sections are equal; but, shh, don't mention this in Washington!)

The data were normalized to account for the geometrical acceptance of the spectrometer and the inefficiencies that were inherent both in the apparatus and in the software analysis programs. This was accomplished by first calculating the instrumental sensitivity for the experiment as follows:

$$S = \frac{N_1}{\sigma_1} = B\rho L \quad (7.1)$$

where S = sensitivity (events/nb)

B = number of incident beam particles (corrected)

ρ = target density ($5.00 \times 10^{22}/\text{cm}^3$)

L = length of target (91.44 cm)

$$B = N_B f_{\text{ATN}} f_{\text{DT}}^{-1} f_{\text{VERT}} f_{\pi} f_G$$

N_B = number of π beam particles measured on scalars

$$= 3.67 \times 10^8$$

f_{ATN} = 1 - fraction of beam absorbed

$$= 1 - \frac{\rho L \sigma_{\text{inelastic}}}{2} \quad \sigma_{\text{in}} = 44.8 \times 10^{-27} \text{ cm}^2$$

$$= 0.90$$

f_{DT} = 1 - fraction of beam missed by scalers because of beam pile-up

$$= 0.99$$

f_{VERT} = 1 - fraction of beam outside vertex cuts

$$= 1.0$$

f_{π} = fraction of the beam π 's that are actually π 's

$$= 1.0$$

f_G = 1 - fraction of beam shaded by Glauber screening (43)

$$= 0.96$$

$$B = 3.30 \times 10^8$$

and

$$S = 1.51 \text{ events/nb} \quad .$$

The sensitivity simply states how many events correspond to a particular cross section; that is, it relates the final corrected number of events observed to a measure of the probability for producing events of that type. The final corrected number of events N_i for a particular reaction i was determined from the expression:

$$N_i = n_i (F_{fatal}^{-1}) (F_v^{-1}) \quad (7.2)$$

where N_i = final corrected number of events

n_i = number of acceptance corrected events. The acceptance was calculated from the Monte Carlo and includes the geometric acceptance and losses due to track finding inefficiencies, decay probabilities of produced particles, and interaction particles.

F_{fatal} = 1 - fraction of events lost due to KFAIL problems (un-
 packing problems, garbled raw data, beam track recon-
 struction problems, etc.)
 = 0.94
 F_v = vertex finding efficiency
 = 0.90 .

The target density used in this calculation was monitored throughout the experiment and run-to-run variations were less than 1%.

Study of the Reaction $\pi^+ n \rightarrow \phi p$
 $\quad \quad \quad \hookrightarrow K^+ K^-$

The quark line diagram for this reaction is shown in Fig. 7.1; here the phi has been interpreted as a completely strange meson; i.e., ideal mixing has been assumed. This is a disconnected hairpin diagram and is therefore forbidden by the OZI rule; that is, the OZI rule predicts this reaction should never occur and the degree to which it does occur is a measure of the violation of the OZI rule. The cross section for this reaction has been measured in this experiment.

Only three prong events with charge +1 and no missing neutrals were used for this study. Events with missing neutral particles were eliminated by requiring energy and momentum conservation. The missing energy, missing momentum, and missing mass squared plots are shown in Fig. 7.2. The data were required to satisfy the following cuts:

missing energy	$-1.0 < \Delta E < 1.5 \text{ GeV}$
(missing transverse momentum) ²	$\Delta PT^2 < 0.04 \text{ (GeV/c)}^2$
missing longitudinal momentum	$-0.8 < \Delta PZ < 1.0 \text{ GeV/c}$
(missing mass) ²	$ MM^2 < 0.05 \text{ GeV}^2$

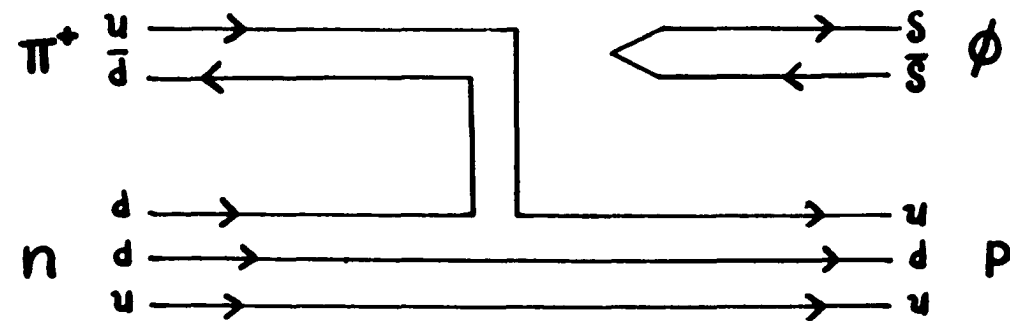


Figure 7.1. Quark line diagram for the OZI violating reaction $\pi^+ n \rightarrow \phi p$

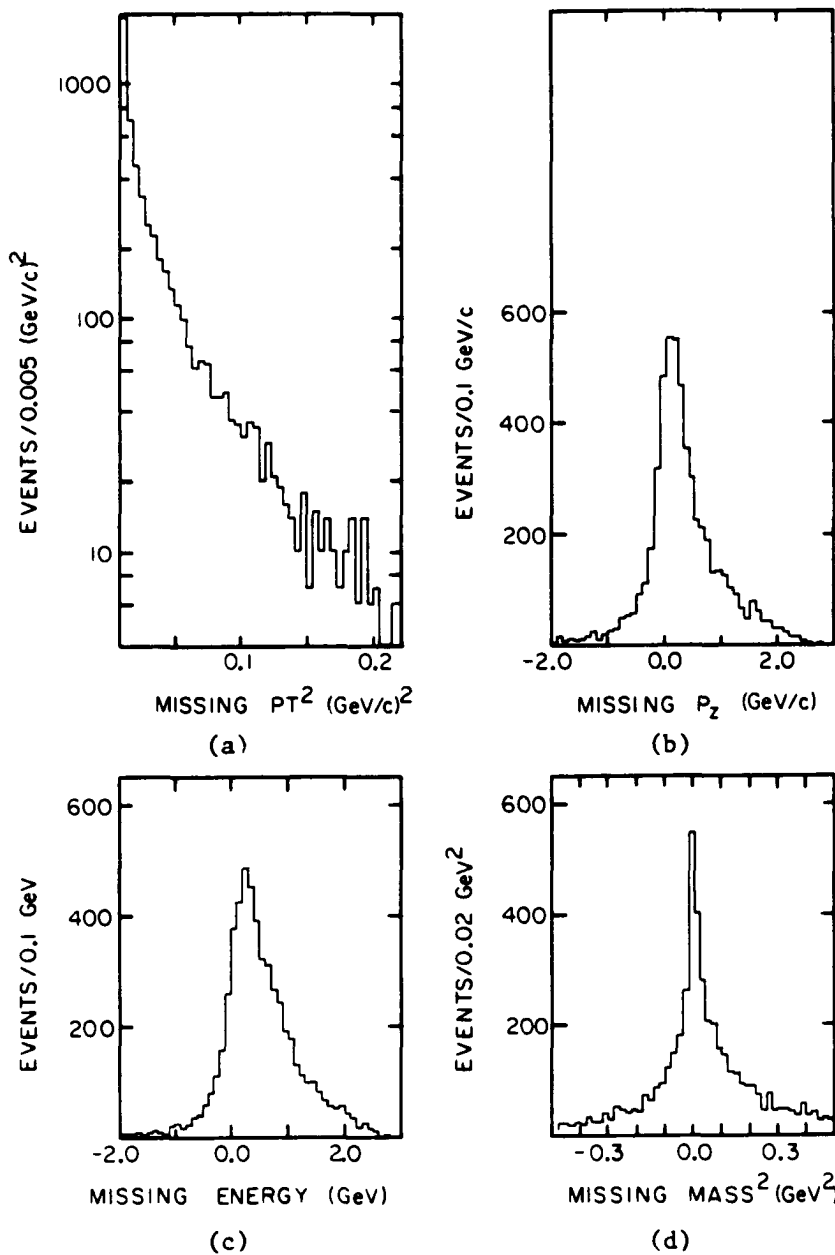


Figure 7.2. Missing energy, momentum and mass² for the reaction $\pi^+ n \rightarrow K^+ K^- p$

- (a) Missing transverse momentum squared.
- (b) Missing longitudinal momentum.
- (c) Missing energy.
- (d) Missing mass².

Monte Carlo simulation of this reaction which assumed a t -distribution of e^{-2t} indicated that there were virtually no kaons of momentum less than 3.5 GeV/c; therefore, each event was required to have two kaons each with a momentum greater than 3.5 GeV/c. The Monte Carlo studies also showed that the proton always had a momentum less than 2.0 GeV/c and such a requirement was placed on the data. The time-of-flight counter, located directly behind the Cherenkov counter C1, distinguished protons from pions and kaons up to 2.0 GeV/c, and thus provided a positive identification for protons.

Figure 7.3 shows the K^+K^- invariant mass distribution for this reaction. The computed mass resolution in the region of the ϕ is ± 5 MeV. The background was fit to a polynomial with an imposed threshold effect. The background under the ϕ signal is due to two sources: nonresonant K^+K^- pairs and $p\bar{p}$ pairs. A large K^+K^- background is expected since the reaction $\pi^+n \rightarrow K^+K^-p$ is allowed by the OZI rule. The $p\bar{p}$ background is expected to be comparable to the $K\bar{K}$ background at this energy. The raw ϕ signal corresponds to 26 events above background and must be corrected for acceptance as explained in the Normalization section. The Monte Carlo generated acceptance is shown in Fig. 7.4 and results in an acceptance correction factor of 4.3. The number of acceptance corrected events is then 112 and the cross section as determined from Eqs. 7.1 and 7.2 is:

$$\sigma(\pi^+n \rightarrow \phi p) = 179 \pm 72 \text{ nb} \quad .$$

The cross section for the reaction $\pi^-p \rightarrow \phi n$ has been measured to be

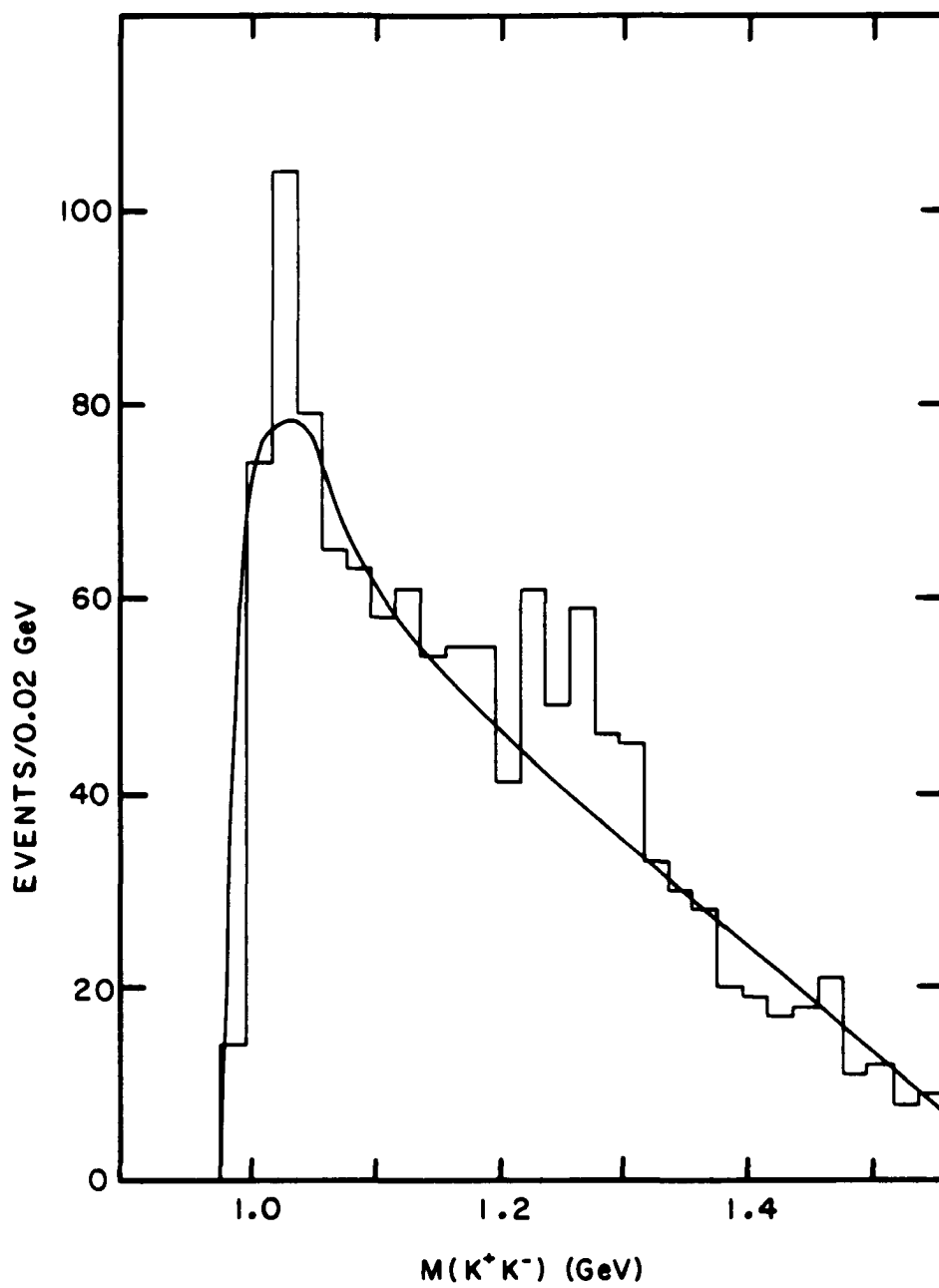


Figure 7.3. K^+K^- invariant mass for the reaction $\pi^+n \rightarrow K^+K^-p$

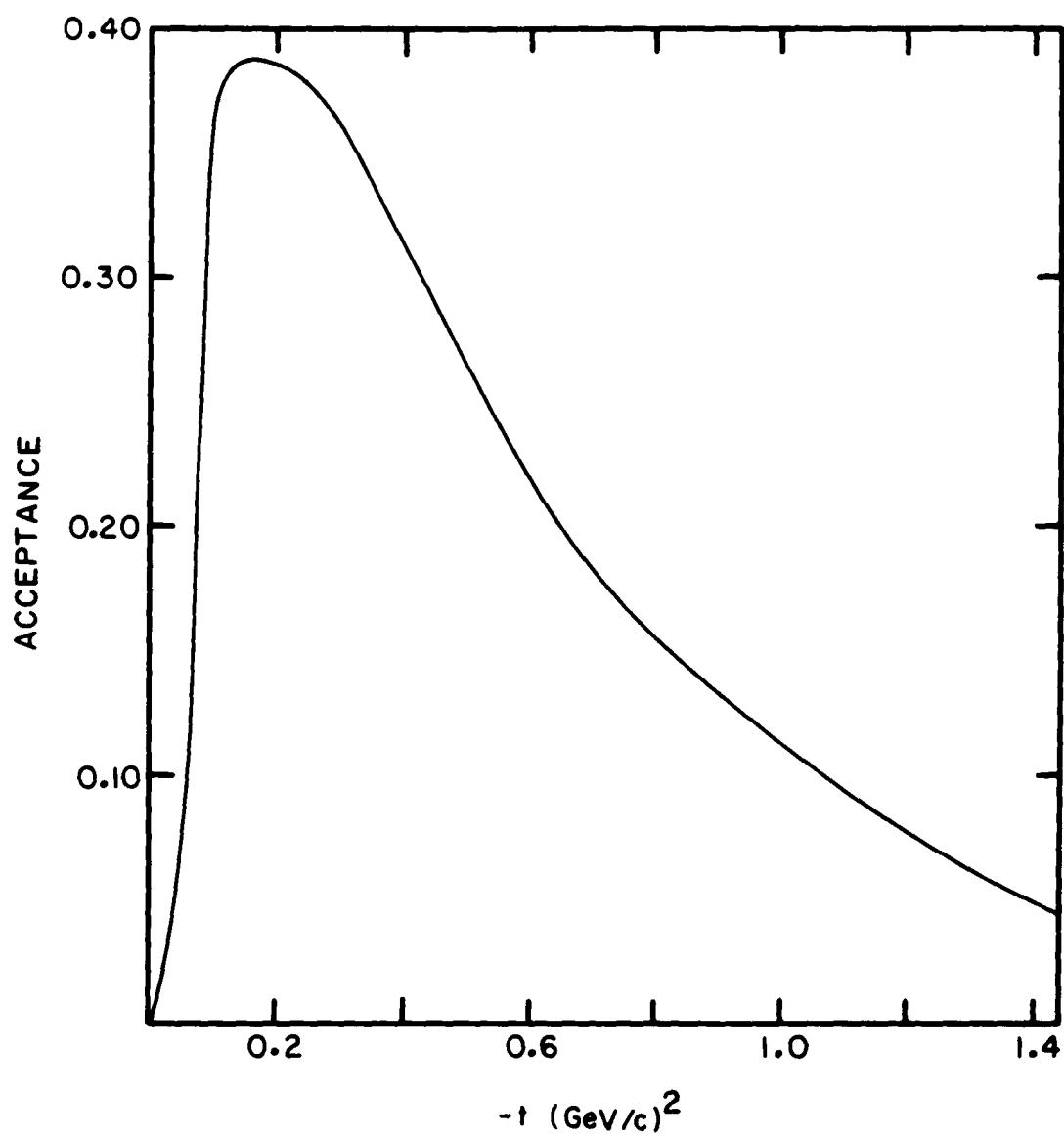


Figure 7.4. Monte Carlo generated acceptance for the reaction $\pi^+ n \rightarrow \phi p$

$263 \pm 56 \text{ nb } [|\mathbf{t}| < 0.5(\text{GeV}/c)^2]$ at 11 GeV/c (44). This reaction is related to the reaction $\pi^+ n \rightarrow \phi p$ by charge conjugation; and the two cross sections are in agreement within errors.

The fact that events of the type $\pi^+ n \rightarrow \phi p$ have been observed is an indication that the OZI rule is violated. A possible interpretation of this result is to consider the ϕ as having a nonstrange component, i.e., not ideally mixed; and that the ϕ is produced solely by its nonstrange component via the OZI allowed diagram of Fig. 2.5. The amount of mixing (i.e., the magnitude of the nonstrange component) is calculated from Sakurai's ω - ϕ mixing model. The validity of this interpretation can be checked as follows. Since the ω and the ϕ are mixed, each contains a strange component and the amount of each component that the ω and the ϕ contain is determined by the mixing angle. The mixing angle has been determined by a number of independent methods and all are in agreement with the value determined from the Gell-Mann-Okubo quadratic mass formula $\theta_{\text{mixing}} \approx 40^\circ$. In the same manner that the reaction $\pi^+ n \rightarrow \phi p$ must proceed via the nonstrange component of the ϕ , the reaction $\pi^+ n \rightarrow \omega p$ must also proceed via the nonstrange component of the ω . Therefore, the ratio

$$R = \frac{\sigma(\pi^+ n \rightarrow \phi p)}{\sigma(\pi^+ n \rightarrow \omega p)}$$

is entirely determined by the mixing angle (neglecting phase space differences) and is determined to be

$$R = \frac{\sigma(\pi^+ n \rightarrow \phi p)}{\sigma(\pi^+ n \rightarrow \omega p)} = 0.0037 \pm 0.0003$$

for $\theta_{\text{mixing}} = 40^\circ$.

The data for these reactions are shown in Fig. 7.5. Also shown are the cross sections for the similar reaction $\pi^+ n \rightarrow \rho^0 p$. The difference between the ρ^0 and the corresponding ω cross sections is generally thought to be due to the fact that the ω reactions are largely spin flip, while the ρ^0 reactions have a large forward nonspin-flip amplitude. The data show that

$$R = \frac{\sigma(\pi^+ n \rightarrow \phi p)}{\sigma(\pi^+ n \rightarrow \omega p)} = 0.0037 \pm 0.0015$$

which is in excellent agreement with the predicted value.

The conclusion is then, that the violation of the OZI rule is a result of the deviation from ideal ω - ϕ mixing; that is, the reaction $\pi^+ n \rightarrow \phi p$ does not proceed via the OZI forbidden diagram of Fig. 7.1 but rather by the OZI allowed diagram of Fig. 2.5. (In terms of QCD, the reaction of Fig. 6.2 occurs by coupling the phi to the rest of the reaction through three gluons. This is entirely equivalent to mixing the omega and the phi (Fig. 2.3), thus giving the phi a nonstrange component, and considering the reaction to occur through the diagram of Fig. 2.5.) The term violation, as used here, does not indicate a deficiency of the OZI rule; rather, it may be equated with deviation from ideal mixing. The phi production, as described here, is then entirely accounted for by the simple mixing model and there is no need to include more bells and whistles as prescribed by the quark fusion

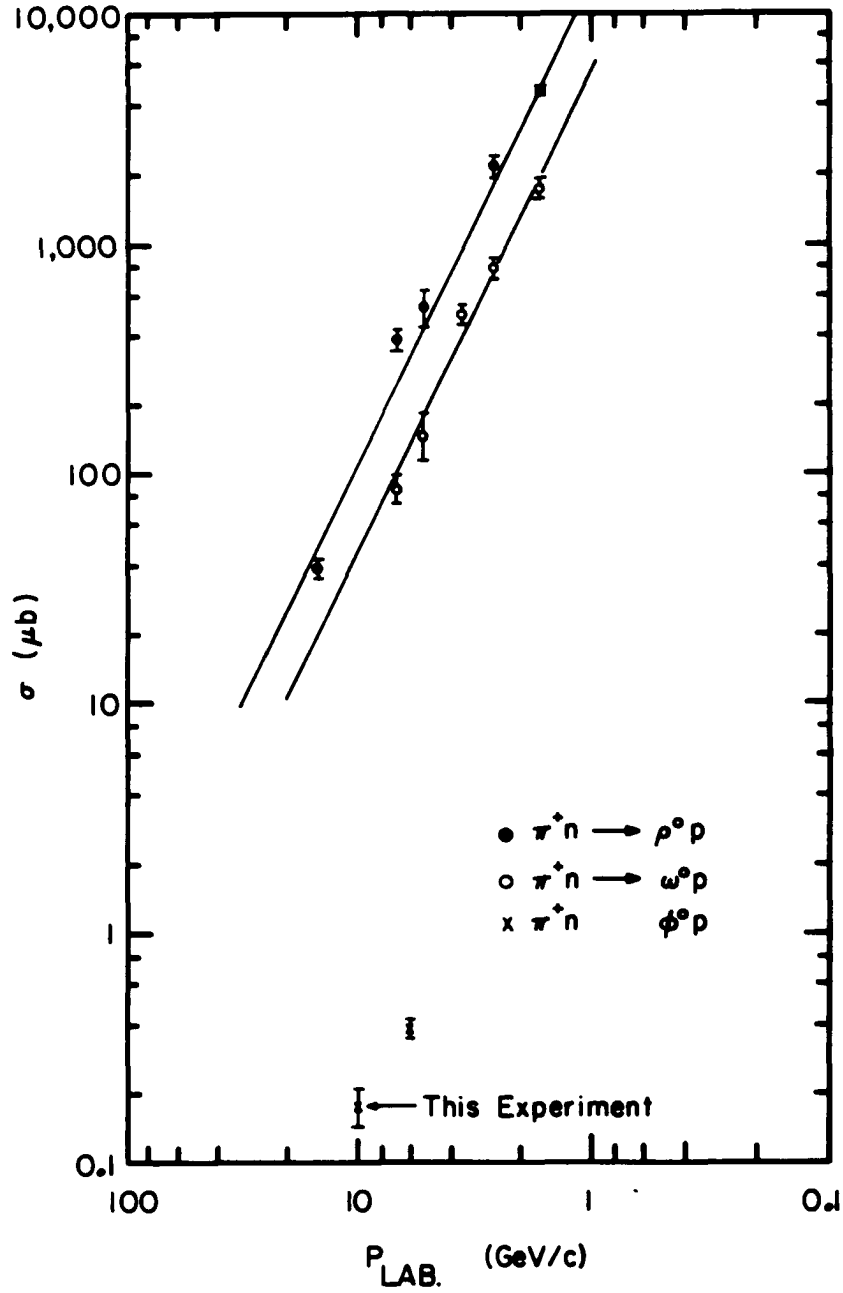
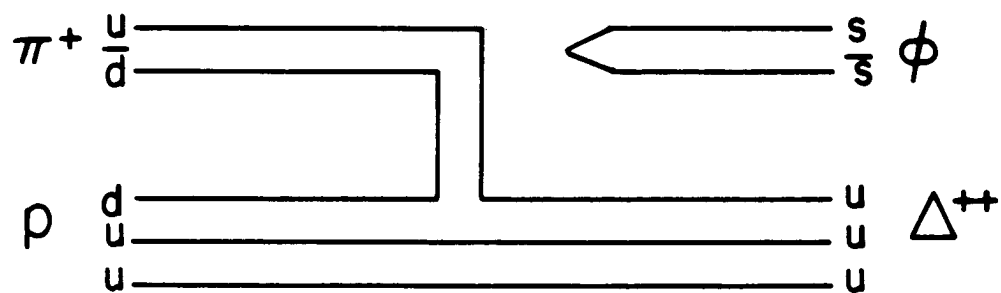
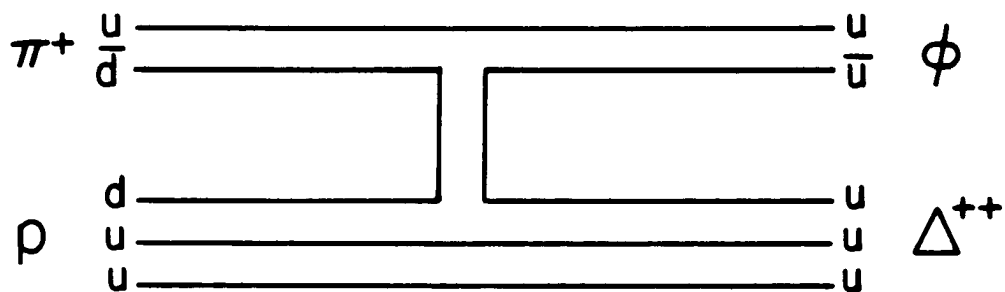


Figure 7.5. Cross sections for the reactions $\pi^+ n \rightarrow V^0 p$ where V^0 represents a neutral vector meson; ρ^0 , ω^0 , or ϕ (Ref. 45)



(a)



(b)

Figure 7.6. Quark line diagrams for the reaction $\pi^+ p \rightarrow \phi \Delta^{++}$
 (a) OZI forbidden diagram (ideal ω - ϕ mixing).
 (b) OZI allowed diagram (nonideal ω - ϕ mixing).

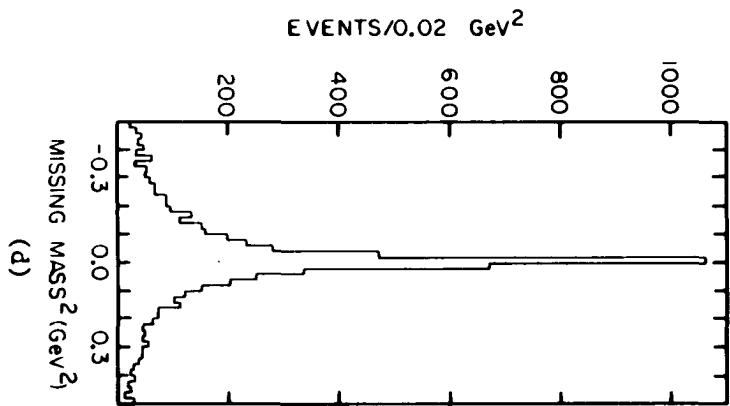
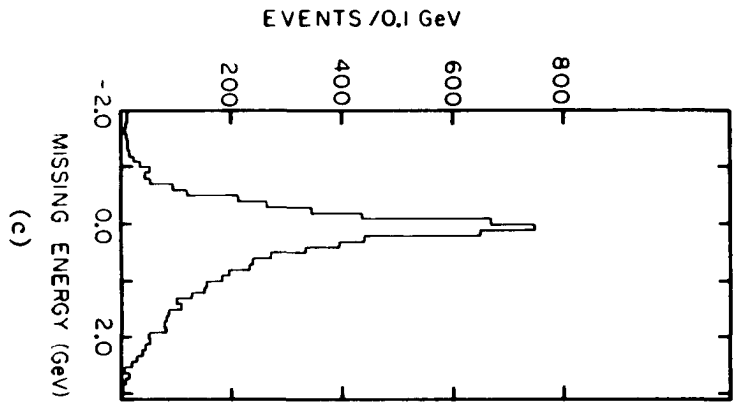
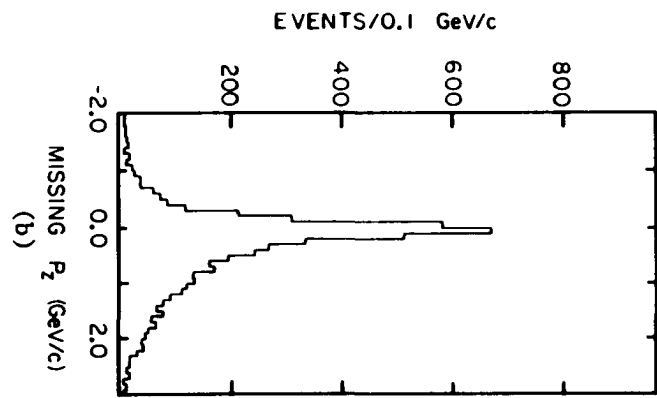
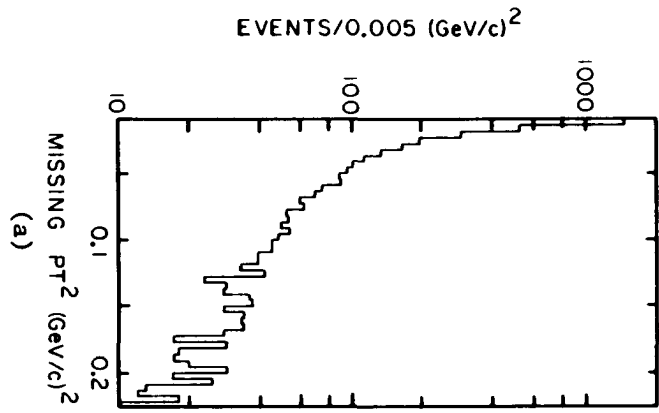
excluded from the sample by imposing energy and momentum conservation. The missing energy, momentum and mass squared plots are shown in Fig. 7.7 and the following cuts were applied to the data:

$$\begin{array}{ll}
 \text{missing energy} & -1.0 < \Delta E < 1.0 \text{ GeV} \\
 (\text{missing transverse momentum})^2 & \Delta_{PT}^2 < 0.04 \text{ (GeV/c)}^2 \\
 \text{missing longitudinal momentum} & -0.9 < P_Z < 1.0 \text{ GeV/c} \\
 (\text{missing mass})^2 & |MM^2| < 0.05 \text{ GeV}^2
 \end{array}$$

The Monte Carlo for this reaction indicated that there were no kaons with a momentum less than 3.2 GeV/c and that the proton's momentum was always less than 2.0 GeV/c; consequently, these cuts were applied to the data. The fourth particle was required to be a slow π^+ and the $p\pi^+$ invariant mass (Fig. 7.8) was required to lie within the Δ^{++} region ($\text{mass}(p\pi^+) < 1.35 \text{ GeV}$). A fit to the $p\pi^+$ -mass distribution of a Breit-Wigner for the Δ^{++} resonance plus a fifth order polynomial background showed that this cut resulted in a sample which contained 83% of all true Δ^{++} events and a 29% background of non- Δ^{++} events. The strength of the Δ^{++} signal as determined in this fit was used for the cross section determination. Thus, the cuts imposed on the data resulted in a sample of events of the typed $\pi^+ p \rightarrow K^+ K^- \Delta^{++}$. Figure 7.9 shows the $K^+ K^-$ invariant mass distribution for this sample of events. The strength of the phi signal was determined by fitting the background to a polynomial. The large background under the phi signal is again due to nonresonant $K^+ K^-$ pairs and $p\bar{p}$ pairs - the $K^+ K^-$ pairs coming mainly from the OZI allowed reaction $\pi^+ p \rightarrow K^+ K^- \Delta^{++}$. The 19 phi events above background correspond to 122 acceptance (Fig. 7.10) corrected

Figure 7.7. Missing energy, momentum and mass² for the reaction
 $\pi^+p \rightarrow K^+K^-\pi^+p$

- (a) Missing transverse momentum squared.
- (b) Missing longitudinal momentum.
- (c) Missing energy.
- (d) Missing mass².



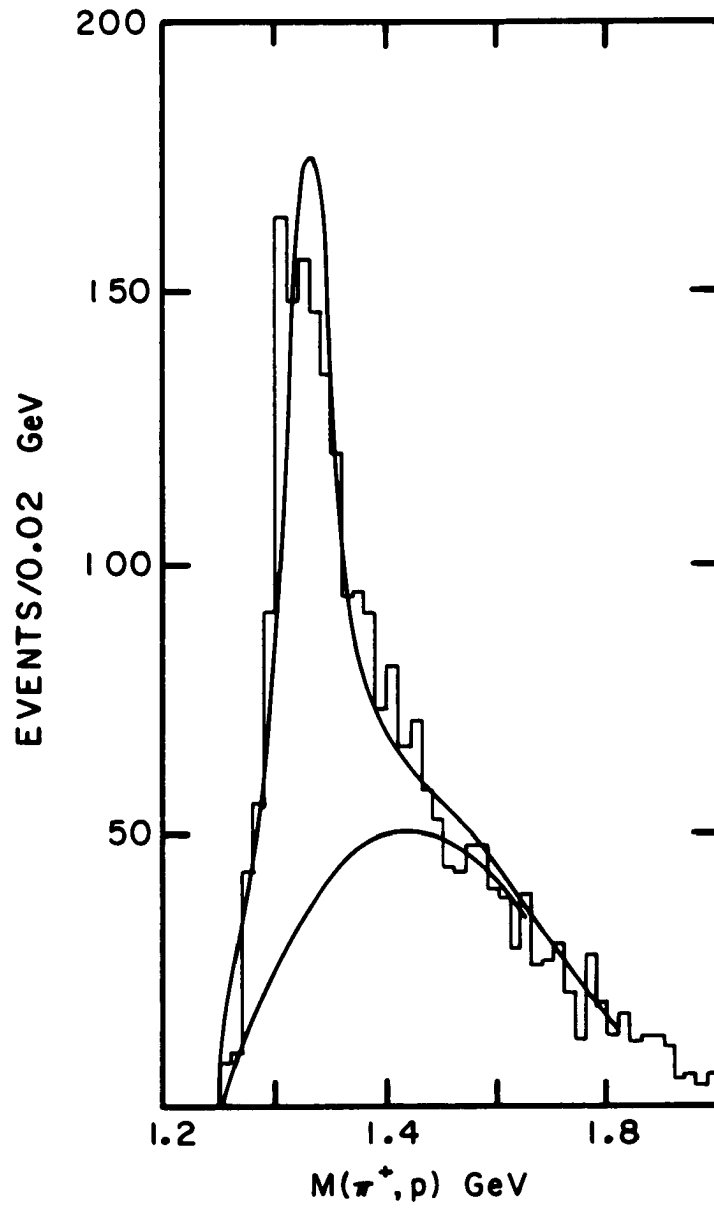


Figure 7.8. $\pi^+ p$ mass distribution for the reaction $\pi^+ p \rightarrow K^+ K^- \pi^+ p$

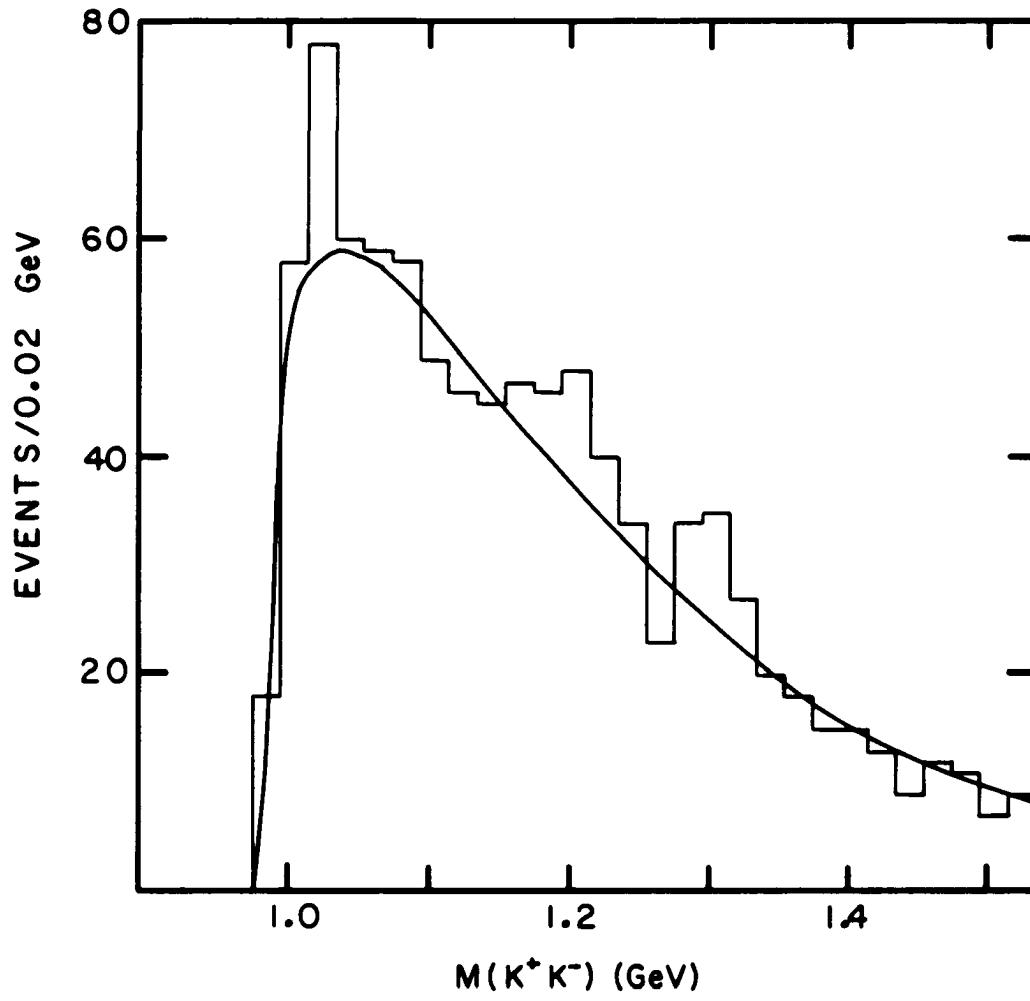


Figure 7.9. K^+K^- mass distribution for the reaction $\pi^+ p \rightarrow K^+ K^- \Delta^{++}$

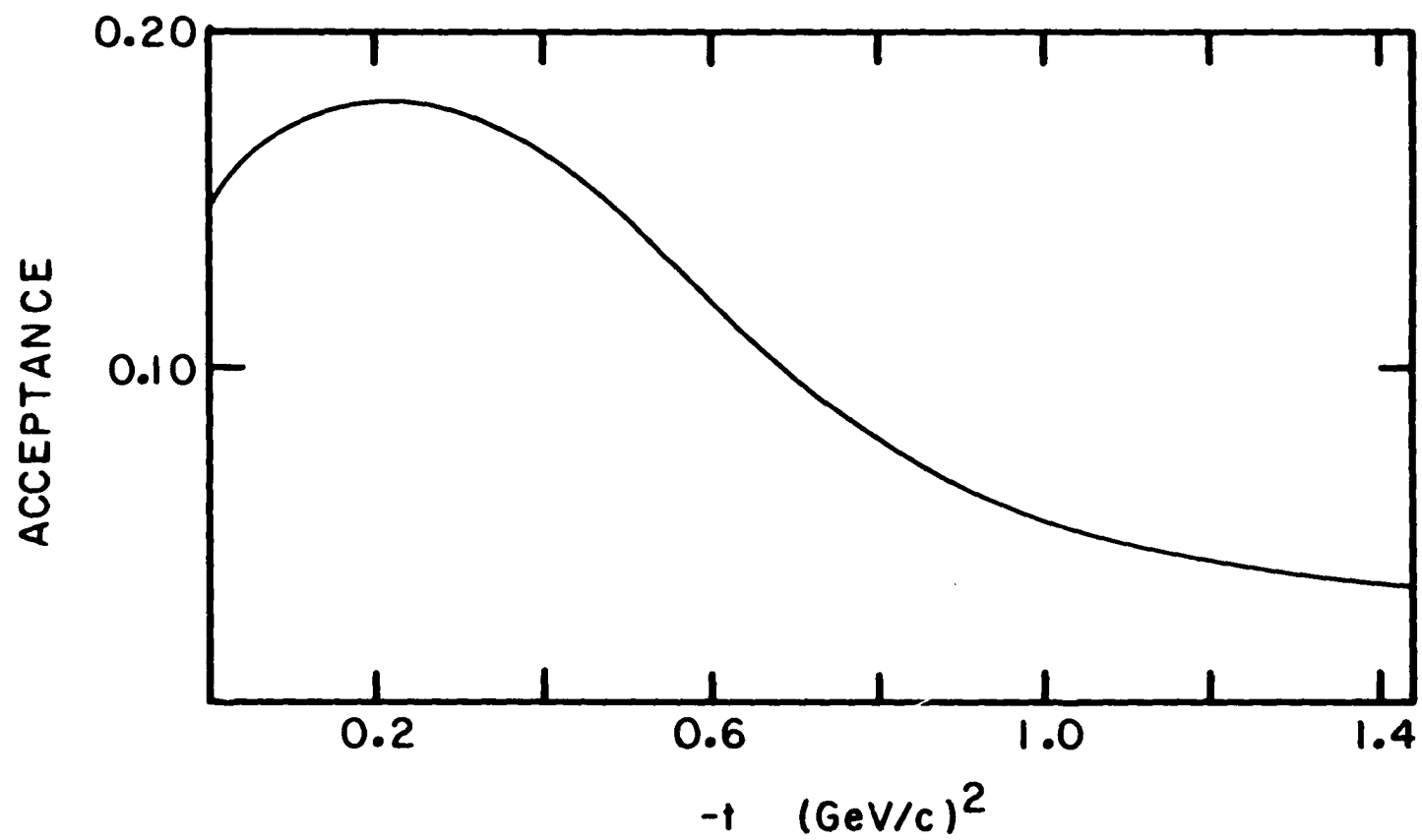


Figure 7.10. Monte Carlo generated acceptance for the reaction $\pi^+ p \rightarrow \phi \Delta^{++}$

events; the resulting cross section is then

$$\sigma(\pi^+ p \rightarrow \phi \Delta^{++}) = 172 \pm 75 \text{ nb} .$$

The interpretation of this result is identical to that for the reaction $\pi^+ n \rightarrow \phi p$. The production of the phi in the reaction $\pi^+ p \rightarrow \phi \Delta^{++}$ is entirely consistent with the phi being produced solely by its non-strange component via the diagram of Fig. 7.6b. This is shown by comparing the cross section for this reaction with the corresponding OZI obeying reaction in which the vector meson is the omega meson, i.e., $\pi^+ p \rightarrow \omega \Delta^{++}$. Data for this reaction are shown in Fig. 7.11 along with the measurement of this experiment. These data show that

$$R = \frac{\sigma(\pi^+ p \rightarrow \phi \Delta^{++})}{\sigma(\pi^+ p \rightarrow \omega \Delta^{++})} = 0.0026 \pm 0.0011$$

which is in agreement within errors with the calculated value

$$R = \frac{\sigma(\pi^+ p \rightarrow \phi \Delta^{++})}{\sigma(\pi^+ p \rightarrow \omega \Delta^{++})} = 0.0037 \pm 0.003 .$$

$$\text{Study of the Reaction } \pi^+ n \rightarrow K^+ \phi \Lambda^0 \rightarrow \pi^- p$$

$\begin{array}{c} \xrightarrow{\quad} \\ \searrow \quad \swarrow \\ K^+ \quad K^- \end{array}$

This reaction is unique in that it can proceed via either an OZI allowed diagram (Fig. 7.12a) or an OZI forbidden diagram (Fig. 7.12b). Thus, it is particularly interesting in that it provides a test of the OZI rule within one final state. This reaction was searched for by first selecting three prong + Vee events in which the Vee particles were consistent with $\pi^- p$ identification and the other three particles were charged kaons. Lambdas were selected by requiring the $\pi^- p$ invariant

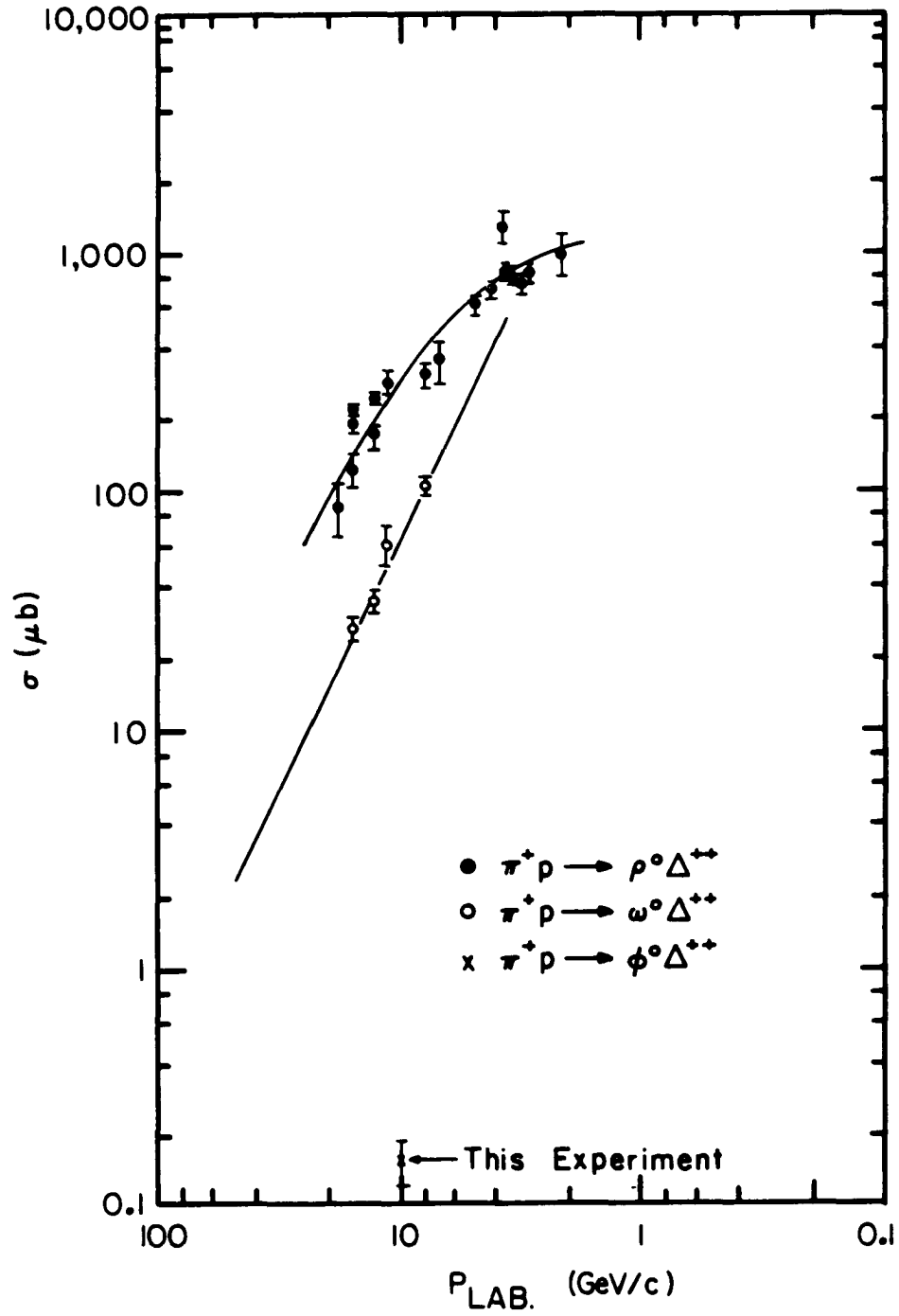


Figure 7.11. Cross sections for the reactions $\pi^+ p \rightarrow V^0 \Delta^{++}$ where V^0 represents a neutral vector meson; ρ^0 , ω^0 , or ϕ (Ref. 47)

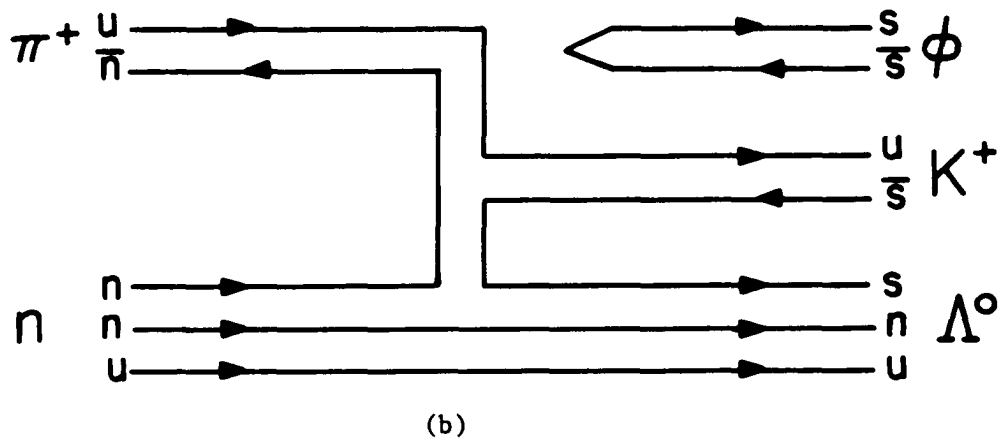
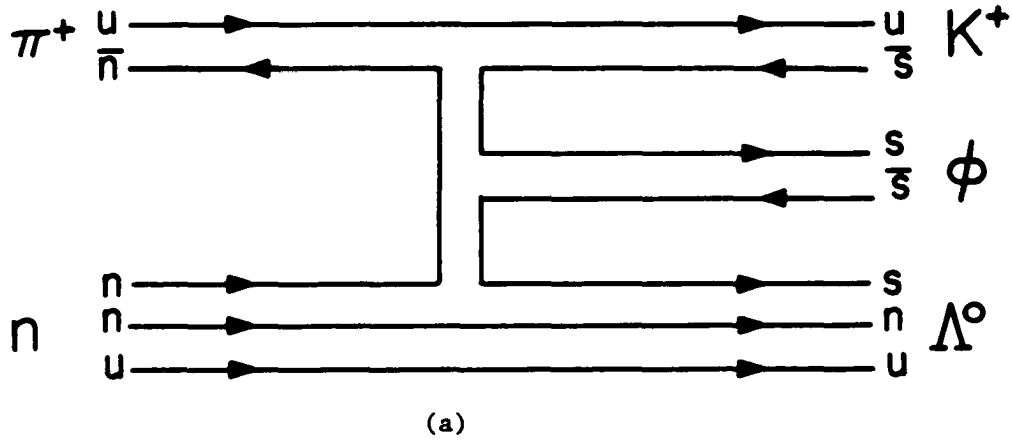


Figure 7.12. Quark line diagrams for the reaction $\pi^+ n \rightarrow K^+ \phi \Lambda^0$

(a) OZI allowed diagram.

(b) OZI forbidden diagram.

mass to be $1.105 < m(\pi^- p) < 1.125$ GeV (Fig. 7.13). The $\pi^- p$ mass distribution was fit to a Gaussian on a smooth background and indicated that the above cut resulted in a sample which contained 98% of all true lambda events and a 17% background of nonlambda events. The lambda was required to be at the bottom vertex by requiring its momentum to be less than 3.3 GeV/c. Energy and momentum were conserved by imposing the following cuts:

$$-0.5 < \Delta P_Z < 0.6 \text{ GeV/c}$$

$$\Delta P_T^2 < 0.05 \text{ (GeV/c)}^2$$

$$-0.3 < M^2 < 0.5 \text{ GeV}^2 \quad .$$

The $K^+ K^-$ invariant mass plot shown in Fig. 7.14 is consistent with no phi signal. The cross section upper limit is calculated using the cumulative Poisson distribution. The four background events in the phi region correspond, with a 95% confidence level, to a mean in the Poisson distribution of nine events. The upper limit on the phi signal is then five events. The Monte Carlo generated acceptance for this reaction which assumed a t-distribution of e^{-2t} for both the $\pi-\phi$ vertex and the $n-\Lambda$ vertex, was 16%. The cross section upper limit, corrected for the $\Lambda \rightarrow \pi^- p$ branching ratio of 0.64 and the $\phi \rightarrow K^+ K^-$ branching ratio of 0.49, is then $\sigma(\pi^+ n \rightarrow K^+ \phi \Lambda^0) < 66$ nb. This is consistent with theoretical predictions.

Phi Prime Search

The ϕ' is the expected first excited state of the $s\bar{s}$ system. Thus, the OZI rule should also be applicable to the production and

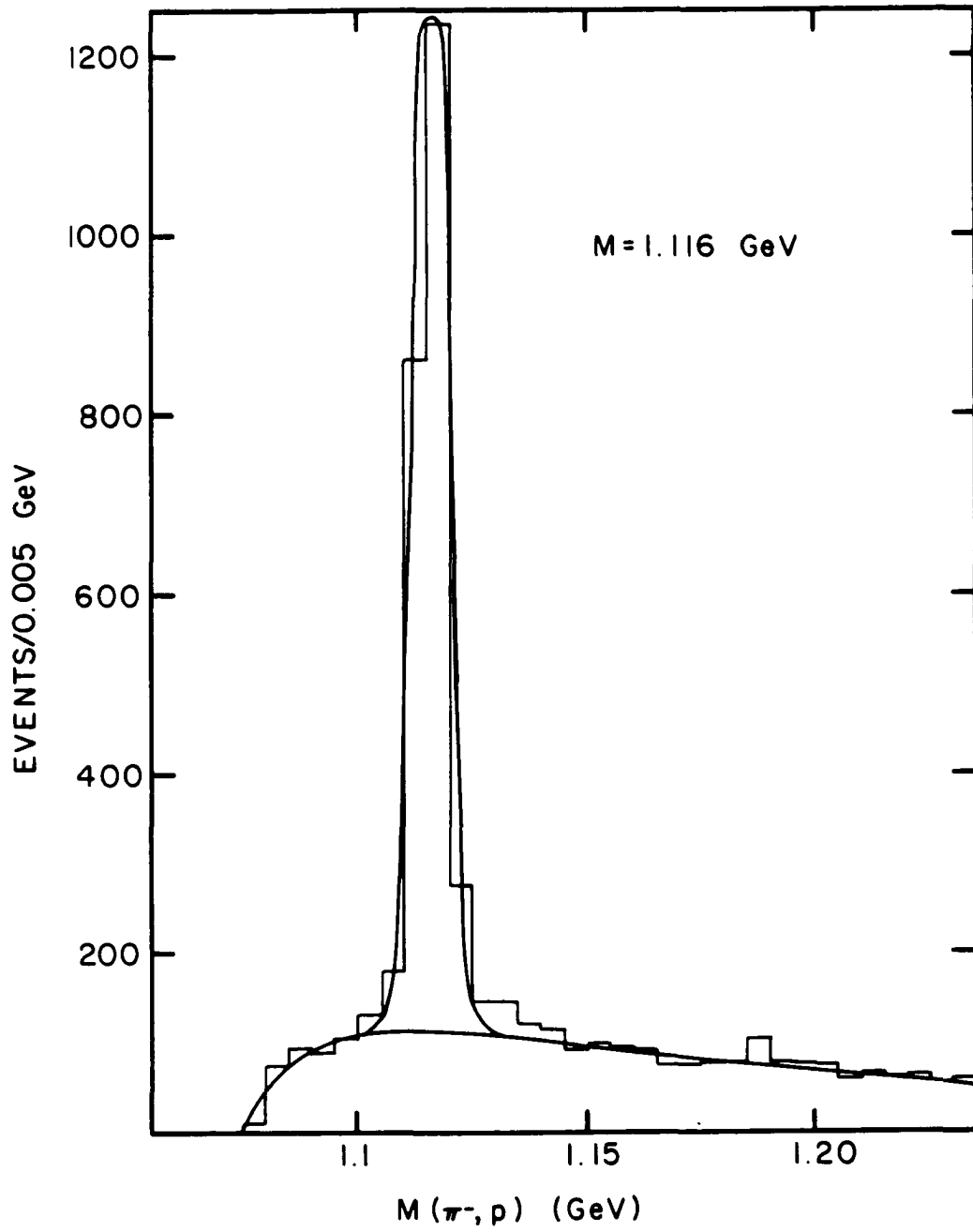


Figure 7.13. $\pi^- p$ mass distribution for the reaction $\pi^+ n \rightarrow K^+ K^- K^- \pi^- p$

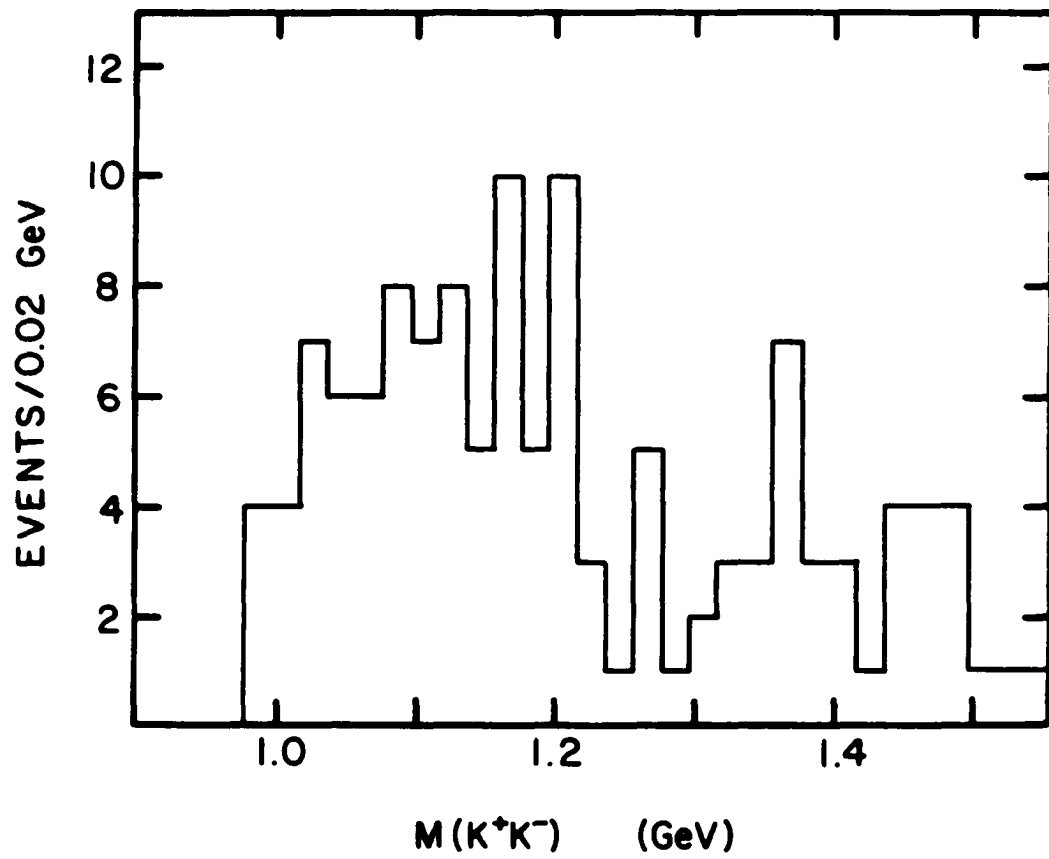
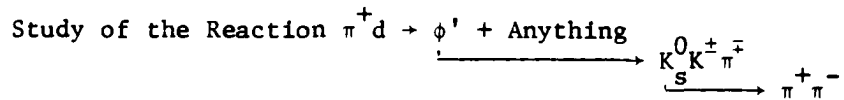
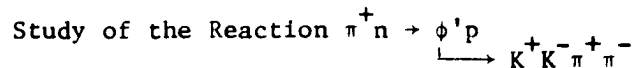


Figure 7.14. K^+K^- mass distribution for the reaction $\pi^+n \rightarrow K^+K^+K^-\Lambda^0$

decay properties of the phi prime. Two of the phi prime's expected decay modes (48), $\phi' \rightarrow K_S^0 K^\pm \pi^\mp$, $\phi' \rightarrow K^+ K^- \pi^+ \pi^-$ are studied in the present experiment. Previous searches for the ϕ' have been inconclusive (49-50).



Only events with a Vee and at least two other tracks were used for this study. K_S^0 's were selected from the $\pi^+ \pi^-$ mass distribution of the Vee particles (Fig. 7.15) by requiring $0.47 < m(\pi^+ \pi^-) < 0.52$ GeV. The mass distribution was fit to a Gaussian plus a third order polynomial background and indicated that the above cut resulted in a sample which contained 100% of all true K_S^0 events and a 17% background of non- K_S^0 events. In addition, the event was required to have a neutral combination of a kaon and a pion. The kaon momentum was required to be greater than 3.0 GeV/c (i.e., greater than the pion threshold in C1). The $K_S^0 K^\pm \pi^\mp$ mass distribution was fit to a smooth curve as shown in Fig. 7.16 and has no obvious structure. The cross section upper limit was calculated assuming a two standard deviation (95% confidence level) variation in the hypothetical signal. The cross section upper limit as a function of mass is shown in Fig. 7.17 and assumes a width of 100 MeV.



This study used only five prong events of charge +1. Events with this final state were selected in the following manner. Momentum conservation was imposed by the following cuts:

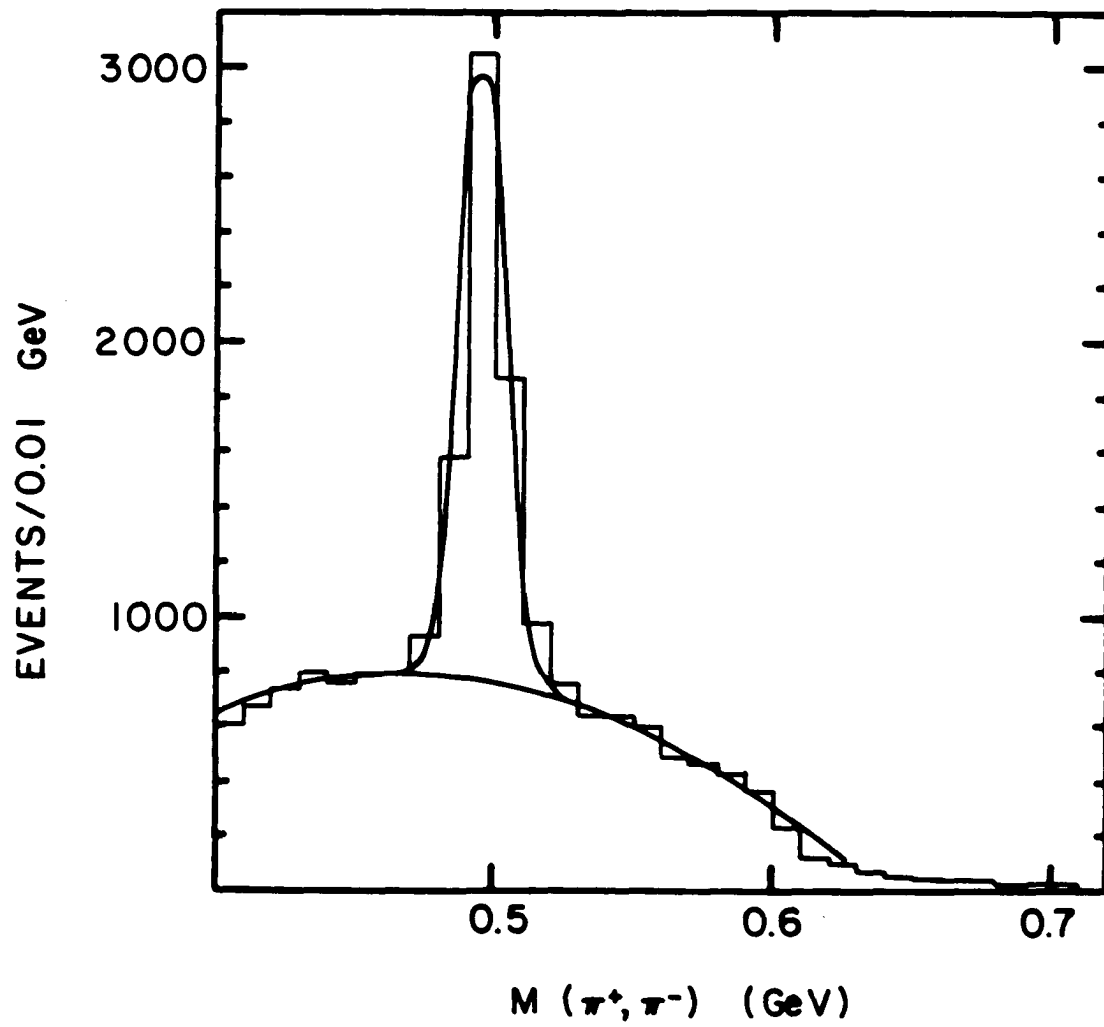


Figure 7.15. $\pi^+\pi^-$ mass distribution for the reaction $\pi^+d \rightarrow \pi^+\pi^-K^+\pi^- + \text{Anything}$

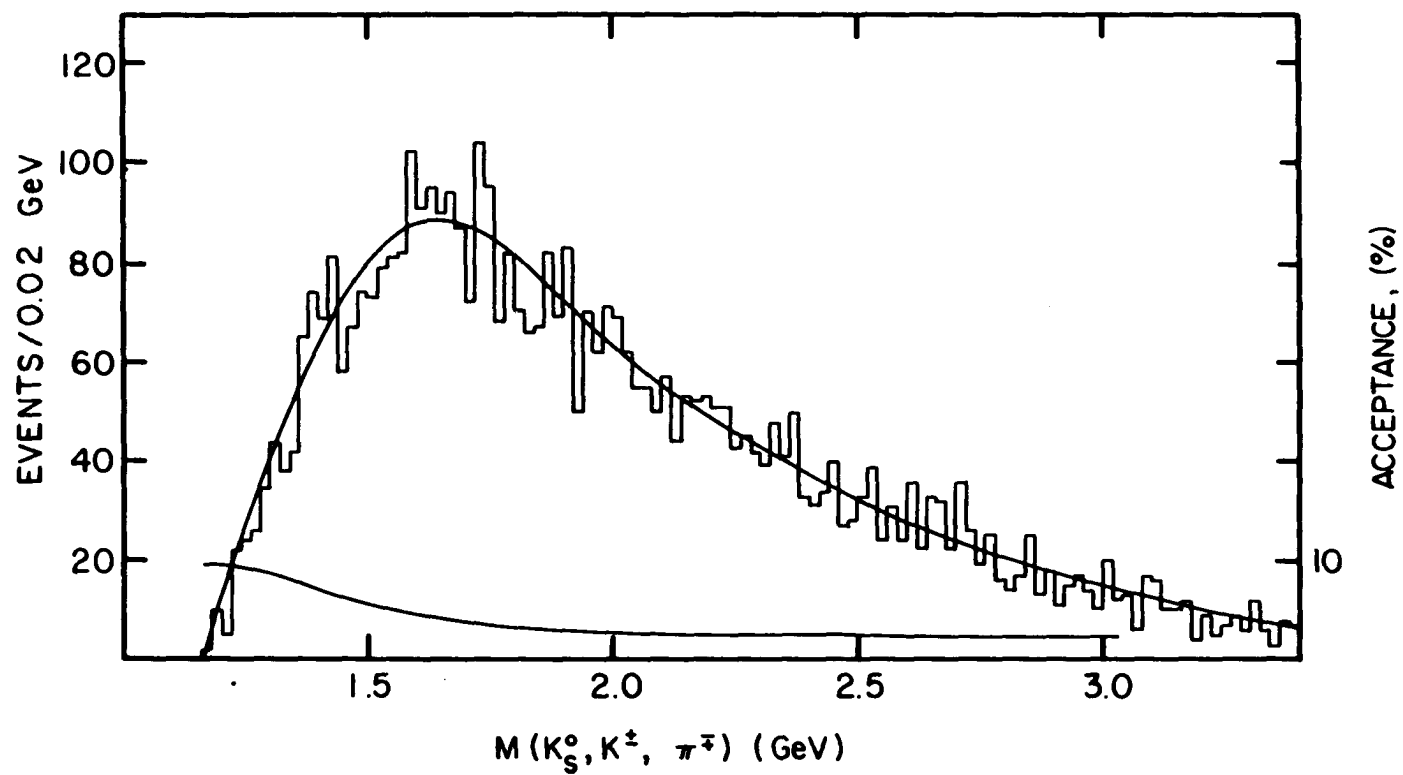


Figure 7.16. $K_S^0 K^\pm \pi^\mp$ mass distribution for the reaction $\pi^+ d \rightarrow K_S^0 K^\pm \pi^\mp + \text{Anything}$. Upper curve is smooth fit to data. Lower curve is acceptance as a function of mass

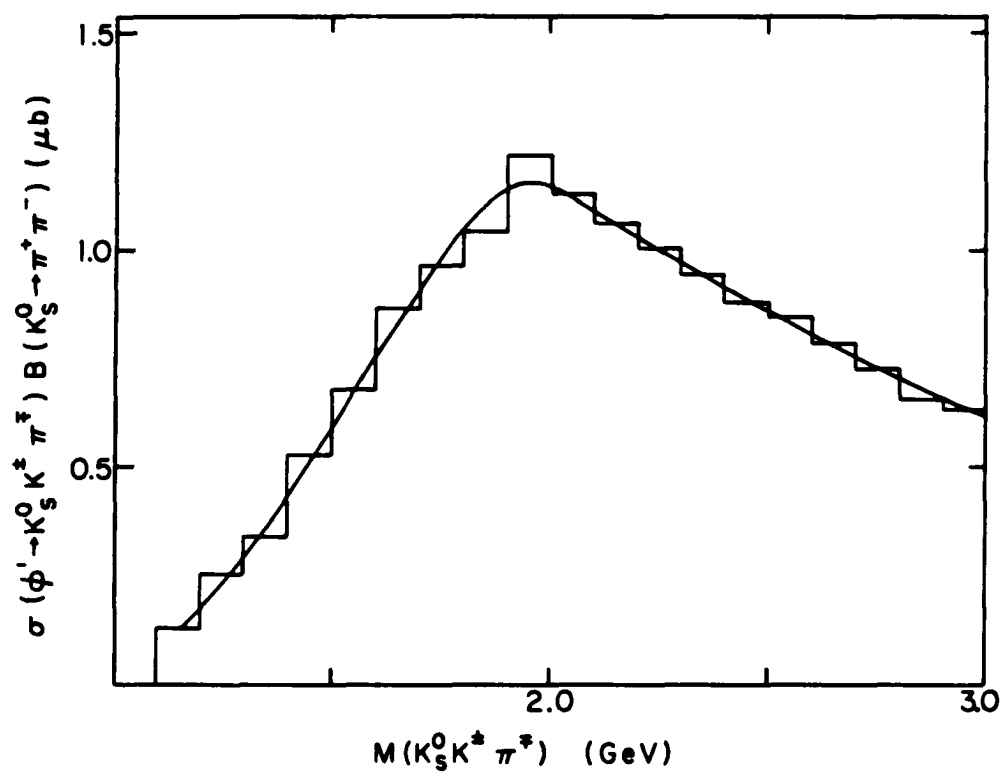


Figure 7.17. The cross section upper limit as a function of mass for $\phi' \rightarrow K_S^0 K^\pm \pi^\mp$ in the reaction $\pi^+ d \rightarrow K_S^0 K^\pm \pi^\mp + \text{Anything}$

$$-0.4 < \Delta P_Z < 0.4 \text{ GeV/c}$$

$$\Delta P_T^2 < 0.03 (\text{GeV/c})^2 .$$

The two fastest particles were assumed to have the same mass, X. The three remaining particles were assumed to be two pions and a proton if consistent with particle identification information. The X-mass² was then calculated from energy and momentum conservation and as shown in Fig. 7.18 there is a clear signal at the kaon mass. The final state $K^+ K^- \pi^+ \pi^- p$ was then selected by requiring $0.1 < m(X)^2 < 0.5 \text{ GeV}^2$. No estimate is made of the possible misidentification resulting from this selection method. In addition, both kaons were required to have momenta greater than 1 GeV/c.

The $K^+ K^- \pi^+ \pi^-$ invariant mass is shown in Fig. 7.19. Two separate fits were made to the data: 1) a polynomial curve of fifth order assuming no signal is present and 2) a Breit-Wigner (mass = 2.14 GeV, $\Gamma = 75 \text{ MeV}$) and a fifth order polynomial background curve. The background determined from the first fit is not significantly different from that of the second fit. The second fit corresponds to 27 events in the Breit-Wigner above background. The Monte Carlo acceptance for this reaction, assuming a mass of 2.14 GeV and a width of 75 MeV and a t -distribution of e^{-6t} was 4%. This corresponds to a cross section of $\sigma(\phi' \rightarrow K^+ K^- \pi^+ \pi^-) = 528 \pm 290 \text{ nb}$. The error was determined from the fitted parameters. The first fit corresponds to a cross section of $\sigma(\phi' \rightarrow K^+ K^- \pi^+ \pi^-) = 437 \pm 175 \text{ nb}$ where the error is statistical. A previous experiment (49) has reported evidence for a phi prime with a mass of 2.15 GeV and width of 140 MeV.

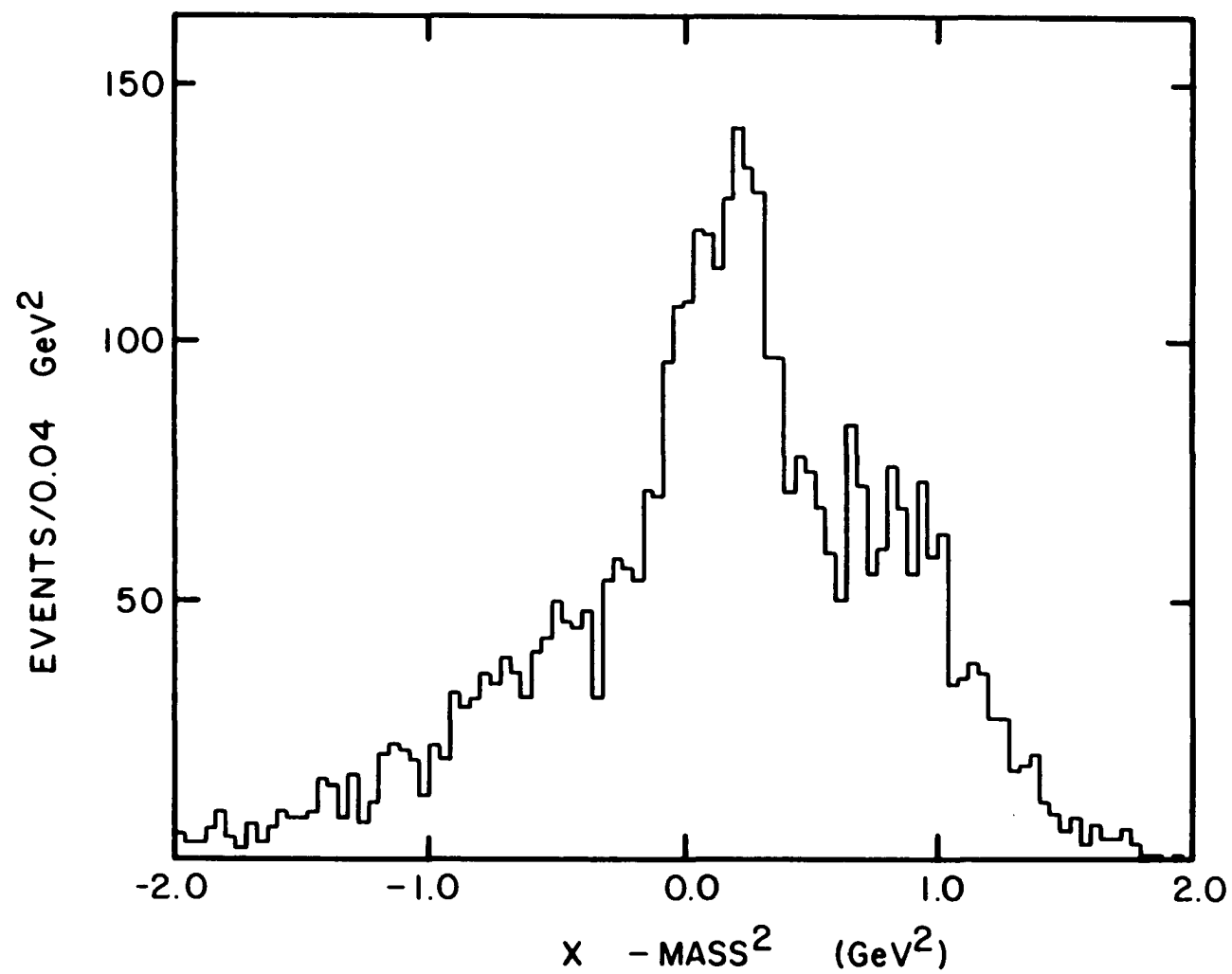


Figure 7.18. X -mass² distribution for the reaction $\pi^+ n \rightarrow X^+ X^- \pi^+ \pi^- p$

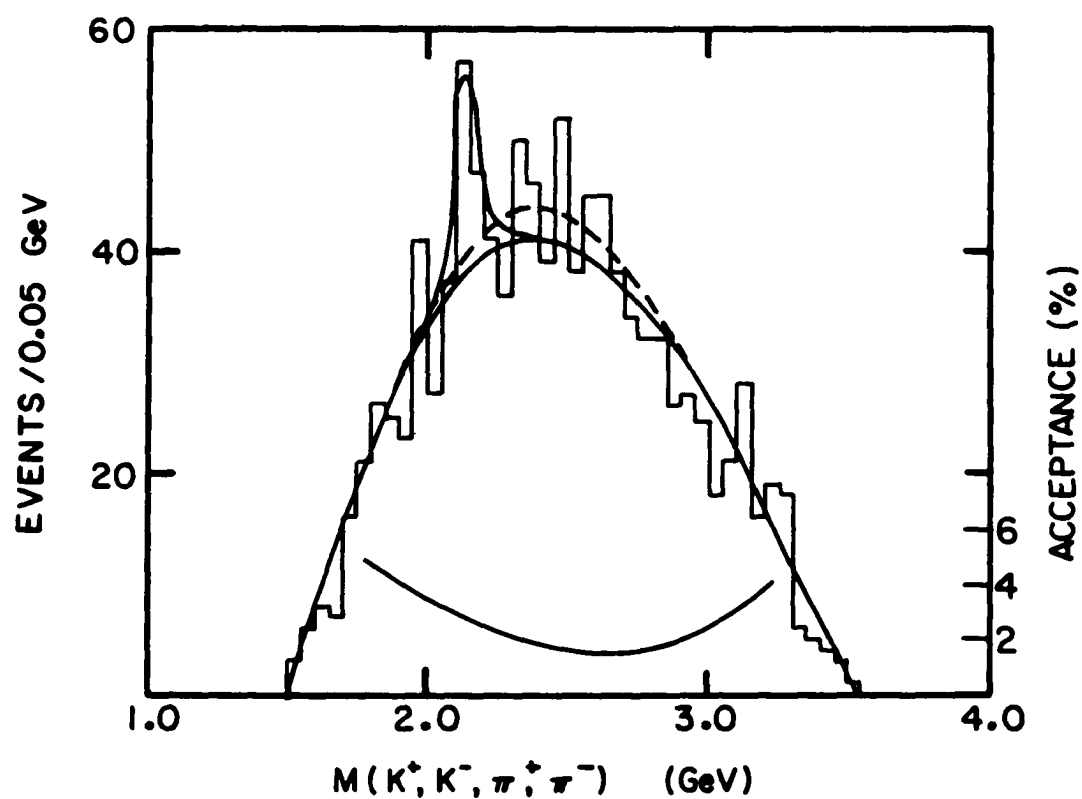


Figure 7.19. $K^+ K^- \pi^+ \pi^-$ mass distribution for the reaction $\pi^+ n \rightarrow K^+ K^- \pi^+ \pi^- p$. Dashed curve is a polynomial fit to the distribution. Upper solid curve is a Breit-Wigner + polynomial background. Lower solid curve is acceptance as a function of mass

APPENDIX

C1, C2 Cherenkov Efficiencies

A study was made of the efficiencies of C1 and C2 using data from the present experiment, E128. All efficiencies were calculated using only two prong elastic events. Approximately 423,000 events were processed from which 13,000 elastic events were selected. The elastic events consisted of 1.7K 3.5 GeV/c π^+ , 3.8K 4.5 GeV/c π^+ , 2.2K 5.5 GeV/c π^+ , 5.2K 5.5 GeV/c π^- , and 70 10 GeV/c π^+ . Elastic events were selected by neglecting any deviation of the incident beam from the z-axis and calculating the transverse momentum in the x-y plane. In the x-y plane, the angle α between the outgoing pion and the recoiling proton was required to satisfy $2.95 < \alpha < 3.33$. Also, the difference in the magnitude of the transverse momenta of the outgoing particles was required to be less than 0.15 GeV/c.

C1 efficiencies were calculated by considering only those events in which the fast pion passed through the active area of C1. A cell was said to fire if the bufferstrobe bit was on or the ADC value was greater than 9. It was necessary to look at both the bufferstrobes and the ADCs because cell 22 had a bad B.S. but a good ADC while cell 29 had a bad ADC but a good B.S. Looking at both readouts also increased the efficiency of most cells by about 1%. If the particle passed through more than one cell, the first cell found to fire was acknowledged as good and the other cells were ignored whether or not they had fired. If no cell fired, then all cells passed through were penalized. This procedure was used for all efficiencies except the efficiency as a

function of the number of cells passed through and the efficiency as a function of track length where in both cases every cell passed through was held accountable for itself. Only the B and C rings were used in the track length efficiency since the A and D rings were so inefficient. Also, all efficiencies (except momentum) were calculated requiring the pion momentum to be greater than 4.1 GeV/c. The efficiency as a function of angle and radius was calculated by dividing each cell into sixteen sections as shown in Fig. A.2. A number of sections were found to be considerably less efficient than the majority of the cell. The cell efficiencies were recalculated excluding these inefficient regions - inefficient regions being arbitrarily defined as those regions with an efficiency less than 80%. As might be expected, the inefficient areas lie near cell boundaries. This is clearly depicted in Fig. A.4, which is a plot of the x-y position of all tracks that did not make light in C1.

C1 Efficiency Checking Both ACD and BUF
 (If either the ADC or BUF fired, it is considered a hit)

<u>A</u>	<u>Eff</u>	<u>Err</u>	<u>B</u>	<u>Eff</u>	<u>Err</u>	<u>C</u>	<u>Eff</u>	<u>Err</u>
1	68.8	8.2	1	95.0	1.2	1	98.2	0.6
2	66.7	9.6	2	96.3	1.1	2	97.8	0.7
3	74.2	7.9	3	89.7	1.8	3	96.0	0.9
4	71.9	8.0	4	93.5	1.4	5	96.2	0.9
5	61.5	9.5	5	84.0	2.0	5	97.0	0.8
6	40.6	8.7	6	78.1	2.1	6	94.3	1.0
7	60.0	9.8	7	77.4	2.3	7	91.2	1.3
8	70.4	8.8	8	93.2	1.4	8	93.3	1.2
9	59.0	7.9	9	95.0	1.2	9	90.9	1.4
10	67.9	8.8	10	84.4	2.0	10	91.7	1.2
11	42.1	8.0	11	84.9	1.9	11	89.8	1.4
12	76.9	8.3	12	96.6	1.0	12	97.3	0.7

<u>Ring</u>	<u>Eff</u>	<u>Err</u>
A	62.5	2.6
B	88.8	0.5
C	94.5	0.3
D	26.7	6.6

C1 Overall Efficiency 90.8 ± 0.3

C1 Efficiency Checking ADC and BUF
and
Using only tracks that passed through only 1 cell

<u>A</u>	<u>Eff</u>	<u>Err</u>	<u>B</u>	<u>Eff</u>	<u>Err</u>	<u>C</u>	<u>Eff</u>	<u>Err</u>
1	70.0	8.4	1	95.7	1.2	1	98.7	0.5
2	60.0	11.0	2	96.6	1.1	2	98.4	0.6
3	76.7	7.7	3	90.5	1.7	3	96.9	0.8
4	75.0	8.2	4	94.7	1.3	4	97.2	0.8
5	62.5	9.9	5	85.8	1.9	5	98.0	0.6
6	41.9	8.9	6	80.2	2.1	6	95.3	1.0
7	59.1	10.5	7	78.6	2.3	7	91.1	1.4
8	75.0	8.8	8	93.2	1.4	8	93.0	1.3
9	60.0	8.3	9	94.5	1.3	9	90.9	1.4
10	66.7	9.6	10	86.0	2.0	10	93.4	1.2
11	42.4	8.6	11	88.2	1.8	11	92.0	1.3
12	78.3	8.6	12	97.6	0.8	12	97.4	0.7

<u>Ring</u>	<u>Eff</u>	<u>Err</u>
A	63.3	2.7
B	90.0	0.5
C	95.3	0.3
D	28.9	7.4

C1 Overall Efficiency 91.7 ± 0.3

C1 Efficiencies for Efficient Region and Inefficient Region
(4.5 and 5.5 GeV/c data with momentum >4.1 GeV/c)

Efficient Region						Inefficient Region					
<u>B</u>	<u>Eff</u>	<u>Err</u>	<u>C</u>	<u>Eff</u>	<u>Err</u>	<u>B</u>	<u>Eff</u>	<u>Err</u>	<u>C</u>	<u>Eff</u>	<u>Err</u>
1	95.0	1.2	1	98.2	0.6	1			1		
2	96.3	1.1	2	97.8	0.7	2			2		
3	91.5	1.7	3	96.0	0.9	3	74.2	7.9	3		
4	94.6	1.3	4	96.2	0.9	4	63.6	14.5	4		
5	95.0	1.5	5	97.0	0.8	5	65.9	4.1	5		
6	95.3	1.3	6	95.0	1.0	6	40.7	4.5	6	76.5	10.3
7	95.4	1.4	7	95.7	1.0	7	42.9	4.7	7	57.4	6.7
8	95.7	1.2	8	98.7	0.6	8	72.2	7.5	8	54.6	6.7
9	96.4	1.1	9	97.2	0.9	9	61.5	13.5	9	50.0	6.7
10	96.0	1.4	10	98.0	0.7	10	67.2	4.1	10	66.0	4.9
11	90.8	1.8	11	94.5	1.1	11	66.3	5.1	11	58.1	6.3
12	97.6	0.8	12	97.3	0.7	12	79.0	9.4	12		

Efficient Region			Inefficient Region		
<u>Ring</u>	<u>Eff</u>	<u>Err</u>	<u>Ring</u>	<u>Eff</u>	<u>Err</u>
1	62.5	2.6	1	200.0	200.0
2	95.0	0.4	2	59.1	1.9
3	96.8	0.2	3	59.2	2.7

Only 1 Cell Hit

Efficient Region			Inefficient Region		
<u>Ring</u>	<u>Eff</u>	<u>Err</u>	<u>Ring</u>	<u>Eff</u>	<u>Err</u>
1	63.3	2.7	1	200.0	200.0
2	95.5	0.4	2	61.8	2.0
3	97.4	0.2	3	61.9	2.8

Overall Counter Efficiency

Efficient Region 94.8 ± 0.2

Inefficient Region 59.1 ± 1.5

Only 1 Cell Hit

Efficient Region 95.4 ± 0.2

Inefficient Region 61.8 ± 1.6

C1 Efficiency as a Function of the Number of Cells Passed Through
(4.5 and 5.5 GeV/c data)

Momentum >4.1 GeV/c

# of cells	Eff	Err
1	91.8	0.3
2	88.7	1.2
3	70.0	14.5

No Momentum Cut

# of cells	Eff	Err
1	89.2	0.3
2	84.4	1.3
3	32.0	9.3
4	0.0	
5	10.53	7.0

Determination of Radial Position

The position of a track through a cell was taken to be the center of the track in that cell. The C1 cells all point back to the center of the target. Assuming the particle originated from the center of the target, the radial position of the particle at the beginning of the segmented region of C1 was then calculated by extrapolating the position backwards as shown in Fig. A.1.

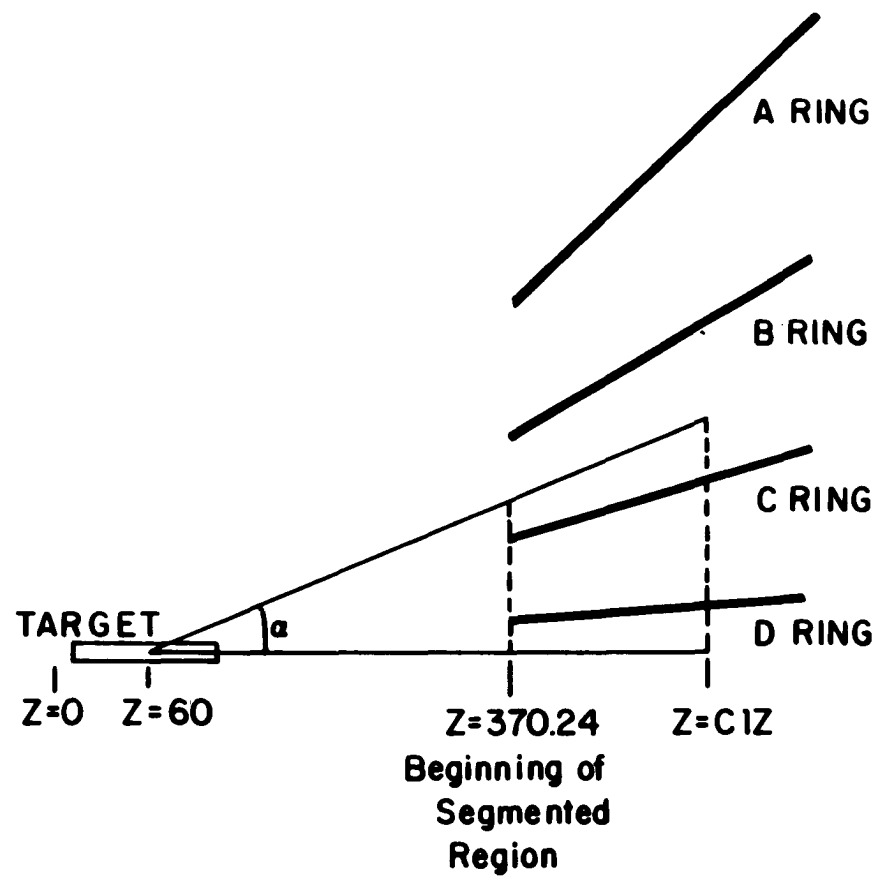
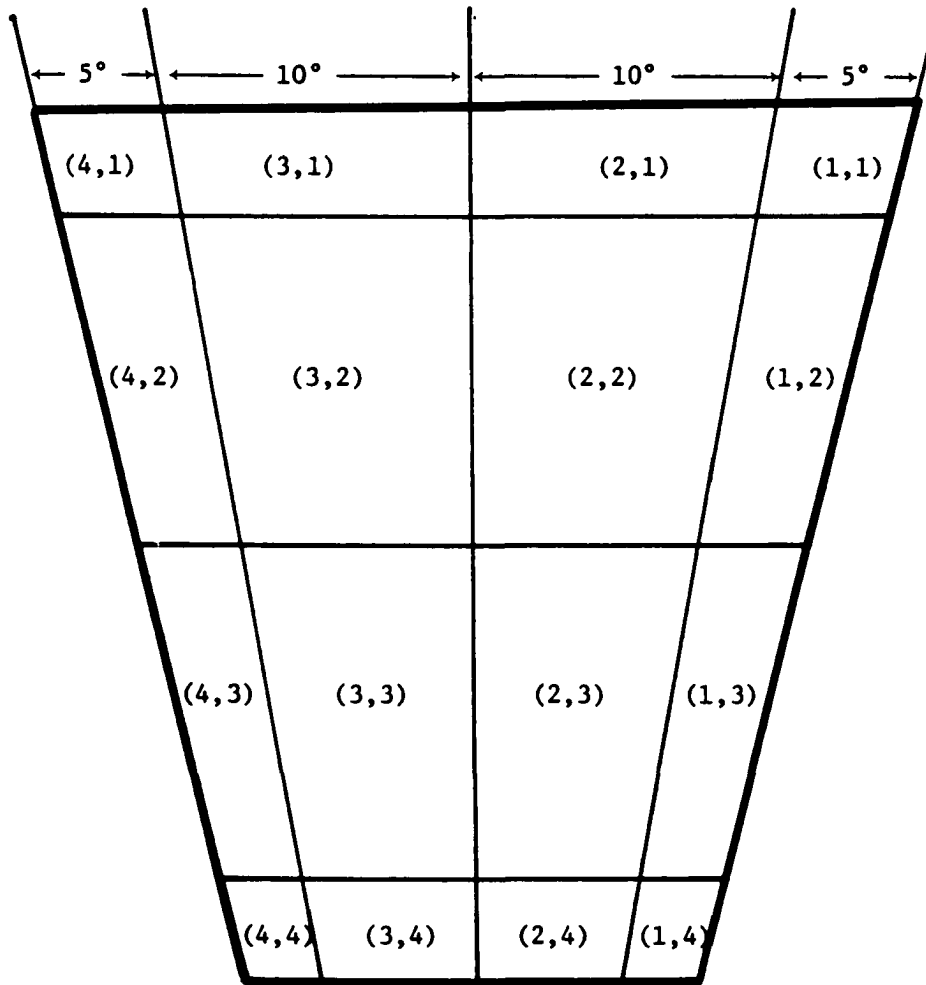


Figure A.1. Determination of radial position in C1

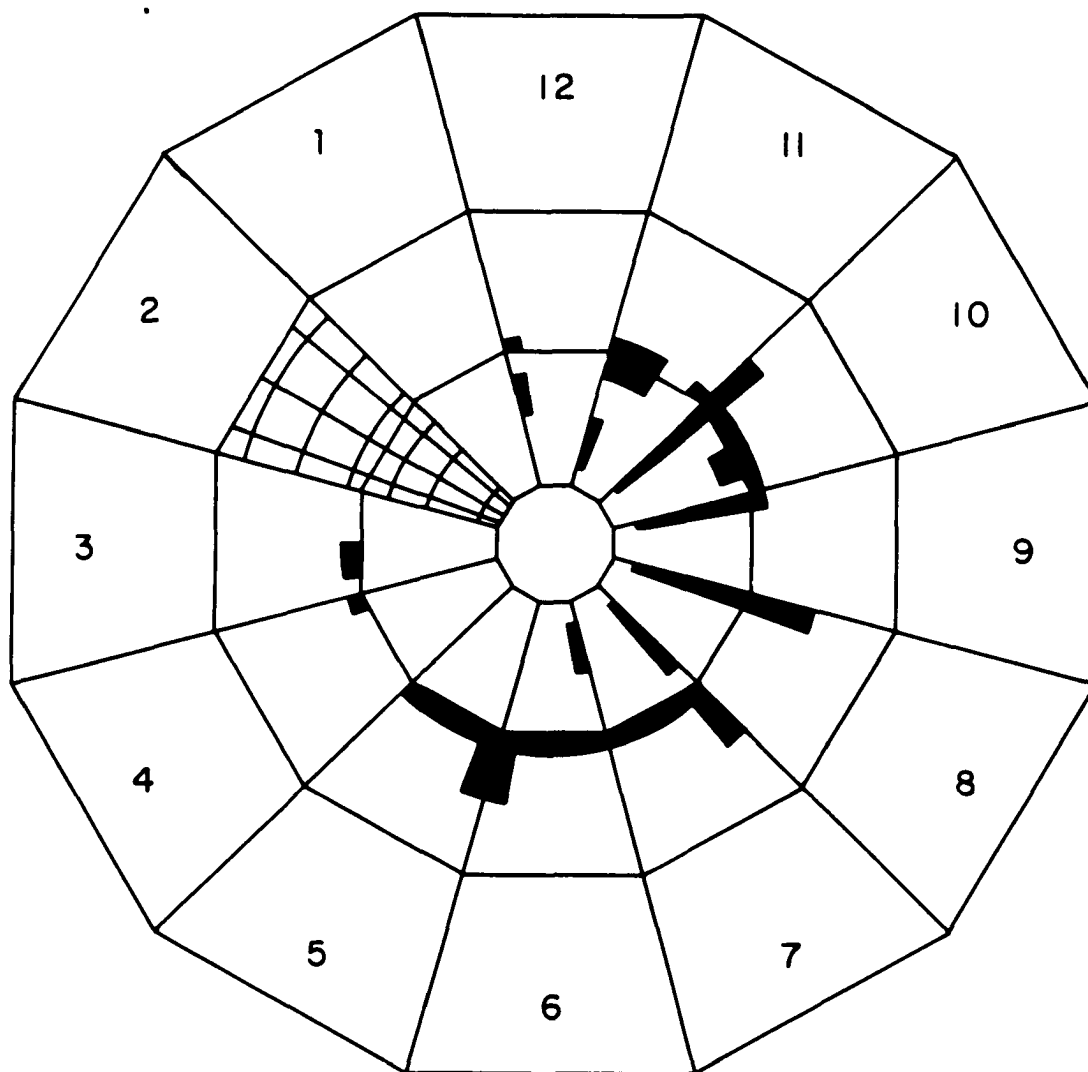


Radial Boundaries at $z = 310.24$ cm

51.90	B Ring Outer Boundary
48.0	
40.0	
32.0	
29.28	C Ring Outer Boundary
26.0	
18.5	
11.0	
8.44	D Ring Outer Boundary

Figure A.2. Division of cells for angle and radius efficiency

INEFFICIENT AREAS OF C1



Looking down beam

Figure A.3. Inefficient areas of C1

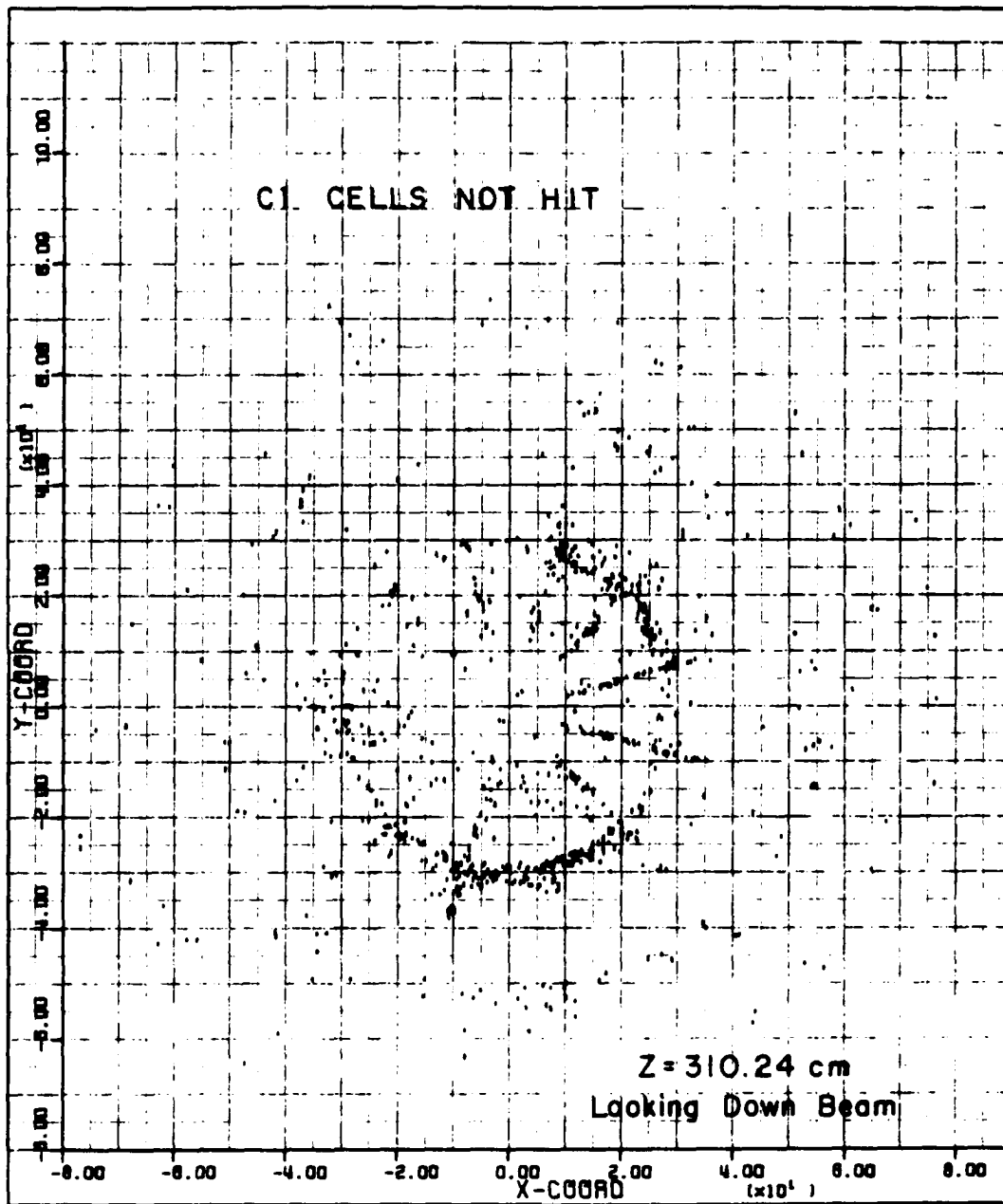


Figure A.4. C1 cells not hit

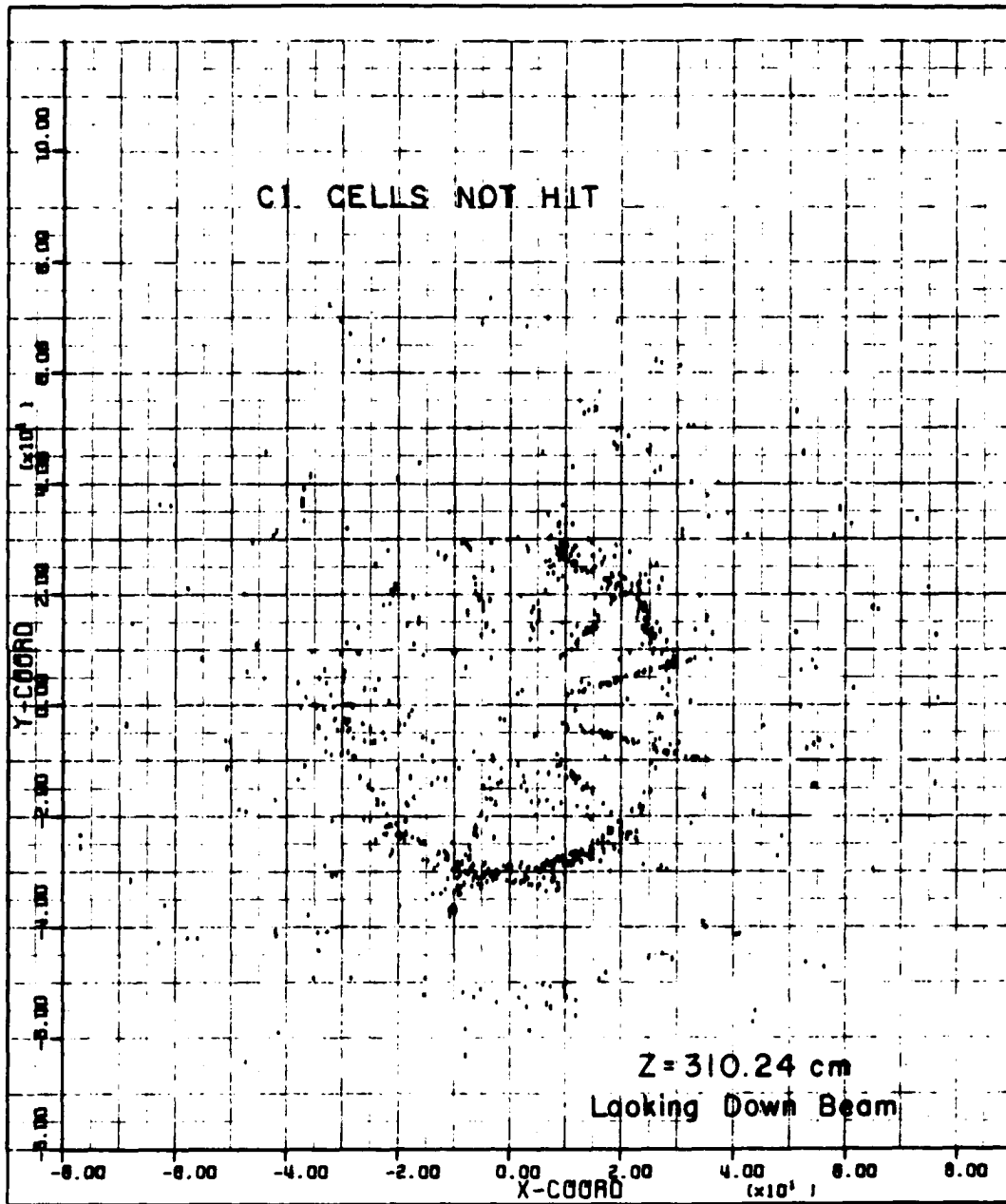


Figure A.4. C1 cells not hit

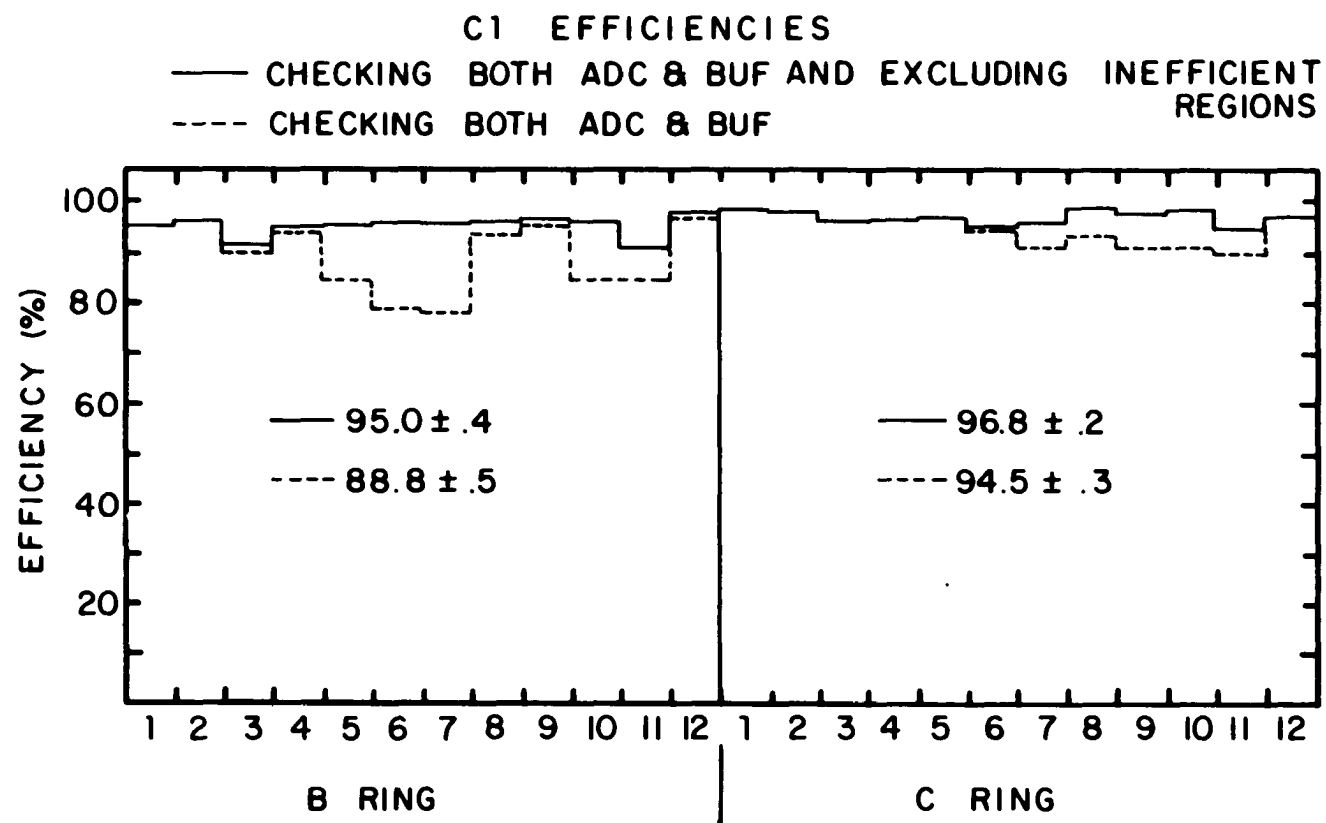


Figure A.5. C1 cell efficiencies

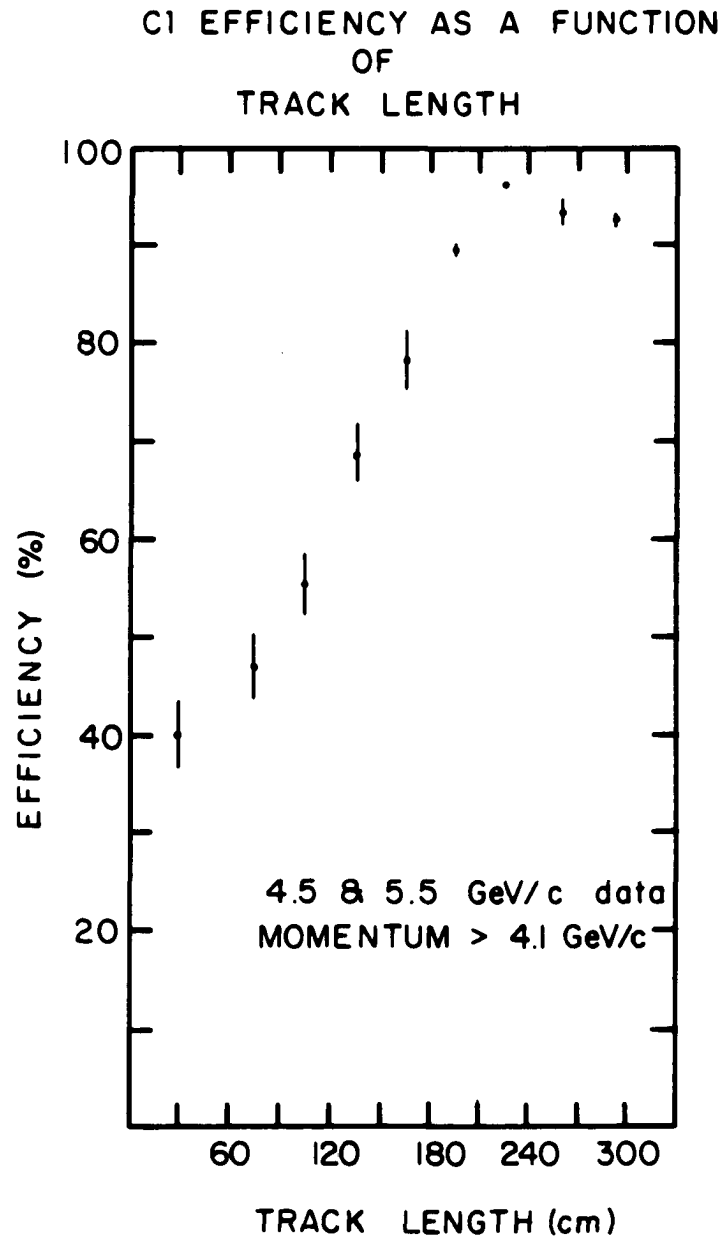


Figure A.6. C1 efficiency as a function of track length

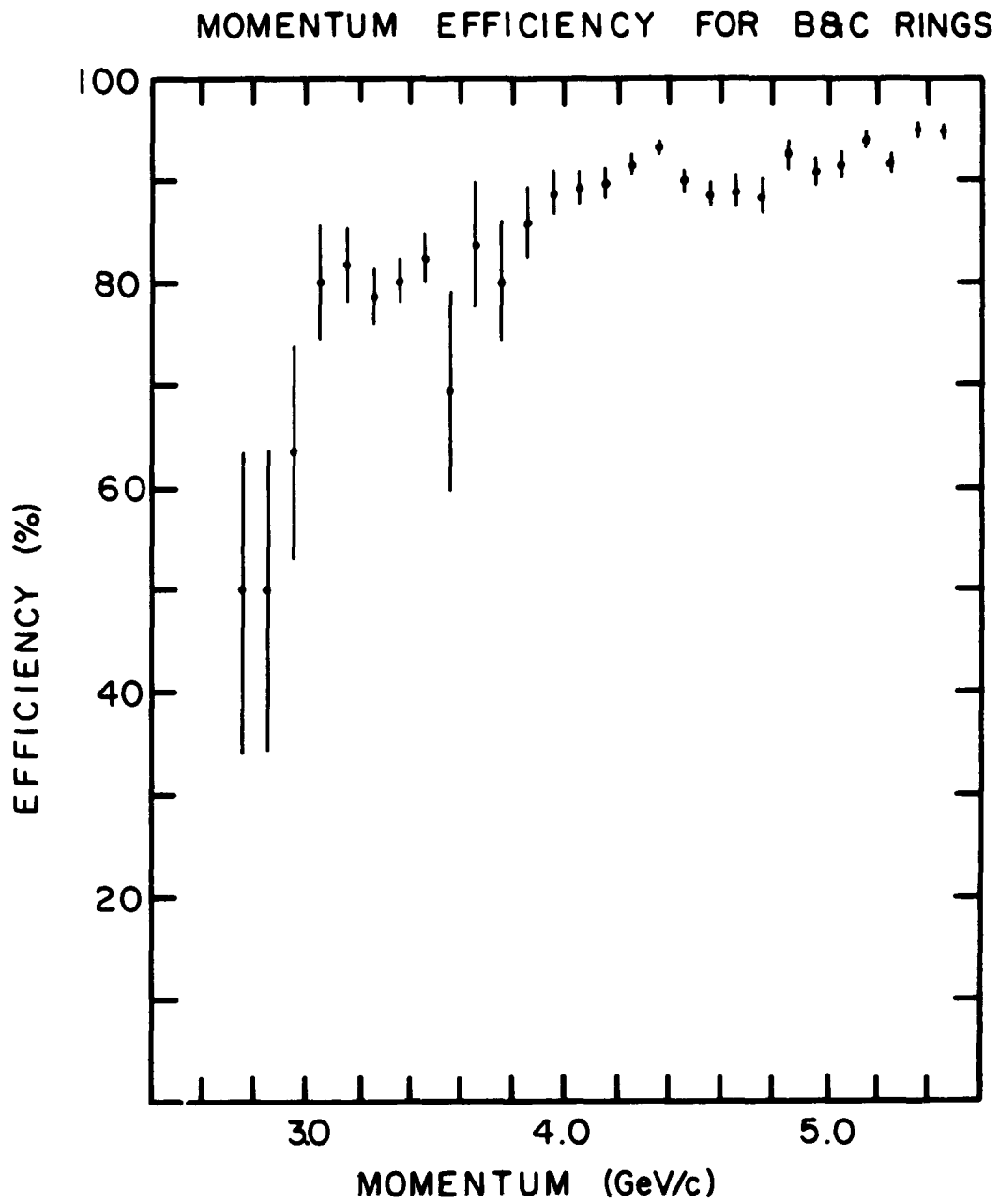


Figure A.7. Cl efficiency as a function of momentum for B and C rings

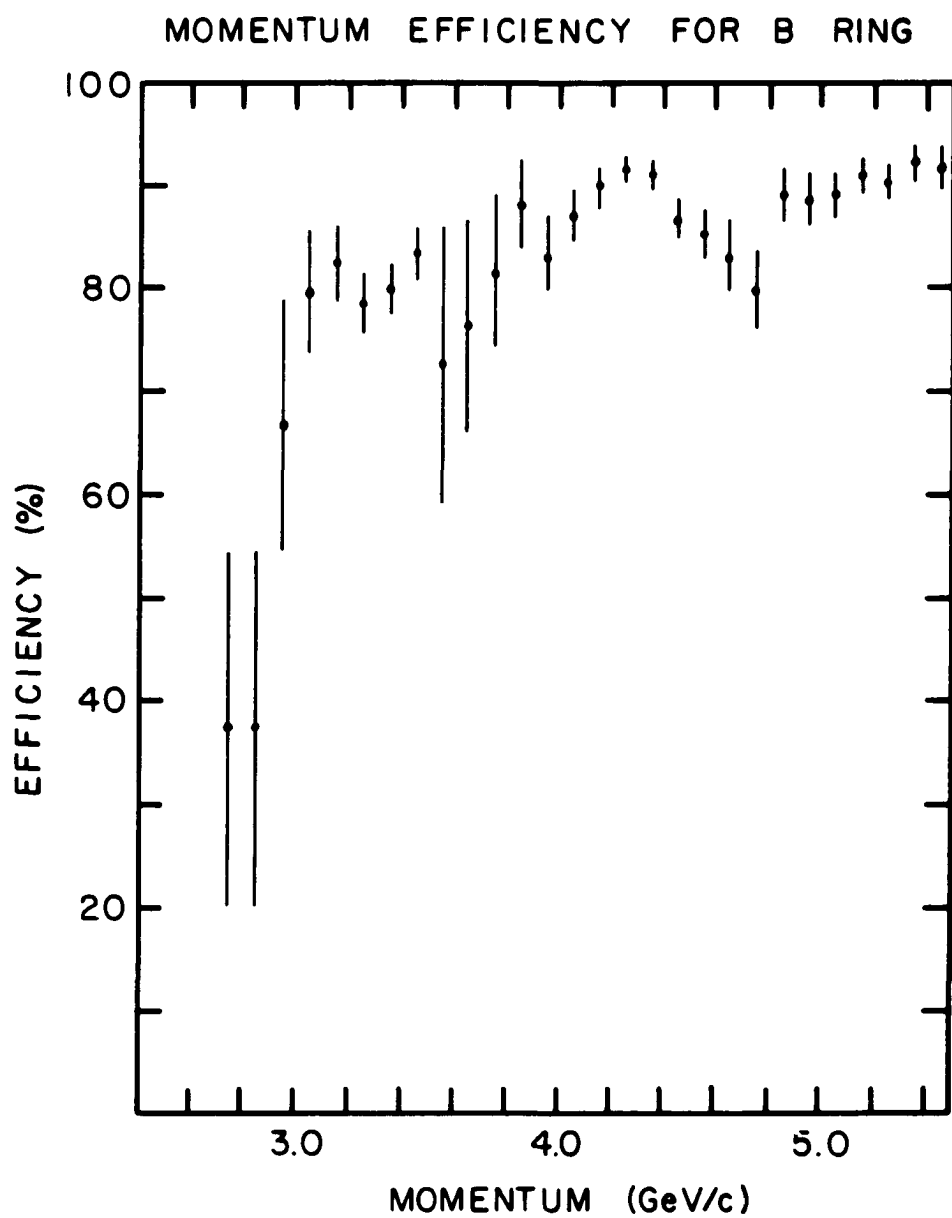


Figure A.8. C1 efficiency as a function of momentum for B ring

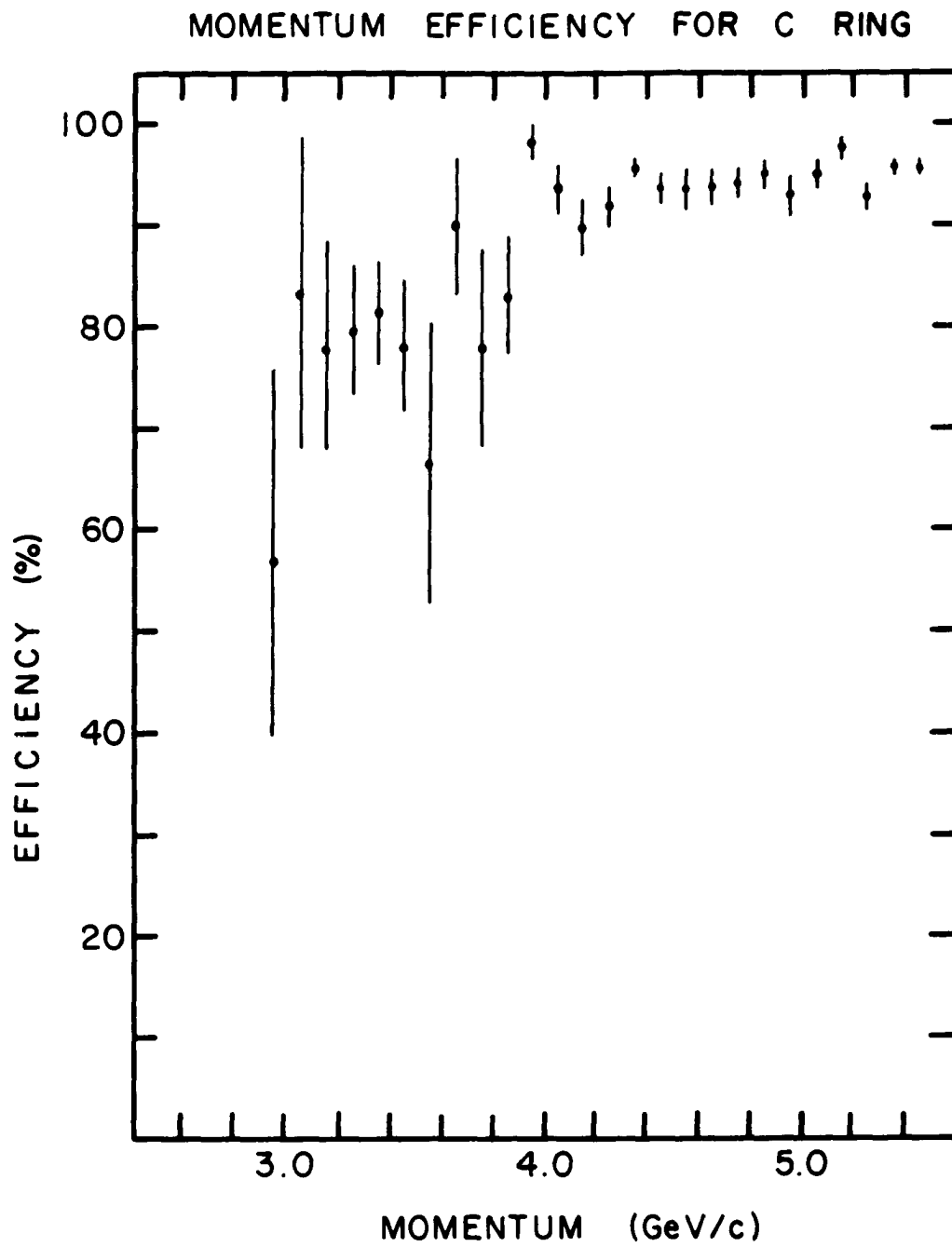


Figure A.9. C1 efficiency as a function of momentum for C ring

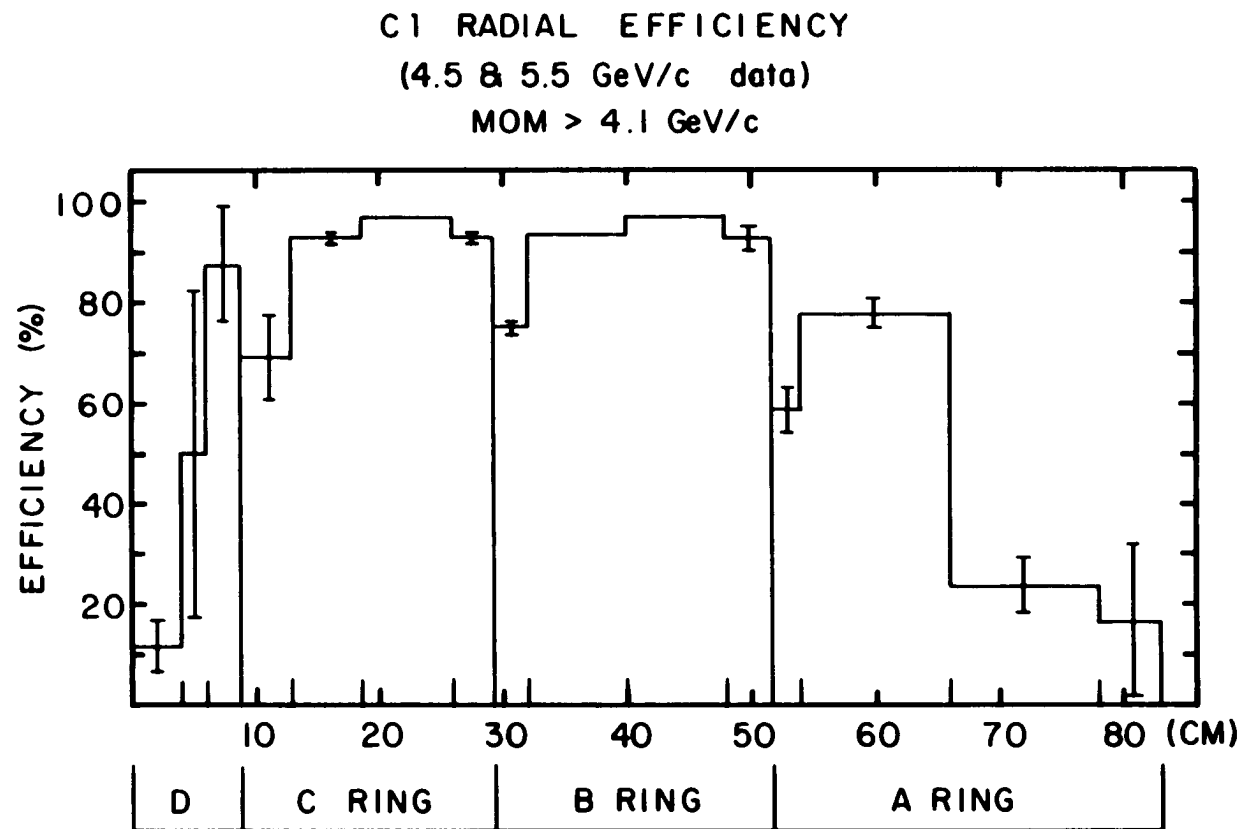


Figure A.10. C1 efficiency as a function of radius

C2 Overall Efficiency using 4.5 and 5.5 GeV/c data

All	84.7 ± 1.0
Center	94.1 ± 1.0
Edge	77.5 ± 1.7
Corner	70.9 ± 6.1

C2 Overall Efficiency using 10 GeV/c data

All	98.2 ± 1.8
Center	100.0
Edge	96.3 ± 3.6
Corner	100.0

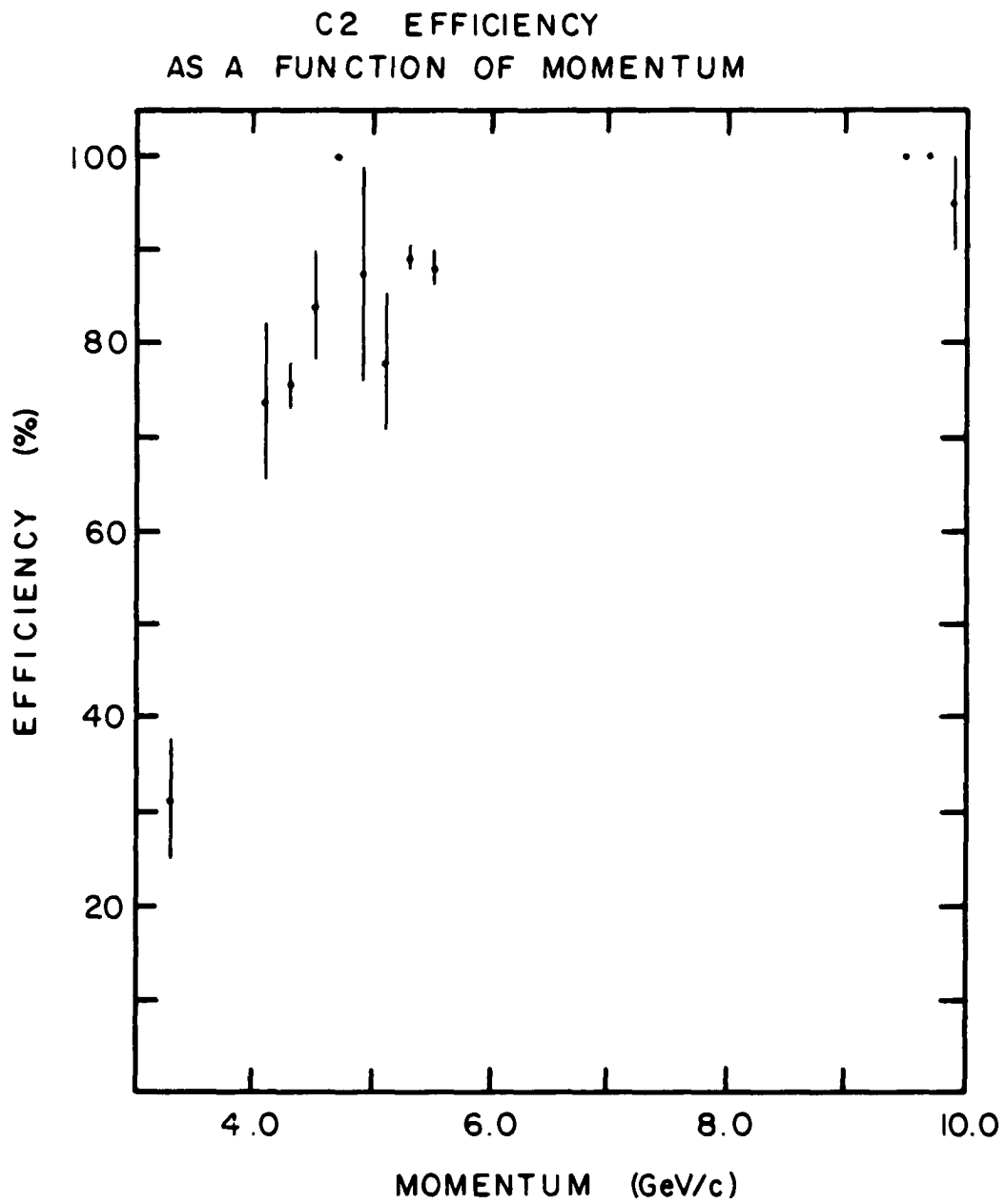


Figure A.11. C2 efficiency as a function of momentum

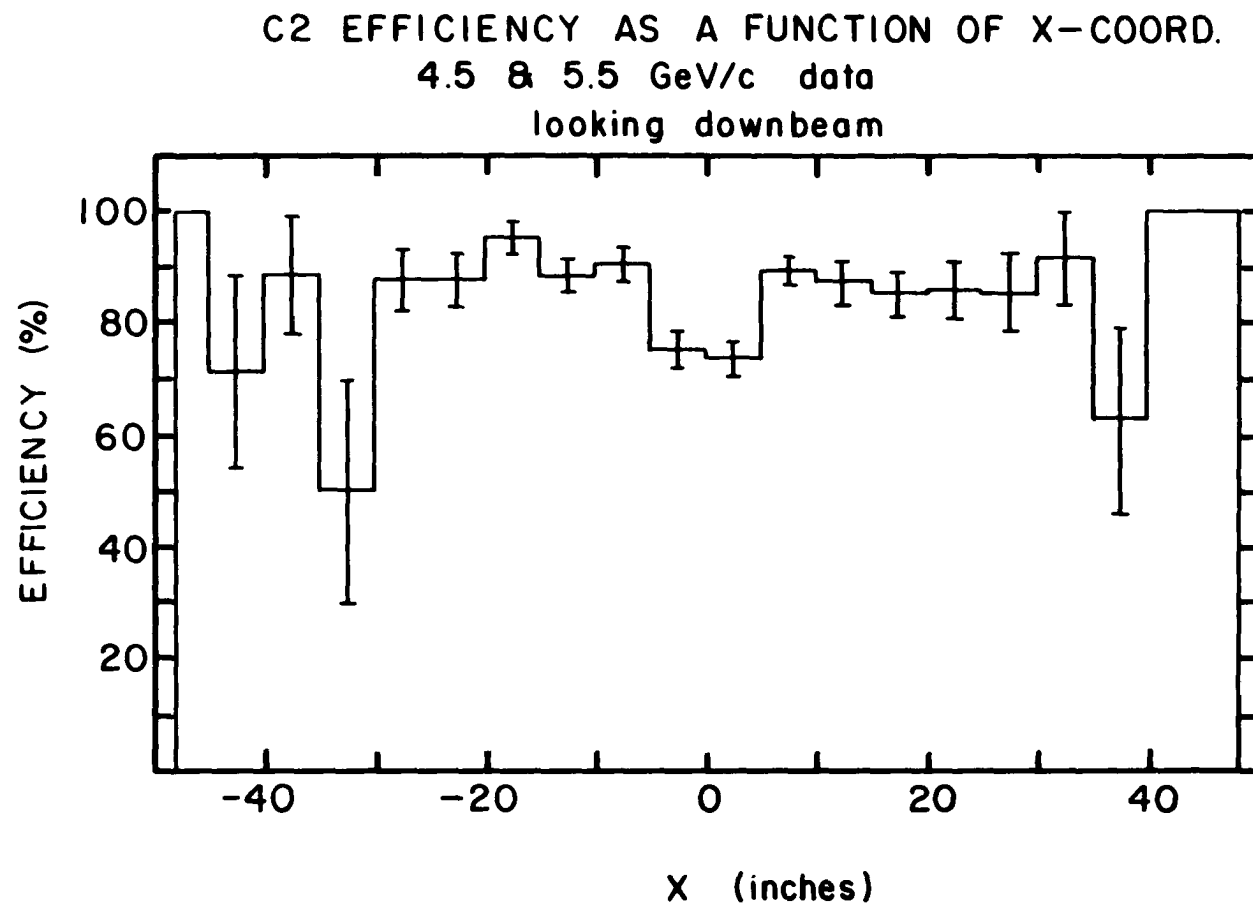


Figure A.12. C2 efficiency as a function of x-coordinate

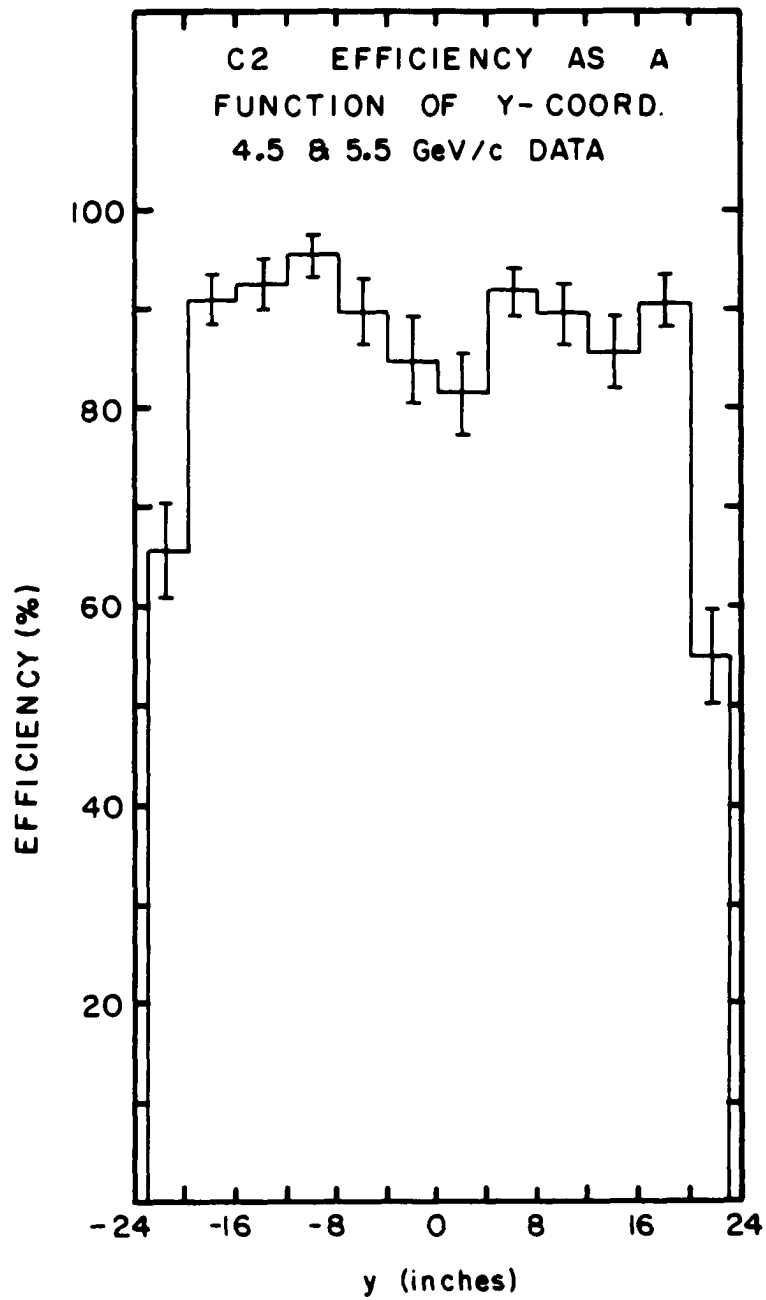


Figure A.13. C2 efficiency as a function of y-coordinate

BIBLIOGRAPHY

1. S. Okubo, Phys. Lett. 5, 165 (1963).
2. G. Zweig, CERN report Nos. TH-401 and TH-412, 1964 (unpublished).
3. J. Iizuka, Prog. Theor. Phys. Suppl. 21, 37 (1966).
4. J. Iizuka, K. Okada, and O. Shita, Prog. Theor. Phys. 35, 1061 (1966).
5. M. Gell-Mann and Y. Ne'eman, The Eightfold Way (Benjamin, New York, 1964).
6. "Review of Particle Properties," Rev. Mod. Phys. 52, No. 2, Part II (April 1980).
7. J. J. Sakurai, Phys. Rev. Lett. 9, 472 (1962).
8. S. Okubo, A Survey of the Quark Line Rule (U.R. 641, Department of Physics and Astronomy, University of Rochester, New York, 1977).
S. Okubo, Phys. Rev. D16, 2336 (1977).
9. H. Harari, Annals of Phys. 94, 391 (1975).
10. H. Fritzsch and M. Gell-Mann, Proc. of the XVI Int. Conf. on High Energy Physics, Chicago, 1972, Vol. 2.
11. H. Fritzsch, M. Gell-Mann, and H. Leutwyler, Phys. Lett. 47B, 365 (1973).
12. S. Weinberg, Phys. Rev. Lett. 31, 494 (1973).
13. D. Gross and F. Wilczek, Phys. Rev. Lett. 30, 1343 (1973).
14. H. D. Politzer, Phys. Rev. Lett. 30, 1346 (1973).
15. H. Fritzsch and P. Minkowski, Nuovo Cimento 30A, 393 (1975).
16. P. Freund and Y. Nambu, Phys. Rev. Lett. 34, 1645 (1965).
17. J. Arafune, M. Fukugita, and Y. Oyanagi, Phys. Lett. 90B, 221 (1977).
18. S. J. Lindenbaum, Quark Line Diagrams, Rules and Some Recent Data, BNL 50812 (December 1977).

19. H. J. Lipkin, Fermi National Accelerator Laboratory Report, FERMILAB-CONF-77/16-THY, 1977.
20. C. Schmid, D. M. Webber, and C. Sorensen, Nucl. Phys. B111, 317 (1976).
21. S. Yazaki, M. Fukugita, T. Inami, and N. Sakai, Phys. Lett. 68B, 251 (1977).
22. V. Blobel et al., Phys. Lett. 59B, 88 (1975).
23. G. F. Chew and C. Rosenzweig, Nucl. Phys. B104, 290 (1976).
24. M. B. Einhorn and S. D. Ellis, Phys. Rev. D12, 2007 (1975).
25. J. F. Gunion, Phys. Rev. D12, 1345 (1975).
26. M. B. Green, M. Jacob, and P. V. Landshoff, Nuovo Cimento 29A, 123 (1975).
27. R. Moore and A. Donnachie, J. Phys. G4, 1835 (1978).
28. A. Donnachie and P. V. Landshoff, Nucl. Phys. B112, 233 (1976).
29. A. Donnachie and P. V. Landshoff, Z. Physik C4, 231 (1980).
30. H. Fritzsch, Phys. Lett. 67B, 217 (1977).
31. M. Gluck, J. F. Owens, and E. Reya, Phys. Rev. D17, 2324 (1978).
32. J. F. Owens and E. Reya, Phys. Rev. D17, 3003 (1977).
33. F. C. Winkelmann, SLAC Report - 160 (1973).
34. S. L. Shapiro et al., IEEE Trans. Nucl. Sci. NS-23, No. 1, 264 (1976).
35. S. L. Shapiro et al., IEEE Trans. Nucl. Sci. NS-23, No. 1, 269 (1976).
36. B. Bertolucci, SLAC-PUB-1574 (1975).
37. C. L. Woody, Ph.D. Thesis, Johns Hopkins University, Baltimore, Maryland (1980).
38. F. G. Oakham, M.S. Thesis, Carleton University, Ottawa, Canada (1977).

39. M. Marshall, Ph.D. Thesis, California Institute of Technology, Pasadena, California (1980).
40. D. Blockus, Ph.D. Thesis, Johns Hopkins University, Baltimore, Maryland (1980).
41. A. Honma, Ph.D. Thesis, Stanford University, Palo Alto, California (1980).
42. S. Durkin, Ph.D. Thesis, Stanford University, Palo Alto, California (1981).
43. A. Fridman, Fortschritte der Physik 23, 243 (1975).
44. B. D. Hyams et al., Nucl. Phys. B22, 189 (1970).
45. T. C. Bacon et al., Athens Topical Conference, p. 129 (1965) [$\rho p, \omega p$ at 1.7].
 R. J. Miller et al., Phys. Rev. 178, 2061 (1969) [$\omega p, \rho p$ at 2.7].
 M. S. Farber et al., Nucl. Phys. B29, 237 (1971) [$\omega p, \rho p$ at 5.4].
 D. Cohen et al., Phys. Rev. Lett. 38, 269 (1977) [ϕp at 6].
 J. A. J. Mathews et al., Phys. Rev. Lett. 26, 400 (1971) [$\rho p, \omega p$ at 6.95].
 J. E. Richey et al., Phys. Rev. D15, 3155 (1977) [ρp at 15].
46. A. S. Ito et al., FERMILAB-PUB-80/19.
47. M. Aderholz et al., Nucl. Phys. B11, 259 (1969) [$\omega \Delta$ at 8].
 M. Aderholz et al., Nucl. Phys. B14, 255 (1969) [$\phi \Delta$ at 8].
 C. Caso et al., Nuovo Cimento 13A, 343 (1973) [$\rho \Delta$ at 11.7].
 J. Ballam et al., Phys. Rev. D4, 1946 (1971) [$\rho \Delta$ at 16].
 M. Deutschmann et al., Nucl. Phys. B99, 397 (1975) [$\rho \Delta$ at 16].
 R. Honecker et al., Nucl. Phys. B106, 365 (1976) [$\rho \Delta$ at 16].
 H. Grassler et al., Nucl. Phys. B115, 365 (1976) [$\omega \Delta$ at 16].
 N. N. Biswas et al., Phys. Rev. D2, 2529 (1970) [$\rho \Delta$ at 18].
 D. Evans et al., Nucl. Phys. B51, 205 (1973) [$\omega \Delta$ at 11.7].
 J. Gaidos et al., Phys. Rev. D1, 3190 (1970) [$\rho \Delta$ at 13].
 J. Gaidos et al., Nucl. Phys. B72, 253 (1974) [$\omega \Delta$ at 13].
 J. Gaidos et al., Phys. Rev. D12, 2565 (1975) [$\rho \Delta$ at 13].
48. A. Bradley and D. Robson, Z. Physik C4, 67 (1980).
49. T. J. Killian et al., Phys. Rev. D21, 3005 (1980).
50. M. Goodman, Ph.D. Thesis, University of Illinois, Urbana-Champaign, Illinois (1979).
 D. Aston et al., Laboratoire de l'Accelérateur Lineaire Report (Orsay), LAL/81-09 (1981).
 G. Costa et al., Nucl. Phys. B175, 402 (1980).

- B. Delcourt et al., Phys. Lett 99B, 257 (1981).
F. Mane et al., Phys. Lett. 99B, 261 (1981).